UNIVERSITÀ DEGLI STUDI DI PALERMO

Corso di DOTTORATO DI RICERCA in SCIENZE FISICHE

Curriculum in Fisica Statistica e Interdisciplinare – Internazionale

Dipartimento di Fisica e Chimica

SSD: Fis02

RESISTIVE SWITCHING IN MEMRISTORS BASED ON YTTRIA-STABILIZED ZIRCONIA

IL DOTTORE
MARIA N. KORYAZHKINA

IL COORDINATORE
G. MASSIMO PALMA

IL TUTOR
BERNARDO SPAGNOLO

CO TUTOR
OLEG N. GORSHKOV
DMITRY O. FILATOV

XXXIII CICLO
2020

List of abbreviations:

AFM – Atomic Force Microscopy;

C–V curves – capacitance-voltage characteristics;

CAFM – Conductive Atomic Force Microscopy;

G–V curves – conductance-voltage characteristics;

HRS – high resistance state;

I–V curves – current-voltage characteristics;

KPFM – Kelvin Probe Force Microscopy;

LRS – low resistance state;

MIM – metal-insulator-metal;

MIS – metal-insulator-semiconductor;

NPs – nanoparticles;

RRAM – Resistive Random Access Memory;

SNR – signal-to-noise ratio;

SCLC – space-charge-limited current;

SCR – space charge region;

TEM – Transmission Electron Microscopy;

YSZ – yttria-stabilized zirconia.

Table of contents

Introduction

Rationale

Recently, the applied research is focused on the creation of a new generation of non-volatile memory devices, since the modern technology of non-volatile flash memory has approached the scalability limit and is facing fundamental and engineering difficulties [1]. In this regard, the largest manufacturers of electronic component base (IBM, Samsung, Intel, Sharp, Hewlett Packard, SONY, Panasonic, etc.) in the past few years have been actively engaged in the development of fundamentally new non-volatile memory elements with high performance and scalability. To date, Resistive Random Access Memory (RRAM) devices are of considerable interest [2]. The operation of RRAM is based on the resistive switching effect [3]. Resistive switching is a reversible bistable (multistable) change in the electrical conductivity of an insulator under the influence of an external electric field. The key element of such memory is the memristor – a metal-insulator-metal (MIM) structure capable of changing the conductivity of an insulator under the action of an applied voltage and maintaining a state with a certain resistance for a long time without expending additional energy [4]. Memristors technology and resistive switching physics are in the focus of attention of the world's leading research centers. The tasks of research in the field of electronics based on memristive systems are the establishment of regularities, mechanisms and construction of physical models of resistive switching processes, optimization of resistive switching parameters, which significantly depend on the characteristics of memristive structures, materials of electrodes and insulator, as well as the topology of memristive devices [5]. Due to the ability to continuously change conductivity depending on the applied electrical signal, memristors are considered as an element of a new generation of non von Neumann computers with multilevel logic [6], as well as electronic synaptic devices and neuromorphic computers [7].

To date, a significant amount of works have been published on the search for materials of electrodes and insulator, technologies for the preparation of memristive structures, as well as the development of theoretical models of the resistive switching process. At the same time, the issues of choosing materials of electrodes and insulator that provide optimal parameters of memory elements, their thermal sustainability and stability of switching parameters, as well as integration into a standard complementary metal-oxide-semiconductor (CMOS) fabrication process remain insufficiently investigated [8]. From the point of view of the technology for creating memristive devices, transition metal oxides, for example, HfO_x, TaO_x, ZrO_x, as well as SiO_x *и* GeO_x, are considered promising insulator materials. The generally accepted resistive switching mechanism in memristors based on these materials is considered to be the reversible rupture and restoration of conductive filaments in the thickness of the insulator film. These filaments are formed during preliminary electroforming from oxygen vacancies under the action of an electric field, applied between the electrodes [9]. The concentration of oxygen vacancies in oxide films is a key parameter of the resistive switching process in oxide-based memristors. The concentration of oxygen vacancies required for resistive switching is usually achieved by deposition of non-stoichiometric oxides or by annealing the insulator layers in vacuum after deposition. It should be noted that, in memristors based on non-stoichiometric oxides, degradation of resistive switching parameters is possible due to the absorption of oxygen from the surrounding atmosphere [10]. It should be emphasized here that cation mobility is also inherent in these matrices (for example, [11]). Also, in addition to the filamentary switching mechanism, there are also interfacial switching mechanism (for example, [12]), in which resistive switching occurs as a result of changes along the entire electrode/switching layer interface, and bulk switching mechanism (for example, [13]), in which resistive switching occurs due to phase transition inside the switching layer.

This dissertation work develops an innovative approach to the use of metal oxides in memristive structures, in which the concentration of oxygen vacancies can

be controlled by doping the matrix with impurities with a valence different from the valence of the metal atoms of matrix. This provides great opportunities for controlling the parameters of memristors and increased stability of their functioning. Such oxides include, for example, yttria-stabilized zirconia (YSZ). The use of YSZ in the development of RRAM devices allows, in contrast to non-stoichiometric oxides, to control the concentration of oxygen vacancies and, as a result, the parameters of memory cells.

Another approach that allows to controlling the parameters of resistive switching is nanostructuring the insulator, in particular, embedding of metal nanoparticles (NPs) into it [14]. The embedding of metal NPs leads to significant changes in the electrical properties of insulator films. In particular, metal NPs can act as concentrators of the electric field inside insulator films, which facilitates electroforming and resistive switching [15].

The use of a semiconductor as one of the electrodes of the memristive structure makes it possible to facilitate the integration of memristors into CMOS technology and thereby significantly brings the transition to RRAM production. In addition, the change in the electrical conductivity of semiconductors under the action of optical radiation (photoconductivity) opens up the possibility of using memristors on the basis of metal-insulator-semiconductor (MIS) structures in optoelectronics: creation of RRAM elements switched by optical signal, which may lead to the appearance of a new field of science and technology – *memristive optoelectronics*.

This dissertation work also develops an approach to describing a memristor using the statistical physics formalism usually applied to the description of the behavior of nonlinear multistable systems. The application of this method, which is relatively new for the memristors topic, allows one to discover and study in detail the constructive role of noise, which, ultimately, provides fundamentally new possibilities for increase of stability, forecasting of behavior and control of parameters of memristive devices.

The goal of the dissertation work

Establishment of mechanisms and peculiarities of resistive switching in memristors based on yttria-stabilized zirconia.

Main tasks of the dissertation work

1. Investigation of the electrical properties of memristive structures based on YSZ before electroforming, during electroforming, and during resistive switching.
2. Investigation of the effect of current compliance and temperature on the characteristics of memristive MIM-structures, their electroforming and resistive switching.
3. Establishment of the mechanism (mechanisms) of current transfer and resistive switching in memristive MIM-structures based on YSZ.
4. Investigation of the influence of optical radiation on the resistive switching of memristive MIS-structures based on YSZ.
5. Investigation of the influence of a noise signal on the characteristics of memristors based on YSZ.

Scientific novelty of the dissertation work

1. Using a set of low-temperature methods for investigations of the ion migration polarization of an insulator of memristive structures, the value of activation energy of migration of oxygen ions in YSZ was obtained (0.50 – 0.55 eV in the temperature range T = 300 – 500 K).
2. It was established that change in the dielectric loss tangent in memristive MIM-structures based on YSZ during resistive switching result from the formation of filaments in the insulator.
3. The effect of resistive switching, stimulated by optical radiation, of MIS-structures based on YSZ has been observed.

4. It was experimentally shown that the PDF of the resistance of the memristive system based on YSZ demonstrates several (2 or more) quasi-stable local maxima subject to the noise parameters and changes over time under the influence of a noise signal.

Theoretical and practical contribution of the dissertation work

1. The technological conditions for the preparation by magnetron sputtering of memristive MIM-structures based on YSZ, which are required for use in non-volatile memory devices (the number of switching up to 10^6, switching time ~ 70 ns, the ratio of resistances in high resistance state (HRS) and low resistance state (LRS) > 10).
2. The established value of the activation energy of migration of oxygen ions in YSZ is key parameter for understanding the evolution of filaments in memristors based on YSZ and other oxides during electroforming and resistive switching. The obtained value of the activation energy is ~ 2 times less than available in the literature one (for T > 900 K), which is associated with the predominant migration of oxygen ions along the grain boundaries in nanocrystalline YSZ films at T < 500 K.
3. It was found that the embedding of Au nanoparticles into YSZ films leads to nonlinearity of the capacitance-voltage characteristics of memristors based on these films due to the accumulation of an electric charge in the nanoparticles. This effect can be used to create memristors with nonlinear capacitance. In particular, on the basis of such elements, it is possible to create devices of combined resistive-charge memory.
4. It was found that memristors based on YSZ demonstrates the effect of resistive switching at high temperatures (up to 125 °C), which indicates that these structures are promising for creating elements of resistive memory with increased temperature sustainability.

5. The results of investigation of the influence of optical radiation on the effect of resistive switching can be used to create photosensitive elements of resistive memory.
6. Using memristive systems based on YSZ as an example, it was experimentally shown that memristors are more complex dynamic system than a system with a simple two-well fixed potential. In particular, (i) it was shown that the PDF of the resistance, which, within the framework of the research method, characterizes the current state of the memristive system, demonstrates several (2 or more) quasi-stable local maxima subject to the noise parameters; (ii) it was found the evolution of PDF of the resistance under the influence of a noise signal, i.e. the influence of noise on the memristors has a multiplicative behavior. The obtained experimental results evidence the applicability of the statistical physics formalism to the description of the dynamical switching behavior of memristors. The considered approach is also applicable to memristors based on other resistive switching types, such as conducting bridge resistive switching.
7. The optimal value of the noise intensity, at which a maximum appears on dependence of the ratio of currents in LRS and HRS on the noise intensity and variation of current after switching to HRS (taken as a measure of switching stability) reaches saturation, was found (14.43 $mV^2 \cdot s$). The dependence of the signal-to-noise ratio of memristance on the external noise intensity reaches a maximum at 10 – 12 $mV^2 \cdot s$. The obtained results evidence that noise can play a constructive role in the nonlinear memristive systems far from equilibrium.

Theses for defence

1. The change in the dielectric losses in memristors based on YSZ during resistive switching result from the formation of filaments in the YSZ film.

2. The nonlinearity of the electrical properties of memristive MIM-structures based on YSZ films with embedded Au nanoparticles result from the accumulation of charge in the nanoparticles.
3. The mechanism of current transfer in the investigated MIM-structures is space-charge-limited current. The conduction in both LRS and HRS is of an activation behavior. The value of activation energy decreases with increasing in value of current compliance.
4. The influence of optical radiation on resistive switching in MIS-structures based on YSZ result from the redistribution of voltage between the insulator and the semiconductor, caused by the appearance of photo-electromotive-force at the insulator/semiconductor barrier.
5. Memristor is a multistable system, and the effect of noise on it has multiplicative behavior.

Author's contribution

The main results presented in this dissertation work were obtained by the author personally or with direct participation. The author personally reviewed the available literature data on the topic of the dissertation work. Some results were obtained together with the staff of the Faculty of Physics and the Research Institute for Physics and Technology of the Lobachevsky State University of Nizhny Novgorod – co-executors of research works, within the framework of which the dissertation work was carried out. The investigation of the electrical properties of memristive structures and the influence of optical radiation on memristive structures were carried out together with Associate Professor, Ph.D., Senior Researcher of the Research and Education Center «Physics of Solid State Nanostructures» S.V. Tikhov. The investigation of the stochastic resonance phenomenon in memristive devices were carried out together with Ph.D., Researcher of the Research and Education Center «Physics of Solid State Nanostructures», Researcher of the Research Institute for Physics and Technology A.I. Belov. Statement of the goal and main tasks of the

dissertation research, experiment planning, analysis and aggregation of obtained results, formulation of conclusions, preparation of reports at scientific conferences and publications on the topic of the dissertation work were carried out together with tutor Full Professor of Theoretical Physics, Professor Bernardo Spagnolo and co-tutors Associate Professor, Ph.D. Oleg N. Gorshkov and Associate Professor, Dr. Dmitry O. Filatov.

The reliability of the obtained results and the validity of scientific theses and conclusions are ensured by the using of modern scientific equipment corresponding to the world level, a combination of well-validated experimental research methods, correct theoretical concepts in the analysis and interpretation of the obtained experimental results, as well as by the reproducibility of the obtained experimental data. The research, performed during the dissertation work, is based on the results of the research, previously published on the topic of this dissertation work and given in the list of references.

Approbation of the results

The main results of the dissertation work have been presented at the following conferences:

- Forum of young scientists of Lobachevsky State University of Nizhny Novgorod (Nizhny Novgorod, Russia, 2013);
- XXI and XXII International Symposium «Nanophysics and nanoelectronics» (Nizhny Novgorod, Russia, 2017 – 2018);
- 3rd International School and Conference «Saint Petersburg OPEN 2016» and 5th International School and Conference «Saint Petersburg OPEN 2018» (Saint Petersburg, Russia, 2016, 2018);
- 23rd Scientific Conference on Radiophysics (Nizhny Novgorod, Russia, 2019);
- International conference “New Trends in Nonequilibrium Stochastic Multistable Systems and Memristors” (Erice, Italy, 2019).

The dissertation materials have been discussed at the scientific seminars of the Faculty of Physics, the Research Institute for Physics and Technology, the Research and Education Center «Physics of Solid State Nanostructures» of Lobachevsky State University of Nizhny Novgorod (Russia), Saint Petersburg Electrotechnical University «LETI» (Russia).

Research on the topic of the dissertation work were carried out by the author within the framework of the project «Research and development of memristive nanomaterials and electronic devices based on it for quantum and neuromorphic computing» (special federal programme «Research and development in priority areas of development of the scientific and technological complex of Russia for 2014-2020», project 2017-14-588-0007-7972, 2017 – 2018, head of project A.N. Mikhaylov) and the project «Complex research of fluctuation phenomena in multistable systems for creation of new generations of electronic devices and neuromorphic artificial intelligence technologies based on memristive materials» (Megagrant of Russian Ministry of Science and Education, Agr. No. 074-02-2018-330 (2), 2018 – 2020, head of project B. Spagnolo).

Author's publications

The dissertation materials are published in 9 papers in the International Scientific journals [A1–A9], in 1 chapter of the book [A10] and 9 proceedings of conferences [A11–A19].

Structure and amount of the dissertation work

The dissertation work consists of List of abbreviations, Introduction, seven chapters, Conclusions, List of publications on the topic of the dissertation work, and List of references. The whole amount of the dissertation work is 152 pages, including 66 figures and 9 tables. List of references contains 179 titles.

Acknowledgements

First of all, I wish to thank my tutor, Prof. Bernardo Spagnolo, and co-tutors, Ph.D. Oleg N. Gorshkov and Dr. Dmitry O. Filatov, for their all-round support and warm encouragement during the work on the dissertation, posing the scientific problems and guiding to effective ways of solution, many hours of discussions of scientific results.

I thank Prof. Bernardo Spagnolo also for hard work on the organization and coordination of the International Ph.D. Program, and providing me with the possibility of participation in this project.

I also wish to thank my colleagues from the Lobachevsky State University of Nizhny Novgorod and the University of Palermo, namely Ph.D. Alexey N. Mikhaylov, Ph.D. Alexander P. Kasatkin, Ph.D. Stanislav V. Tikhov, Ph.D. Alexey I. Belov, Prof. Alexander A. Dubkov, Ph.D. Nikolay V. Agudov, Ph.D. Maria E. Shenina, Ph.D. Davide Valenti and Ph.D. Anna A. Kharcheva, for their help in mastering the memristors topic, statistical physics and simulation, as well as for their support.

I warmly thank my nearest people, who helped me to find enough energy to overcome all difficulties on the way to finalization the dissertation work, namely: my husband Dmitry, parents Tamara and Nikolay, my little and mischievous sister Anna, and my best friend Alena Panaeva.

I thank also Davide Valenti and Luca Leonforte for their hospitality and assistance in making pleasant acquaintance with Palermo.

I wish to thank Russian Ministry of Science and Education (Megagrant of Russian Ministry of Science and Education, Agr. No. 074-02-2018-330 (2), 2018 – 2020) and Ministry of Education, Universities, and Research of Italy (MIUR) for financial support of the research and travels in scope of the International Ph.D. Program.

CHAPTER 1. Memristive structures based on transition metal oxides (Literature review)

This chapter provides a review of the most important literature data on the topic of this dissertation work. The review is focus on memristive structures based on transition metal oxides (Section 1.1). Most attention is paid to memristor structures based on zirconium oxide and yttria-stabilized zirconia (YSZ) (Section 1.2). The assumptions about the mechanisms of electroforming and resistive switching in memristive structures based on transition metal oxides are considered (Section 1.3). Some experimental results are noted that confirm the filamentary model in such structures.

1.1. Effect of resistive switching in memristive structures based on transition metal oxides

The effect of resistive switching was first discovered in metal-insulator-metal (MIM) structures in 1960 in the USSR [16]. The conductivity of the MIM-structure $Al/Al_2O_3/Ag$ was investigated. The current-voltage characteristics (*I–V* curves) of such a structure showed the presence of a maximum. Such characteristics were studied in more detail in [17] using the example of the structures $Zr/ZrO_2/Au$, $Al/Al_2O_3/Au$, $Ta/Ta_2O_5/Au$, $Al/SiO/Au$, $Ti/TiO_2/Au$. The results obtained in this direction over the first decade are published in the review [18]. The same review contains data about MIM-structures based on KCl, LiF, CsJ, KBr, MgF_2, CaF_2, Nb_2O_5, MnF_2.

In 1971 L. Chua proposed a theoretical description of the memristor as a resistor with memory [19]. In 2008, employees of the Hewlett-Packard Company in [4] presented the results of a study of electric transport in memristor based on titanium dioxide from liquid helium temperature to room temperatures. After electroforming in such structures, a continuous transition was observed between two

states: an approximately ohmic state and a state characterized by conductivity through a barrier. The data was interpreted in terms of a model in which electroforming creates a conductive channel that partially connects metal electrodes through a titanium dioxide film. In [20], employees of the same company studied bipolar resistive switching of memristive structures based on titanium dioxide, based mainly on the hysteresis loop of the *I*–*V* curves.

In [21], the concept of filaments based on the developments of Hewlett-Packard Company was considered. The influence of switching parameters on the properties of memristive structures was determined. The features of the *I*–*V* curves were interpreted using the model of the formation of parallel filaments with their dynamic growth and decay.

In [22], the reproducible resistive switching of a polycrystalline thin Gd_2O_3 film without preliminary electroforming was demonstrated. The switching curve was similar to that of other materials (requiring preliminary electroforming), except that initial state was a low resistance state (LRS). The ratio of resistances in high resistance state (HRS) and LRS was 6 – 7 orders of magnitude and was achieved at a voltage of 0.6 V. An analysis of the switching mechanism indicated that the presence of metallic Gd in the Gd_2O_3 film played an important role in the implementation of resistive switching without preliminary electroforming.

In [23], the transition of the switching mode between bipolar resistive switching and unipolar threshold one in the Pt/NiO/Pt structure was observed. Bipolar switching could be changed to unipolar threshold one by applying a positive pulse with an amplitude of 2 V and a duration of 10^{-2} – 10^{-4} s, and vice versa by applying a negative pulse with the same amplitude and duration. A model in which the migration of oxygen ions O^{2-} is responsible for the transition of the switching mode was proposed.

Investigations of memristors based on other oxides (see, for example, [24]) have shown that the current in the LRS is related to the current in oxide materials via localized filaments. In [24], using high-resolution Transmission Electron Microscopy,

filaments in the $Pt/TiO_2/Pt$ were studied during resistive switching. Studies carried out in [24] confirmed that switching was due to the restoration and rupture of Ti_nO_{2n-1} filaments.

In [25], TiO_x-based transparent memory devices were proposed. TiO_x films were completely transparent in the visible region and had an amorphous structure. Resistive memory devices based on such films demonstrated resistive switching and good memory characteristics, including fast switching with 1 μs pulses, stable functioning for $> 10^3$ cycles, and storage of the recorded state at temperatures up to 125 °C. It was concluded that the functioning of the device is due to the reversible restoration/rupture of filaments in TiO_x layer, which was deficient in oxygen.

The review [26] summarizes recent investigations of the behavior of resistive switching in systems based on binary oxides. In [27], detailed measurements of the *I–V* curves and current – time dependences of resistive memory devices $Cu/Ta_2O_5/Pt$ are reported. During preliminary electroforming, Cu ions migrated in the Ta_2O_5, and thus a metal filament consisting of Cu atoms was formed. After electroforming, the device demonstrated bipolar resistive switching from LRS to HRS (RESET process) and vice versa – from HRS to LRS (SET process). From measurements of the temperature sustainability of the LRS, it was concluded that the RESET process consisted in the oxidation of Cu atoms, which was accompanied by Joule heating in the thinnest part of the metal filament, due to which the metal filament was ruptured.

In [28], highly stable and reproducible effects of bipolar resistive switching of Cu/AlN/Pt structures are shown. Memory characteristics, including a large memory window (10^3) and a long storage time (10^6 s), were demonstrated. It was concluded that the current in the RESET process decreases if the current compliance decreases, which makes it possible to reduce the power consumption. The dominant conduction mechanisms in LRS and in HRS, respectively, had ohmic behavior and were space-charge-limited current (SCLC). The memory effect is explained by a model related to reduction and oxidation reactions, which cause the restoration and rupture of filaments in AlN film.

In order to clarify the mechanism of resistive switching in the $Al/TiO_2/Al$ structures, the microscopic changes in TiO_2 films and Al/TiO_2 interfaces that occurred after the SET process were investigated in [29]. In the case of films prepared at low temperatures (< 150 °C), the thickness of the top layer in the interface decreased after the SET process due to dislocations of the top layer in the interface resulting from the uniform migration of oxygen vacancies. The films prepared at high temperature had a TiO crystalline phase; this meant that the filaments were formed from local clusters of oxygen vacancies.

In [30], the effect of resistive switching of heterostructures $Al/TiO_x/TiO_2/Al$ was investigated. The switching was due to a SCLC mechanism controlled by localized traps in the TiO_x layer. An analytical model that includes the ratio of the densities of free and trapped carriers and shows the exponential energy distribution of traps was developed.

The review [31] notes that the universal capabilities of Scanning Probe Microscopy significantly expand the understanding of resistive switching mechanisms. In [32], a high-performance and low-power consumption (1 μW) resistive memory based on $Ni/GeO_x/SrTiO_x/TaN$ structures was reported. Low-power consumption resistive memory elements are also considered in [33]. It is noted that reducing the current during the RESET process is critical for obtaining high recording densities. Investigated structures $Ni/HfO_2/Si$ demonstrated unipolar resistive switching with low current (50 μA) and low power (30 μW) during RESET.

In [34], ZnO was used as an insulator in a resistive memory element. The *I–V* curves of structures Cu/ZnO/Pt and Cu/ZnO/Al in HRS are compared. It was found that rupture and restoration of the copper filament occurs at the cathode. It is argued that the filaments are most likely conical in shape: the base of the cone is located at the anode, and the top is at the cathode.

In [35], carbon doped with copper (C:Cu) was used as an insulator in a resistive memory element. Improved switching stability was shown. It was shown

that Cu atoms were agglomerated during rapid annealing and formed Cu-filaments. Thus, the structures did not require preliminary electroforming.

Resistive memory elements are also considered from a theoretical point of view. In [36], the *I–V* curves and defect distribution were calculated for solid-state devices in which acceptors are mobile. The devices had the form of MIM-structures, in which the insulator was a conductor with mixed ion-electronic conductivity, and the electrodes blocked the exchange. The result was nonlinear *I–V* curves, energy accumulation, hysteresis, negative resistance, and quasi-switching. In [37], it is argued that the functioning of all known resistive memory elements is determined by three mechanisms (also their combinations): (i) formation of continuous filament between two electrodes inside an insulator; (ii) formation of discontinuous conducting atomic chains between two electrodes inside an insulator; and (iii) rearrangement of charged defects/impurities near the interface between the semiconductor and the electrodes, as a result of changing the contact resistance. In [38], the analysis of the dependences of the resistive switching parameters on the dimensions of the elements was carried out. In particular, the analysis of the temperature dependence of the resistance made it possible to study of the resistance mode of the element (its state) depending on the dimensions of the filaments. In [39], the results of first-principles simulation of oxygen diffusion in amorphous HfO_x are given. The simulation result was in agreement with the experimental data.

1.2. Effect of resistive switching in memristive structures based on zirconium oxide and yttria-stabilized zirconia

Recently, when interest in memristive structures has increased due to their promising potential as a basis for creating a new generation of non-volatile memory devices [40], zirconium oxide was used as one of the main materials for microelectronics. In [41], resistive switching in thin films of non-stoichiometric zirconium oxide was investigated. The $Pt/ZrO_x/p^+$-Si structure demonstrated two

stable states of resistance. The composition of the ZrO_x thin films was monitored by X-ray photoelectron spectroscopy, which showed three layers: high resistance ZrO_2 top layer, transition region with medium resistance, and conductive bulk layer ZrO_x. Resistive switching was explained by the capture of electrons by excess Zr^+ ions and their emission in the transition layer, which controlled the distribution of the electric field inside the oxide and, thus, the electric current density. It is noted in [42] that binary metal oxides, such as ZrO_2, are simpler in preparation (in comparison with such compounds as $SrZrO_3$ and $Pb(Zr_xTi_{1-x})O_3$). In addition, binary metal oxides are more compatible with the generally accepted technology for preparation of metal-insulator-semiconductor structures. Zirconium oxide is considered as one of the main candidates for non-volatile memory devices, since it has such positive qualities as simple composition, high breakdown field, and high thermal sustainability.

In [15], the resistive switching parameters of ZrO_2 films, nanostructured by an array of Au nanoparticles (NPs), were investigated. TEM shows clearly visible Au NPs in ZrO_2 films. The investigated structures demonstrated two stable resistance states. The ratio of resistances in these two states was ~ 100. In [15], a significant effect of the presence of NPs on the resistive switching parameters was shown. It was assumed that the resistive switching is due to the capture and emission of electrons by Au NPs. When electrons were captured by NPs, an electric field appeared inside the zirconium oxide, which caused a decrease in conductivity and, thus, an increase in resistance, which corresponds to the RESET process. And vice versa, injection of electrons from NPs led to an increase in conductivity, which corresponds to the SET process. Based on the proposed mechanism of resistive switching, it is indicated that defects and traps in a zirconium oxide film play an important role. Zirconium oxide films, unlike single crystals, are imperfect objects with a large number of defects. In the investigated zirconium oxide films, there was two types of defects: defects formed «naturally» (dislocations, grain boundaries, and vacancies), and specially formed Au NPs, which act, for example, as electron traps. Obviously, it is not easy to control the formation of defects natural for this material, which leads to a scatter of

the resistive switching parameters from device to device. The formation of Au NPs is more controllable and makes it possible to additionally modulate traps in ZrO_2 films. As a result, the device yield, as shown in [15], can be significantly increased, since the concentration of traps is more uniform from device to device.

In [43], the influence of the material of the top electrode on the parameters of resistive switching of ZrO_2 films was investigated. It was assumed that the switching of the structure in the LRS was a field-controlled process, and the switching in the HRS was a current-controlled process. It is concluded that the origin of the resistive switching is associated with the properties of not only the internal volume of the insulator, but also the interface between the electrodes and the insulator.

It was shown in [44] that after the deposition of Ti top electrode the ZrO_2 film after electrical breakdown «recovered» and again demonstrated resistive switching. On the contrary, such a phenomenon was absent when Pt or Al top electrodes were deposited on the ZrO_2 film. The phenomenon of resistive switching recovering was explained by the effect of the formation of layers at the interface: TiO_z and ZrO_y, serving as a reservoir of oxygen and series resistance, respectively.

In [45], resistive memory elements based on ZrO_2 films irradiated with Ti ions were investigated. It was shown that such elements do not require preliminary electroforming and demonstrate a decrease in the scatter of the resistive switching parameters, namely, the voltage of the SET process and the resistance in the HRS. Moreover, it also resulted in high device yield (about 100%), low operating voltage, high switching rates, high ratio of resistances in HRS and LRS ($> 10^4$) and long storage times ($> 10^7$ s).

In [46], resistive memory elements based on ZrO_2 films irradiated with Au ions were investigated. The structures demonstrated reproducible unipolar resistive switching. It was shown that the investigated structures had a high device yield (almost 100%).

In [47], the resistive switching parameters of memory elements based on ZrO_2 films with an embedded Mo layer were investigated. It was shown that such elements

do not require preliminary electroforming and demonstrate excellent resistive switching parameters, which included low operating voltage (< 1.5 V), good endurance (> 10^3 cycles) and long storage time (> 10^7 s). It is concluded that oxygen vacancies induced by the presence of a Mo layer can enhance the formation of filaments and improve the resistive switching parameters.

In [48], the electrical properties of Ti/Co inclusions in resistive memory elements based on ZrO_2 films were investigated. Such elements demonstrated stable unipolar switching in the region of low negative voltages. To explain the switching mechanism, a physical model based on filament formation was used. It is noted that such elements have great potential for creating ultra-high-density non-volatile memory.

1.3. Mechanisms of electroforming and resistive switching in memristive structures based on transition metal oxides

At the time of writing this dissertation work, the understanding of resistive switching mechanisms is based mainly on the concept of filaments emerging inside the insulator under the influence of an electric field. Inside the filaments, the modification of the atomic structure of the material takes place, which leads to local increasing of the electron conductivity of the material.

At the initial moment of time, the application of an electric field to the structure leads to the flow of a low current value (~10^{-6} – 10^{-7} A) through defects in the insulator film. An increase in the electric field leads to an abrupt increase in the current, during which Joule heating occurs. An increase in temperature accelerates all diffusion processes (see [49]) and mass transfer in an electric field and, as a result, the rearrangement of the structure of the filament (filaments). In [50], it is discussed that during electroforming, a local, metal-rich conductive filament is formed through a controlled «soft break» of the insulator by applying a positive voltage to the top electrode. Oxygen ions move from the insulator to the top electrode and surrounding

areas. During the RESET process, a positive voltage is applied to the bottom electrode and oxygen ions move back into the filament, recombining with the vacancies and switching the device to a HRS.

In [51], a schematic representation of the physical picture of bipolar resistive switching was given. Switching between HRS and LRS is explained by the restoration and rupture of filaments in the oxide, which can consist of oxygen vacancies (serving as traps) or metal ions [24, 52]. It is assumed that the Joule heating [53] and the migration of oxygen ions/vacancies under the influence of an electric field [54] will play an important role in switching. The current in such structures is mainly determined by the tunneling of electrons from the cathode to the nearest trap in the insulator, subsequent electron hopping through the trap chain, and electron tunneling into the anode. Let's say a voltage is applied to the structure so that the left and right electrodes serve as the cathode and anode, respectively. An electron from the cathode must punch through the breaking gap before passing through the circuit to the anode on the right side. Therefore, the conduction through this circuit is determined by the bottleneck in the gap. Since the tunneling probability depends exponentially on the gap size, the current through the structure has an exponential dependence on the gap size. That is, changing the gap size can have a significant effect on the state of the HRS. The authors of the work also argue that the length of the filament rupture region is a function of voltage and time.

In [55], the resistive switching mechanism in structures Pt/NiO/W was investigated. *I–V* curves showed a completely linear behavior. It was assumed that this is due to the fact that the filaments were formed from a continuous metallic phase (for example, Ni). It is noted that the Pt/NiO/W structures in HRS demonstrate a semiconductor conduction mechanism, while in LRS, it is metallic.

In [56], a model of defect generation in the structures Ti/HfO_2:Si/TiN was demonstrated. It was shown that with a small number of resistive switching, the filament size was controlled by the magnitude of the currents compliance, while the excessive growth of filaments was induced by parasitic capacitance. With a large

number of resistive switching, the filament size in both cases increased with increasing defect concentration.

In [57], it was noted that the mechanism of resistive switching is based on the conductivity of the impurity band, without ionic motion. In this case, traps provide a memory effect. It was shown in [58] that the migration of oxygen ions in YSZ is a two-step process: the formation of active oxygen vacancies and the hopping of oxygen ions from one active vacancy to another.

In [59], a model was proposed that explains the specific features of the conductivity of YSZ by the fact that at low temperatures oxygen vacancies form inactive clusters, which require certain energy to decay. Thus, the activation energy of ionic conduction is the sum of two quantities: the energy of injection of a vacancy from a cluster, E_a, and the migration energy of a vacancy, E_m. An analysis of the temperature dependence of the Gibbs free energy and entropy showed [60] that E_a = 0.52 eV and E_m = 0.73 eV for YSZ (12 mol. % Y_2O_3).

In [61], the resistive switching mechanisms in structures Ti/HfO_x/TiN at ultra cryogenic temperature (4 K) were investigated. It is shown that the continuous *I–V* curve obtained at room temperature was replaced by the discontinuous one obtained at ultra cryogenic temperature. The quantization of the *I–V* curve is associated with the quantization of the filament conductivity [62, 63]. It was noted that during the RESET process the conduction mechanism changed from ohmic (for LRS) to Schottky emission [59]. This suggests that the filament in the LRS was oxidized layer by layer by oxygen ions migrating from the HfO_x/TiN interface. The oxidation reaction of the filament started from the first layer close to TiN. During this, the effective cross section of the filament decreased, which caused a change in the resistance of the structure. Since the resistance value is inversely proportional to the effective area determined by the number of atoms in the cross section of the filament, the ratio of resistance with and without atom i is equal to $R_{N-i} / R_N = N / N\text{-}i$. Therefore, the quantized change in resistance during the RESET process can be explained by reactions occurring at the atomic level in the filaments. In [59], the

results of simulation of described process were shown. The simulation results were in good agreement with the experimental ones. It was concluded that the filament in the investigated memristive structure in the LRS was formed from elementary Hf atoms.

It was shown in [64] that the conduction mechanism in the HRS of the structure Ti/ZrO_2/Pt had ohmic behavior at low voltages; this indicates that the number of thermal generated free carriers in the ZrO_2 film is greater than that of the introduced charge of carriers. At high voltages, the conduction mechanism was explained by the SCLC mechanism. The SCLC mechanism was caused by injected excess carriers dominating the thermal generated free carriers. The conduction in the SCLC mechanism was associated with shallow traps. The application of even higher voltage led to the filling of the traps and the formation of a space charge near the electrode, which, in turn, prevented their father filling. With a further increase in voltage, the filaments were completely formed, which switched the structures to LRS, in which ohmic conductivity prevailed.

It should be noted the studies demonstrating the experimental detection of filaments in memristors based on transition metal oxides. For example, it was possible to observe filaments by Transmission Electron Microscopy [65] and Atomic Force Microscopy [66, 67].

1.4. Conclusion of the literature review

From the literature review, it follows that at the time of writing this dissertation work, questions remain related to the determination of resistive switching mechanisms in structures based on transition metal oxides and the choice of an active layer material that provides optimal values of the parameters of memory elements, integration into a standard CMOS-process, thermal and irradiation sustainability.

CHAPTER 2. Preparation of memristive MIM- and MIS-structures based on yttria-stabilized zirconia and methods for investigation of structural and electrical properties

This chapter describes the methods of preparation, electron microscopic and probe investigations, and investigations of the electrical properties of memristive metal-insulator-metal (MIM) and metal-insulator-semiconductor (MIS) structures based on yttria-stabilized zirconia (YSZ). Section 2.1 describes the methods of preparation of the investigated structures. Section 2.2 discusses the main techniques of electron microscopic and probe investigations of memristive structures (Atomic Force Microscopy (AFM), Transmission Electron Microscopy (TEM), and Optical Microscopy). Section 2.3 describes methods of investigation of electrical properties of memristive structures.

2.1. Preparation of memristive MIM- and MIS-structures based on yttria-stabilized zirconia

This section describes the methods of preparation of memristive MIM- and MIS-structures based on YSZ, which were the objects of this dissertation work.

The investigated structures were prepared by radio-frequency magnetron sputtering at the Laboratory of Physics and Technology of Thin Films, Research Institute for Physics and Technology, Lobachevsky State University of Nizhny Novgorod (by Engineer I.N. Antonov) using the Torr International 2G1-1G2-EB4-TH1 vacuum setup. The method of radio-frequency magnetron sputtering is modern, one of the most widespread methods of obtaining high quality metal, insulator, and semiconductor layers without violating the stoichiometric composition and is highly stable and reproducible [68]. The principle of radio-frequency magnetron sputtering is based on the formation of annular plasma above the cathode surface as a result of the collision of electrons with molecules of the working gas. Positive ions, formed in

the discharge, are accelerated towards the cathode, bombard its surface, knocking out material particles from it, which settle on the substrate in the form of a thin or island film.

In this dissertation work, the radio-frequency magnetron sputtering method was used to form metal electrodes Au/Zr, YSZ films, and Au nanoparticles (NPs) inside YSZ films.

MIM-structures were prepared on Si(001) substrates, coated with a SiO_2 (~ 0.5 μm), on top of which TiN layers (25 nm) with a Ti sublayer (25 nm) were deposited. MIS-structures were prepared on *n*-Si(100) substrates with electrical resistivity 4.5 Ω·cm, coated with a tunnel-thin SiO_2 layer by the chemical method (sequential treatment of the silicon surface, first in Hydrofluoric Acid, and then in a mixture of Sulfuric Acid with Hydrogen Peroxide). The molar fraction of the stabilizing oxide Y_2O_3 in the pressed powder $ZrO_2(Y)$ target material, from which YSZ films with a thickness of 40 nm were prepared, was ≈0.12. Au electrodes with 3 nm thick Zr sublayers were prepared on the surface of the YSZ layer. Depending on the purpose of the study, the thickness of the Au electrode varied (20 and 40 nm). Au films with a thickness of 20 nm, on the one hand, had sufficient electrical conductivity, and on the other hand, were semi-transparent in the visible wavelength range. Au films with a thickness of 40mm demonstrated the resistance typical of bulk gold. The area of the top metal electrodes was set by the pattern of the shadow mask ($1.2 \cdot 10^{-3}$ and $1.0 \cdot 10^{-2}$ cm^2).

In addition, by layer-by-layer deposition of YSZ (20 nm)/Au (1 nm)/YSZ (20 nm) sandwich structures with subsequent annealing (in Ar atmosphere at 450 °C for 2 minutes), MIM-structures with two-dimensional arrays of Au NPs inside YSZ films were prepared.

To reduce the density of surface states in MIS-structures, tunnel-transparent SiO_2 interface layers were prepared at the YSZ/*n*-Si interface by chemical oxidation (the natural oxide from the surface of the Si wafers was previously removed in a 0.5 mol/L aqueous solution of Hydrofluoric Acid), and then passivating Sb

layers ~ 2 nm thick were deposited by the method of pulsed laser deposition at the Research Institute for Physics and Technology, Lobachevsky State University of Nizhny Novgorod (by Senior Researcher, Ph.D. B.N. Zvonkov).

To investigation of accumulation of electric charge in Au NPs, the method of Kelvin Probe Force Microscopy (KPFM) was applied. For these studies, a special series of samples was prepared with single-layer arrays of Au NPs embedded in YSZ films 10 nm thick on n^+-Si(001) substrates with electrical resistivity 0.005 Ω·cm.

Together with an industrial partner Russian Federal Nuclear Center – All-Russian Scientific Research Institute of Experimental Physics «Measuring Systems Research Institute named after Yu.Ye. Sedakov» memristive devices cross-point type of various areas (5×5, 10×10, 20×20, 50×50 и 100×100 μm^2) were prepared on the basis of MIM-structures Au (40 nm)/Zr (8 nm)/YSZ (40 nm)/TiN (25 nm)/Ti (25 nm)/SiO_2 (500 nm)/Si and Au (20 nm)/Ta (8 nm)/YSZ (10 nm)/Ta_2O_5 (10 nm)/TiN (25 nm)/Ti (25 nm)/SiO_2 (500 nm)/Si. These devices were prepared using multistage photolithography.

To investigation of local stochastic resistive switching of YSZ film on a conductive substrate by the method of Conductive Atomic Force Microscopy (CAFM) was applied. For these studies, the YSZ films (≈ 4 nm in thickness) were deposited onto TiN/Ti/SiO_2/Si substrate mentioned above.

2.2. Methods of electron microscopic and probe investigations of memristive MIM- and MIS-structures based on yttria-stabilized zirconia

This section discusses the main methods of electron microscopic and probe investigations.

The surface morphology of the substrates and memristive structures was investigated by AFM using an atomic force microscope «Solver PRO» (NT-MDT, Russia) at the Laboratory of Scanning Probe Microscopy, Research and Education Center «Physics of Solid State Nanostructures», Lobachevsky State University of

Nizhny Novgorod (by Leading Researcher, Associate Professor, Dr. D.O. Filatov). This method allows obtaining information with nanometer/angstrom resolution.

Structural analysis of the samples was carried out by TEM on cross sections using a Jeol JEM 2100 transmission electron microscope at the Laboratory of Transmission Electron Microscopy, Research and Education Center «Physics of Solid State Nanostructures», Lobachevsky State University of Nizhny Novgorod (by Leading Researcher, Professor, Dr. D.A. Pavlov and Engineer, Ph.D. A.I. Bobrov). The TEM method is highly informative and is used to study of the structure of a sample on the surface and in volume. This experimental setup allows achieving a resolution of ~ angstrom.

Optical microscopy is used to control the quality of the surface of memristive structures, including memristive devices. The method allows obtaining an image of an object with submicron dimensions. In this dissertation work, such studies were carried out using a Leica DM 4000M optical microscope at the Laboratory for Surface Preparation of Semiconductors and Solids, Research Institute for Physics and Technology, Lobachevsky State University of Nizhny Novgorod (by Head of Laboratory V.E. Kotomina).

The used methods are one of the modern and highly informative methods for obtaining information about the state of the surface and volume of the samples.

2.3. Methods of investigation of electrical properties of memristive MIM- and MIS-structures based on yttria-stabilized zirconia

This section describes methods of investigation of electrical properties of memristive MIM- and MIS-structures based on YSZ.

The electrical properties of the memristive structures were investigated using a semiconductor device analyzer Agilent B1500A (resolution 0.1 fA and 0.5 μV). Cyclic current-voltage characteristics (*I*–*V* curves) were measured, as well as high-frequency ($f = 100$ kHz), low-frequency ($f = 1$ kHz), and quasi-static capacitance-

voltage characteristics (*C–V* curves) and conductance-voltage characteristics (*G–V* curves) of MIM- and MIS-structures, as well as theirs temperature dependencies in the temperature range 77 – 510 K. The voltage across the structure corresponded to the potential of the top electrode relative to the potential of the substrate. To study of the processes of ion migration polarization in MIM-structures, dynamic *I–V* curves and depolarization currents [69] were measured additionally. From the results of these measurements, the temperature dependences of the depolarization charge and the concentration of oxygen ions were obtained, from which the activation energy of ion migration was determined E_a.

The KPFM method was applied to study of the process of accumulation of electric charge in Au NPs. This method is designed to measure the spatial distribution of electric potential over the surface of solids, microelectronic devices, and so on [70]. The KPFM method is based on measuring the response of the AFM-cantilever when a sinusoidal alternating voltage is applied between the conducting AFM-probe and the surface of the sample under study with a frequency that coincides with the frequency of the natural oscillations of the AFM-cantilever. In this dissertation work, the study by the KPFM method was carried out using AFM «Solver PRO» (NT-MDT, Russia) in an air atmosphere at room temperature. Probes NT-MDT NSG-11 with Pt coating were used. The radius of curvature of the AFM-probe tip R_p, according to the passport data, was ≈ 35 nm. Point charge injection into Au NPs was carried out in the contact mode by applying a voltage pulse V = 3 V with a duration of ~ 1 s between the AFM-probe and the n^+-Si substrate. At the same time, the waveforms of the current through the AFM-probe were analyzed to make sure that there was no breakdown of the nanocomposite insulator film. The temporal dynamics of the potential, induced by the injected charge, was studied by repeated scanning of the film surface area around the point of charge injection at certain time intervals from the moment of injection.

The response of the memristive devices based on YSZ/Ta_2O_5 (with area 20×20 μm^2) to the noise signal (as well as investigation of the stochastic

resonance phenomenon) was investigated using a home-made setup shown schematically in Figure 1. Before the study, memristive devices were subjected to preliminary electroforming using Agilent B1500A semiconductor device analyzer.

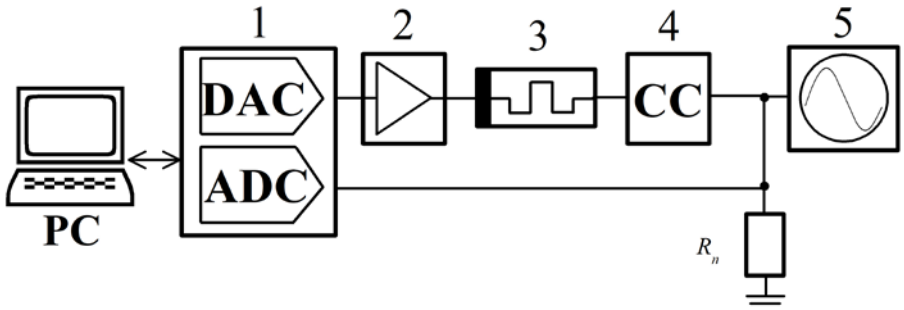

Figure 1. Schematic representation of the experimental setup for investigation of response of the memristive device based on YSZ/Ta_2O_5 to the noise signal, consisting of DAC/ADC unit (1), amplifier (2), memristive device (3), current compliance (4), oscilloscope (5), and load resistor (R_n)

The bias voltage, applied to the memristive device, was supplied by the digital-to-analog converter (DAC) of National Instruments USB-6211 computer-controlled DAC/ADC unit, operated as a programmable voltage source under LabView 2016 software. The output voltage range of the DAC is ± 10 V; the maximum output bit rate is 250 kHz. The voltage from the DAC output was then amplified up to the maximum magnitude 25 V by a wide bandpass dc operation voltage amplifier. The bandpass of the amplifier is 0 to 2 MHz. In order to investigate the response of the memristive device based on YSZ/Ta_2O_5 to the noise signal, a digitally synthesized external noise signal was applied. The digitally synthesized Gaussian white noise signal is generated using a random number generator of ADSViewer-2 (v.015) software module [71] and is saved in a control PC. ADSViewer-2 software system is running under LabVIEW 6.1 software system and allows generating the series of random numbers with Gaussian distribution utilizing either the summation of several series of random numbers with uniform distribution or a nonlinear transformation of a series of random numbers with uniform distribution. The noise data array contains 2^{16} random numbers. Before measurements, the noise data array is read into

the random access memory (RAM) of the control PC. The magnitude of the noise signal is defined by scaling the original noise data and characterized by the output voltage standard deviation σ_V. Finally, a constant offset voltage V_{offset} is added to the noise data. The resulting noise signal is played back, sent to the DAC of the DAC/ADC unit, in an endless cycle with predefined bit rate equal to the maximum bit rate provided by the DAC, with 250000 numbers per second that corresponds to the white noise spectrum bandwidth from 0 to 250 kHz. The output signal was taken from the load resistor R_n = 1 kΩ and was supplied to the analog-to-digital converter (ADC) of the National Instruments USB-6211 DAC/ADC unit. The maximum sampling rate of the ADC is 250 kHz. The output signal waveform was monitored by Agilent 3000A digital oscilloscope.

The CAFM method was applied to study of the local stochastic resistive switching of YSZ film on a conductive substrate. Schematic representation of the experimental setup and sample cross-section, are shown in Figure 2.

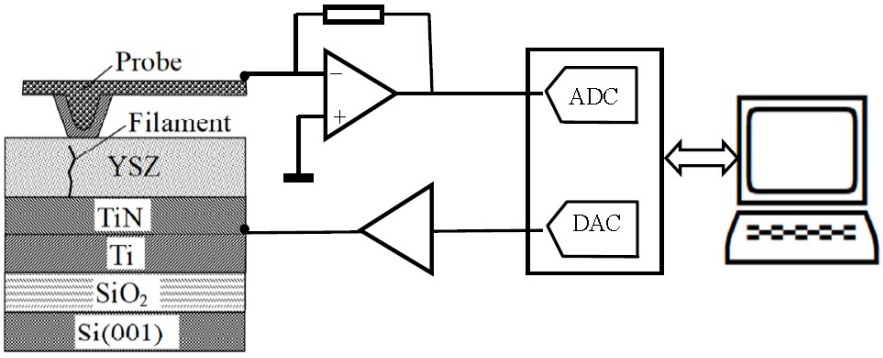

Figure 2. Schematic representation of the experimental setup to investigation of local stochastic resistive switching

The resistive switching was investigated in ultra high vacuum (UHV) environment (the base residual gas pressure ~ 10^{-10} Torr) using Omicron UHV AFM/STM LF1 installed into Omicron MultiProbe RM UHV setup at the Laboratory of Scanning Probe Microscopy, Research and Education Center «Physics of Solid State Nanostructures», Lobachevsky State University of Nizhny Novgorod (by Leading

Researcher, Associate Professor, Dr. D.O. Filatov; Senior Researcher, Ph.D. D.A. Antonov). NT-MDT NSG-11 DCP probes covered by diamond-like coating were used. The bias voltage applied between the CAFM-probe and the TiN conductive layer was supplied by the DAC of Lcard E502 PC-controlled ADC/DAC unit employed as an external programmable voltage source. Before the study, YSZ film was subjected to preliminary electroforming: a voltage $5 – 6$ V was applied between the CAFM-probe and the TiN conductive layer until the probe current reached 10 – 15 nA. Afterwards, the cyclic *I–V* curves of the CAFM-probe/sample contact (virtual memristor) were measured in order to ensure the proper resistive switching. In order to investigate the impact of noise on the virtual memristor response, a digitally synthesized external noise signal with predefined magnitude was applied between the CAFM-probe and the substrate using Lcard ADC/DAC unit control software. The digitally synthesized Gaussian white noise signal was generated using a random number generator of ADSViewer-2 (v.015) software module mentioned above. In the experiment, the noise signal was played back, sent to the DAC of Lcard E502 ADC/DAC unit, in an endless cycle with predefined bit rate. The maximum bit rate was 10^6 numbers per second, which corresponds to the white noise spectrum bandwidth from 0 to 1 MHz. The signal from the DAC output of Lcard E502 ADC/DAC unit was amplified up to the maximum magnitude of 10 V by a wide bandpass dc operation voltage amplifier and supplied to the external bias voltage input of Omicron UHV AFM/STM LF1. In order to obtain a wide-band external white noise signal between the CAFM-probe and the sample, the original in-vacuum operation amplifier in the STM preamplifier (current-voltage converter) of Omicron UHV AFM/STM LF1 was replaced by an external (ex-vacuum) preamplifier with the bandpass of 0 to 7 MHz. The probe current signal was taken from the «Tip current» output of Omicron SCALA AFM/STM electronic control unit and supplied to the ADC of Lcard E502 ADC/DAC unit operated in the buffering mode. The maximum sampling rate of the ADC was 2 MHz.

The methods of investigation of electrical properties described in this section are among the most modern, highly informative, non-destructive, non-polluting, and can be carried out in an air atmosphere.

CHAPTER 3. Structural and electrical properties of initial (before electroforming) memristive MIM- and MIS-structures based on yttria-stabilized zirconia

Memristive metal-insulator-metal (MIM) and metal-insulator-semiconductor (MIS) structures demonstrate the effect of resistive switching, as a rule, only after electroforming. This chapter presents investigations of memristive structures in initial state, i.e. before electroforming. Section 3.1 discusses the structural properties of MIM-structures based on yttria-stabilized zirconia (YSZ). In the preparation of MIS-structures, the same conditions for the deposition of the insulator and the top electrode, which were used in the preparation of MIM-structures, were used. In Section 3.2, the dielectric properties and the mechanism of electronic conduction of the initial memristive structures based on YSZ are considered, and the ion transfer processes in the initial memristive structures based on YSZ are analyzed. Section 3.3 presents the results of investigations of the electrical properties of the initial MIM-structures based on YSZ films, nanostructured by an array of Au nanoparticles (NPs). Section 3.4 discusses the electrical properties of the initial MIS-structures based on YSZ with high and low values of the surface states density. Section 3.5 summarizes the results obtained in Chapter 3.

3.1. Structural properties of memristive structures based on yttria-stabilized zirconia

This section presents the results of investigations of the morphology of interfaces and the crystal structure of YSZ films. Figure 3 shows a schematic representation of the investigated memristive MIM-structure.

To assess the surface quality of the TiN bottom electrode, measurements of its topography were performed using the Atomic Force Microscopy (AFM) method. It was found that the TiN surface had a sufficiently high homogeneity and a low

roughness value (~ 0.5 nm). This made it possible to use TiN as the conducting bottom electrode of the memristive MIM-structure.

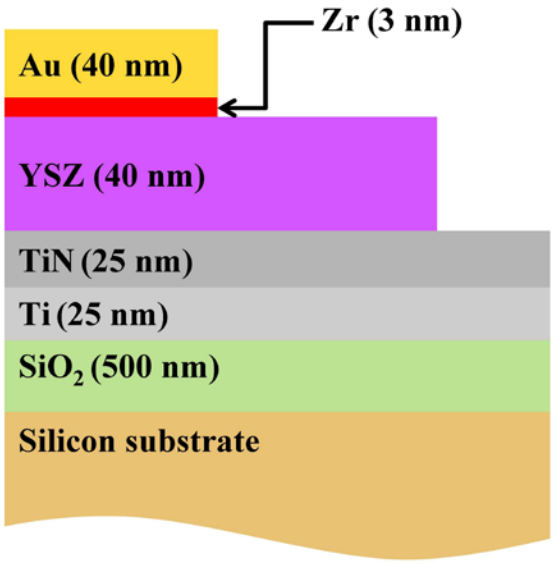

Figure 3. A schematic representation of the investigated structures

To obtain detailed information about the structural properties of the samples, the high-resolution Transmission Electron Microscopy (TEM) method was used. Figure 4 shows an overview and detailed TEM image of the cross section of the investigated structure. According to TEM data (Figure 4a), the insulating SiO_2 sublayer on a silicon substrate was amorphous.

Figures 5 – 7 shows TEM images of the cross section of TiN/Ti bottom electrode, YSZ film, and Au/Zr top electrode of the memristive MIM-structure. Table 1 shows the values of the nominal and real (obtained using the TEM method) thicknesses of the layers of the memristive MIM-structure.

It was shown that the YSZ layers had a columnar polycrystalline structure (Figure 6), as in [72, 73], and a well-developed interface with the top electrode, as indicated by irregularities with sizes of 1 – 5 nm. The positions of these irregularities corresponded to the positions of grain boundaries in the oxide layer. The grain boundaries were highlighted in the TEM image by a light contrast, which reflected the presence of a high concentration of vacancy defects, and had a thickness

of 1 – 3 nm, depending on the distance from the top electrode.

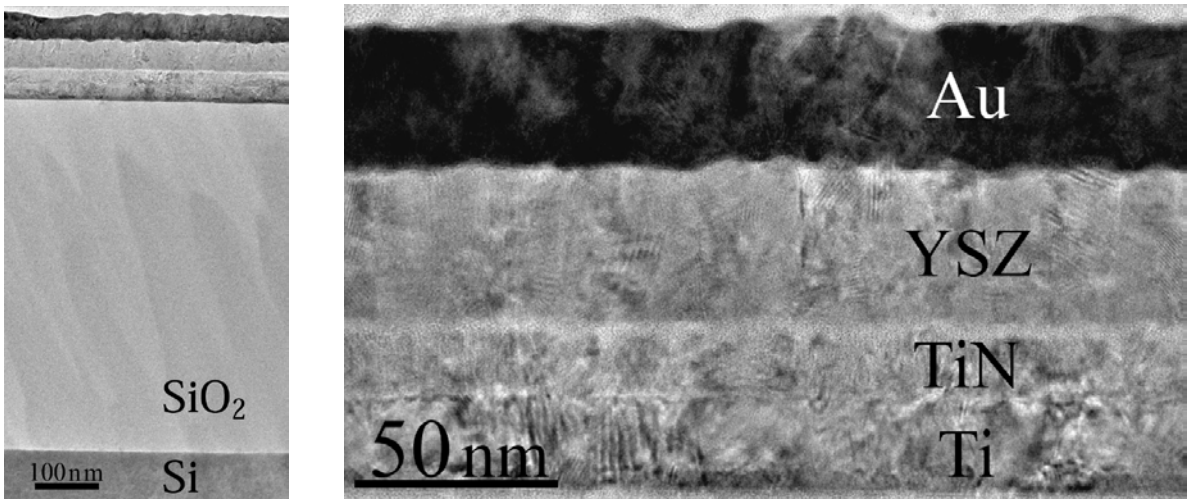

(a) (b)

Figure 4. An overview (a) and detailed (b) TEM image of the cross section of the structure, a schematic representation of which is shown in Figure 3 [A1, A11]

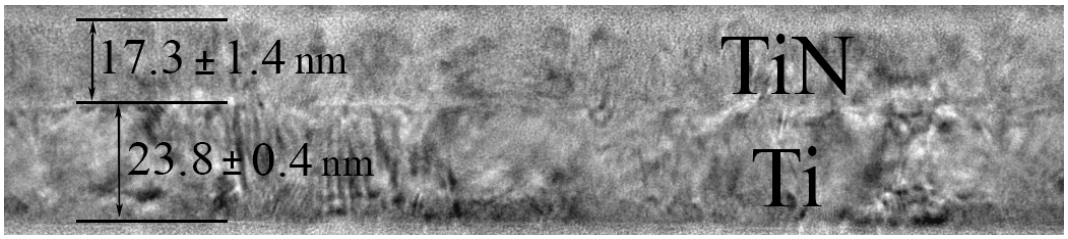

Figure 5. TEM image of the cross section of TiN/Ti bottom electrode of the investigated structure

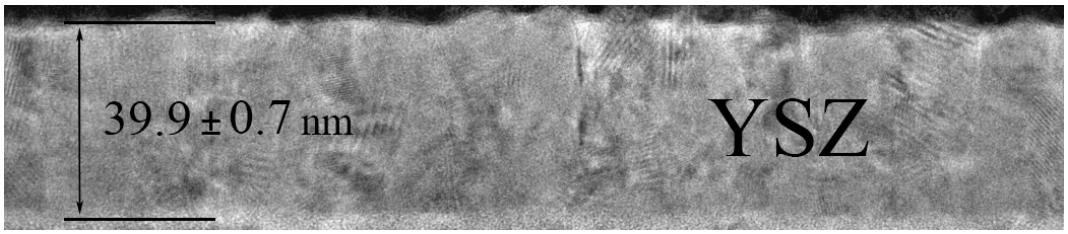

Figure 6. TEM image of the cross section of YSZ film of the investigated structure

Note that the roughness of the YSZ film at the interface with the top electrode was more significant than at the interface with the bottom electrode. This fact is due to the polycrystalline structure of the YSZ film. Using of YSZ polycrystalline films in such structures, in contrast to amorphous one, seems to be more appropriate. In amorphous

films, unlike polycrystalline ones (with crystallites stabilized in the cubic phase), phase transitions can occur during resistive switching, which can lead to instability of resistive switching parameters of structures based on such films.

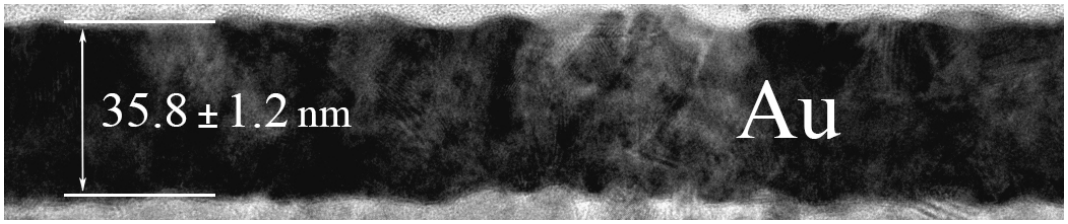

Figure 7. TEM image of the cross section of Au/Zr top electrode of the investigated structure

Table 1. Values of nominal and real thicknesses of layers of the memristive MIM-structure Au/Zr/YSZ/TiN/Ti/SiO_2/Si.

Layer	Nominal thickness, nm	Real thickness, nm
Au	40	35.8 ± 1.2
Zr	3	–
YSZ	40	39.9 ± 0.7
TiN	25	17.3 ± 1.4
Ti	25	23.8 ± 0.4
SiO_2	500	545.8 ± 2.0

The top electrode was a polycrystalline Au layer. The TEM image (Figure 7) shows the top electrode/insulator interface. However, due to a well-developed interface, a thin Zr sublayer against the background of Au and insulator cannot be identified.

The TEM method was used to study of memristive MIM-structures based on YSZ with embedded Au NPs. The preparation technique for such structures is described in Chapter 2. Figure 8 shows a TEM image of a sandwich structure YSZ (20 nm)/Au (1 nm)/YSZ (20 nm)/*n*-Si. The TEM results indicated that the island Au film after annealing coagulated into NPs, concentrated within a layer ~ 10 nm

thick, of predominantly spherical shape with a diameter $D = 2.3 \pm 0.4$ nm, an average distance between NPs 3.7 ± 1.6 nm, and surface density $N_s \sim (7.3 \pm 6.3) \cdot 10^{12}$ cm^{-2}. The corresponding bulk density in a layer 10 nm thick was $N \sim 7.3 \cdot 10^{18}$ cm^{-3}. In this case, the volume fraction of Au NP in the above layer was $N_V \sim 1.1 \cdot 10^{-2}$.

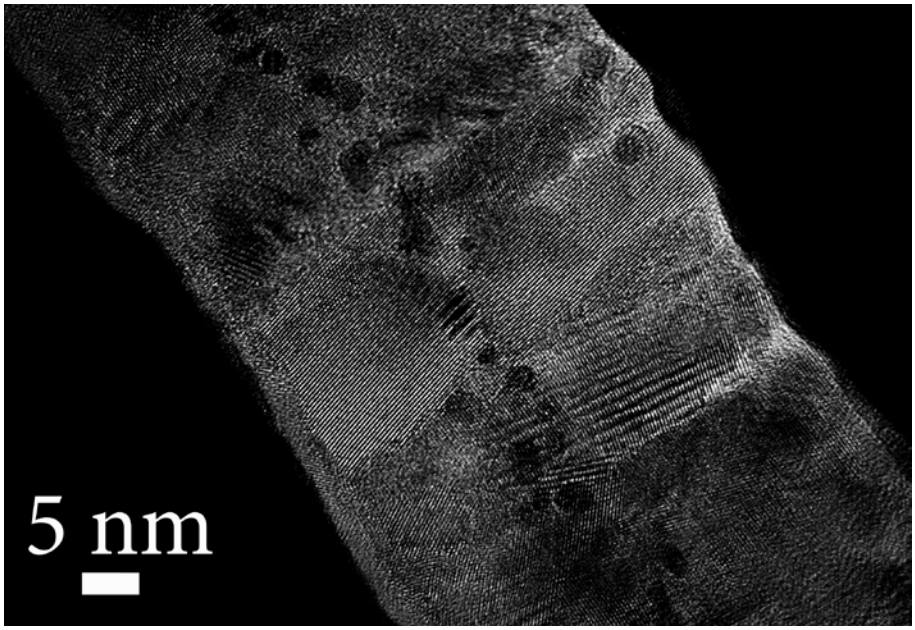

Figure 8. TEM image of the cross section of YSZ/Au/YSZ/*n*-Si with an effective Au film thickness of 1 nm after annealing at a temperature of 450 °C for 2 minutes [A2, A12]

The TEM data also indicated that the Au NPs had a monocrystalline structure, and the YSZ layers had a columnar polycrystalline structure with a crystallite size of 5 – 15 nm. It should be noted that annealing at a temperature of 450 °C satisfies the requirements for low-temperature annealing, which are imposed on memristive MIM-structures.

Note that the parameters of the layers of the top electrode and YSZ in the MIM- and MIS-structures did not differ.

Thus, this section presents the results of investigation of the initial memristive MIM- and MIS-structures by electron microscopic and probe methods described in Section 2.2. Detailed information about investigated structures, including nanostructured by an array of Au NPs, was obtained.

It was found that the surface of the bottom electrode had a sufficiently high homogeneity and a low roughness value and YSZ films had a nanocrystalline structure and a well-developed interface with the top electrode.

It was found that nanoscale gold layers in a sandwich structure YSZ/Au/YSZ during annealing coagulated into two-dimensional arrays of NPs with a diameter 2.3 ± 0.4 nm, an average distance between NPs 3.7 ± 1.6 nm and surface density $(7.3 \pm 6.3) \cdot 10^{12}$ cm^{-2}.

3.2. Electrical properties of memristive MIM-structures based on yttria-stabilized zirconia

This section presents the results of investigation of the electrical properties of initial (before electroforming) memristive MIM-structures based on YSZ. This is important for understanding the mechanisms, responsible for the processes, occurring during electroforming and resistive switching. Section 3.2.1 discusses the dielectric properties and the mechanism of electronic conduction of the initial memristive structures based on YSZ. Section 3.2.2 shows the results of determining the parameters of ion transfer in the YSZ by methods of studying ion migration polarization.

3.2.1. The dielectric properties and the mechanism of electronic conduction of the memristive MIM-structures based on yttria-stabilized zirconia

This section presents the results of investigation of current-voltage characteristics (*I–V* curves) and small-signal measurement of admittance of the initial memristive MIM-structures Au/Zr/YSZ/TiN/Ti/SiO_2/*n*-Si, the structural properties of which are considered in Section 3.1. The values of the dielectric constant of YSZ, dielectric loss tangent and resistances of structures were obtained from the parallel equivalent circuit for capacitor (an equivalent circuit replacing a real capacitor with a

resistor and capacitor connected in parallel). The results of determining the mechanism of the electronic current in the investigated structures are presented.

Figures 9 and 10 show frequency dependences of capacitance (C), resistance (R) and dielectric loss tangent ($tg\delta$) of memristive MIM-structure Au/Zr/YSZ/TiN/Ti/SiO_2/n-Si ($S \sim 1 \cdot 10^{-2}$ cm^2). The parameters were obtained from the parallel equivalent circuit for capacitor [74].

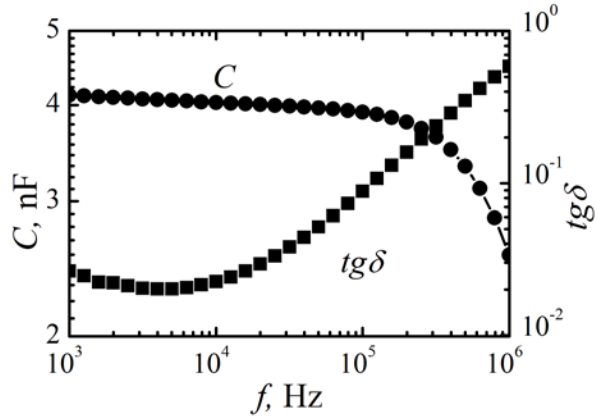

Figure 9. Frequency dependences of capacitance and dielectric loss tangent of investigated MIM-structures in initial state

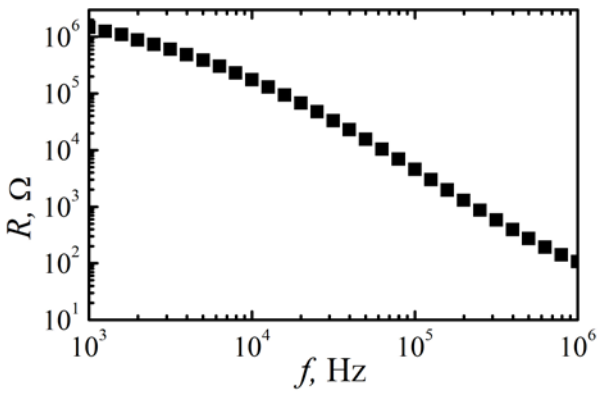

Figure 10. Frequency dependence of resistance of investigated MIM-structures in initial state

Small-signal measurements of admittance [74, 75] were used to determine the values of the dielectric constant (ε_1, ε_2) of YSZ (determined from the value of the capacitance measured from the parallel equivalent circuit for capacitor), the dielectric loss tangent ($tg\delta_1$, $tg\delta_2$) and resistances (R_1, R_2) of the structure, where 1 refers to a frequency of 1 kHz, and 2 – to a frequency of 100 kHz (Table 2). It should be noted that the values of the dielectric constant of YSZ are in good agreement with the data available in the literature (see, for example, [76]).

Leakage current in the investigated memristive structures can be associated with the peculiarities of the electrode morphology (see Section 3.1). On the one hand, the presence of these peculiarities is preferable, since they are concentrators of the electric field at the electrode/insulator interface, and their presence can lead to a

decrease in the electroforming and resistive switching voltages. On the other hand, the presence of such peculiarities in the initial structures decreases the range of currents, in which the resistive memory elements can operate, which decreases the possibility of varying the parameters of the memory elements during their manufacture.

The main mechanisms of conduction in insulators are shown in Table 3 [77].

Table 2. Parameters of the investigated memristive structure in initial state, obtained from small-signal measurements of admittance measured from the parallel equivalent circuit for capacitor [A1].

ε_1	ε_2	$tg\delta_1$	$tg\delta_2$	R_{p1}, Ω	R_{p2}, Ω
23	22	$2.6\cdot10^{-2}$	$8.9\cdot10^{-2}$	$1.5\cdot10^{6}$	$4.6\cdot10^{3}$

Table 3. The main mechanisms of conduction in insulators.

Mechanism	Expression
Schottky Emission	$J = AT^2 \exp\left[\frac{-q(\varphi_b - \sqrt{qE/4\pi\varepsilon})}{kT}\right]$
Poole-Frenkel Emission	$J = E \exp\left[\frac{-q(\varphi_b - \sqrt{qE/\pi\varepsilon})}{kT}\right]$
Tunnel or Field Emission	$J = E^2 \exp\left[\frac{-4\sqrt{2m^*}(q\varphi_b)^{3/2}}{3q\hbar E}\right]$
Space-Charge Limited	$J = \frac{8\varepsilon\mu V^2}{9d^3}$
Ohmic	$J = E \exp\left[\frac{-\Delta E_{ae}}{kT}\right]$
Ionic Conduction	$J = \frac{E}{T} \exp\left[\frac{-\Delta E_{ai}}{kT}\right]$

The table uses the following notation: J – current density, A – effective Richardson constant, φ_b – barrier height, E – electric field, ε – dielectric constant, k – Boltzmann constant, m^* – effective mass, d – insulator thickness, ΔE_{ae} – activation energy of electrons, and ΔE_{ai} – activation energy of ions. Note that conditions, when several mechanisms are involved in the current transfer processes, are possible.

In order to clarify the mechanism of electronic current transfer, the *I–V* curves of the initial MIM-structure, measured at $V < 0$, are shown in Schottky coordinates (Figure 11).

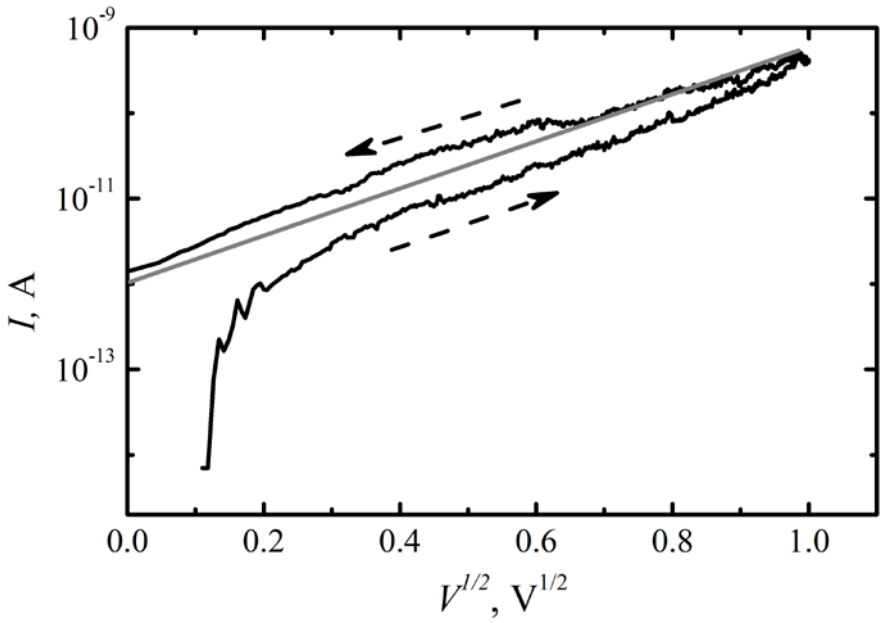

Figure 11. *I–V* curves, measured at $V < 0$ and plotted in Schottky coordinates, of the initial MIM-structure. Dashed arrows shows the direction of the voltage sweep

The direction of the hysteresis corresponded to the movement of oxygen ions (vacancies) or the injection of electrons into the YSZ from the top electrode with subsequent capture by traps. From the ohmic section of the *I–V* curve of the initial structure, the electrical resistivity of the YSZ layer was estimated (~ 10^{14} Ω·cm). Assuming that the current transfer mechanism was a Schottky mechanism, the barrier height φ_b was determined using the following equation:

$$\varphi_b = \frac{kT}{q \ln\left[I_s / AT^2 S \right]}, \qquad (1)$$

where q is the elementary charge, A = 120 m^*/m (m^*/m = 0.3 – the ratio of the electrons effective mass of zirconium oxide at room temperature [78] to the electron mass in vacuum), S is the top electrode area; current I_s was determined by extrapolation of the I–V curve in Schottky coordinates up to intersection with the current axis at V = 0. The φ_b value in the initial structure was 0.92 eV.

The presence of such an activation mechanism of electronic conduction was confirmed by studying the temperature dependences of the I–V curves at very slow voltage sweep rates (0.01 V/s). Figure 12 shows the dependences of the current on the inverse temperature, obtained at different values of negative voltage.

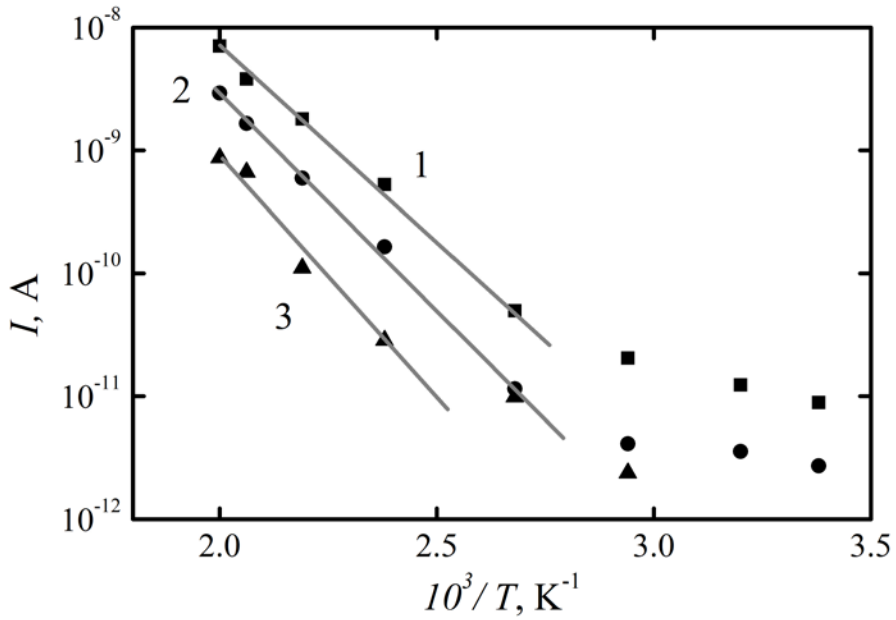

Figure 12. Dependences of the current on the inverse temperature, obtained at different values of negative voltage V, V: -2 (1), -1 (2), and -0.5 (3)

The data, presented in Figure 12, demonstrated the exponential behavior of the current dependencies in the region of relatively high temperatures. The activation

energy E_a, determined from the slope of these dependencies, increased linearly with decreasing square root of the voltage. Extrapolation of this dependence to V = 0 V made it possible to obtain a value of 0.90 eV, close to the value of the barrier height φ_b, determined from the I–V curves in Schottky coordinates.

The energy band diagram of the structure Zr/YSZ/TiN (Figure 13) with the parameters given in Table 4 allows a more detailed understanding of the current transfer mechanism. Such point defects as C-defects (associated with oxygen vacancies) and T-defects (associated with oxygen divacancies), presented in YSZ, has high concentrations (~10^{20} and ~10^{19} cm^{-3}, respectively) and are deep centers for conduction electrons. Therefore, the presence of levels of these defects was taken into account when investigation of the energy band diagram. It should be noted that, in all investigated MIM-structures, heavily-doped TiN were used as a substrates; therefore, when investigation of the energy band diagram, the value of the work function of Ti was used.

Table 4. Layer parameters of the structure Zr/YSZ/TiN used investigation of the energy band diagram.

Parameter	Value	Reference
Work function of Zr	4.05 eV	[79]
Electron affinity of YSZ	2.65 eV	[80]
Band gap of YSZ	5.5 eV	[72]
Level of α-band below the conduction band of YSZ	1.5 eV	[72]
Level of T-defect below the conduction band of YSZ	3.3 eV	[72]
Level of C-defect below the conduction band of YSZ	2.6 eV	[72]
Work function of Ti	4.2 eV	[81]

The obtained energy band diagram allows concluding the following. The Fermi level of Zr was 1.4 eV below the conduction band of YSZ (E_c), i.e., it approximately

coincided with the position of the α-band, located 1.5 eV below E_c. Thus, in the case of electronic conduction caused by the transfer of electrons in the α-band, it was found that there was no barrier for such transfer.

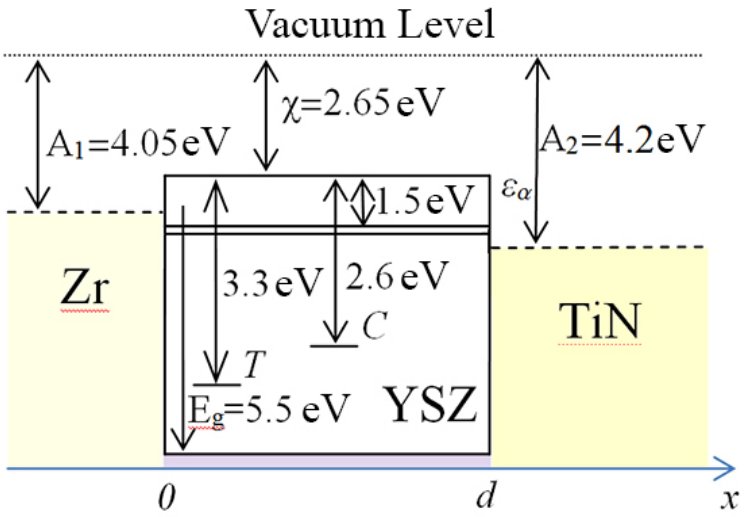

Figure 13. The energy band diagram of the structure Zr/YSZ/TiN

This meant that the Schottky mechanism could not be considered in this case as an electronic current mechanism. At the same time, the Poole-Frenkel mechanism (at which the *I–V* curve is linear in the same coordinates as in the case of Schottky emission) corresponded to electron transfer from the level of C-defects to the α -band with an activation energy of ~ 1 eV. This mechanism of electronic conduction in thermochemically reduced YSZ single crystals was considered in [72].

Thus, the investigations of the electrical properties of the initial memristive MIM-structures based on YSZ presented in this section made it possible to determine the values of the dielectric constant of YSZ, dielectric loss tangent, and resistance. This section presents the results of the investigation of the *I–V* curves and the energy band diagram of MIM-structures based on YSZ. The possibility of participation in the current transfer process of several mechanisms is shown.

3.2.2. Ion migration polarization in the yttria-stabilized zirconia films

In this section, in order to understand the mechanisms of resistive switching, the ion transfer parameters in YSZ were determined. The results of the study of the initial memristive MIM-structures based on YSZ by investigations of the ion migration polarization are presented.

Figure 14 shows the dynamic *I–V* curves of the initial MIM-structures based on YSZ, measured at various temperatures. The dynamic *I–V* curves did not depend on the polarity of the bias voltage. The direction of the hysteresis loop was always the same (as shown in Figure 14).

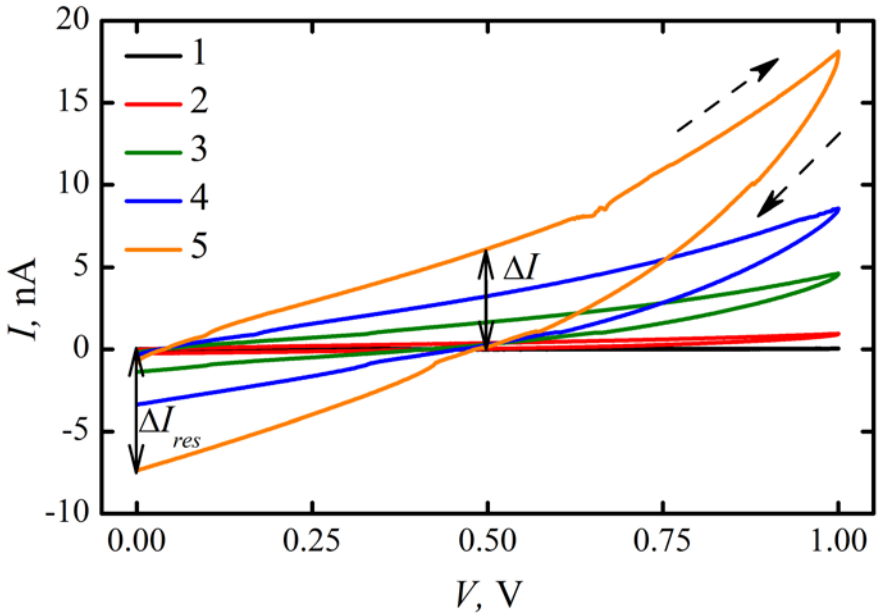

Figure 14. Dynamic *I–V* curves of the initial MIM-structures based on YSZ, measured at various temperatures *T*, K: 345 (1), 405 (2), 445 (3), 473 (4), 502 (5). Voltage sweep rate 0.02 V/s. Dashed arrows shows the direction of the voltage sweep [A3, A13]

The hysteresis observed in the dynamic *I–V* curves could be attributed either to the ion migration polarization of the insulator or to a trap one. It should be noted that there is a residual current ΔI_{res} at $V = 0$, which indicates the presence of the electret effect [75]. The magnitude of the hysteresis of the dynamic *I–V* curves and the

electret effect increased with increasing temperature especially abruptly when the threshold temperatures were reached, at which ionic hysteresis appeared in the MIS-structures. Therefore, the hysteresis observed in the dynamic *I*–*V* curves can be related to the inertia of the oxygen ion drift when increasing and decreasing the bias voltage. The movement of ions was accompanied by the appearance of transient electric currents in the external electric circuit, since it changed the electric field strength in the YSZ films. The hysteresis loop related to the ion migration polarization in the higher temperature range did not depend on the voltage sweep rate β. So far, one can exclude the effect of the displacement current. The charging and discharging of the MIM-capacitors cannot take effect as well since typical time constant of the current relaxation was < 1 μs as determined from the measurements of the small-signal parameters of the equivalent scheme.

In [82], another nature of the effect of non-zero-crossing *I*–*V* hysteresis curve was considered: internal electromotive force (V_{emf}) or nanobattery. V_{emf} results from the appearance of an internal ion current not equal to zero at $V = 0$ due to the spatial separation of positive and negative ions (respectively, Ag^+ and OH^- in case of SiO_2). The difference from the pure electret effect presented in this section, in the structures considered in [82], there is an electrochemical reaction on the electrodes, namely the electrochemical oxidation of Ag: $Ag \rightarrow e^- + Ag^+$. In this section, the applied voltage is below the threshold for electrochemical oxidation on the electrodes.

Since the magnitude of the hysteresis loop did not depend on the sign of the bias voltage at given measurement temperature, one can conclude the charges of the ions and traps in the investigated samples to be distributed uniformly within the YSZ film before the polarization [75]. The net charge ΔQ can be determined from the area of the hysteresis loop using the following relation [83]:

$$\Delta Q = \int_0^V \frac{IdV}{\beta} - \int_V^0 \frac{IdV}{\beta} \qquad (2)$$

Figure 15 shows the temperature dependences of the net charge ΔQ, of the forward current at zero reverse one ΔI (see Figure 14 for explanation), of the residual current ΔI_{res}, of the depolarization current I_{dep} and of the quasi-static capacitance C, obtained for MIM-structures based on YSZ. These temperature dependencies can be approximated by the combinations of two straight lines in the Arrhenius axes with the activation energies ~ 0.55 eV (at T > 380 K) and ~ 0.2 eV (at T < 380 K). The former activation energy can be related to the activation of the ion transport. The latter activation process can be related to the traps in YSZ.

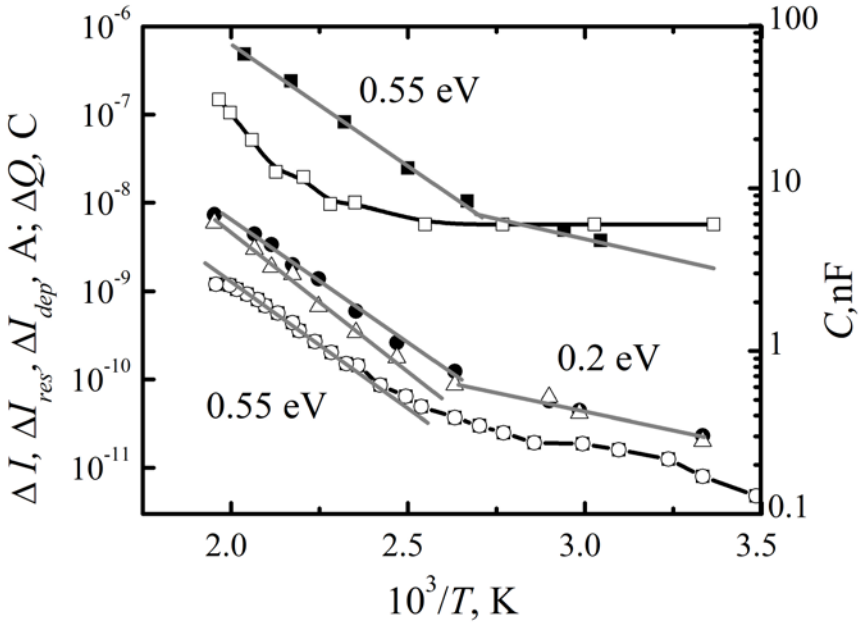

Figure 15. Temperature dependences of ΔQ (■), ΔI (●), ΔI_{res} (Δ), I_{dep} (○) and of C (□), obtained for MIM-structures based on YSZ [A3]

Assuming the uniform distribution of the charge in the YSZ films before the polarization, the surface density of the charge N was estimated according to the equation:

$$N = \frac{\Delta Q}{qS} \tag{3}$$

The values of the reduced surface concentration of the mobile ions in the YSZ films were not saturated with increasing temperature and can be estimated as $\approx 5 \cdot 10^{14}$ cm^{-2} at 505 K. Correspondingly, the reduced surface density of the traps in the films of ≈ 40 nm in thickness was estimated to be $\approx 1.2 \cdot 10^{12}$ cm^{-2}. Note that the volume concentration of the oxygen vacancies in the single crystal YSZ with 12 % mol. of Y_2O_3 is ~ 10^{21} cm^{-3} which corresponds to the surface vacancy concentration of ~ 10^{14} cm^{-2}. This meant that the oxygen vacancies in the investigated YSZ films were concentrated in a layer at least 5 times thinner than the YSZ film itself.

Also, the temperature dependencies of the quasi-static capacitance *C* are presented in Figure 15. These data support the estimates of the activation energies given above. Starting from $T \approx 380$ K corresponding to the beginning of manifestation of the ion migration polarization, the values of *C* began to increase with increasing temperature. At higher temperatures, this growth obeyed Arrhenius law with the activation energies ranging from 0.50 to 0.53 eV. These values were close to the ones for the ion migration obtained from the measurement of the dynamic *I–V* curves.

Typical kinetics of the temperature *T* and of the depolarization current I_{dep} after the polarization of the investigated structures are presented in Figure 16. The sample was polarized at 510 K and constant $V = 1$ V and was cooled down to 300 K rapidly. Then the sample was heated up again at $V = 0$. The maximum absolute value of I_{dep} took place near 500 K (Figure 16, curve 2). Analysis of the depolarization curve showed that the temperature dependence of I_{dep} to obeyed Arrhenius law when increasing *T*. The activation energy was ≈ 0.55 eV. This value was close to the ones obtained from the measurements of the dynamic *I–V* curves and of the quasi-static capacitance.

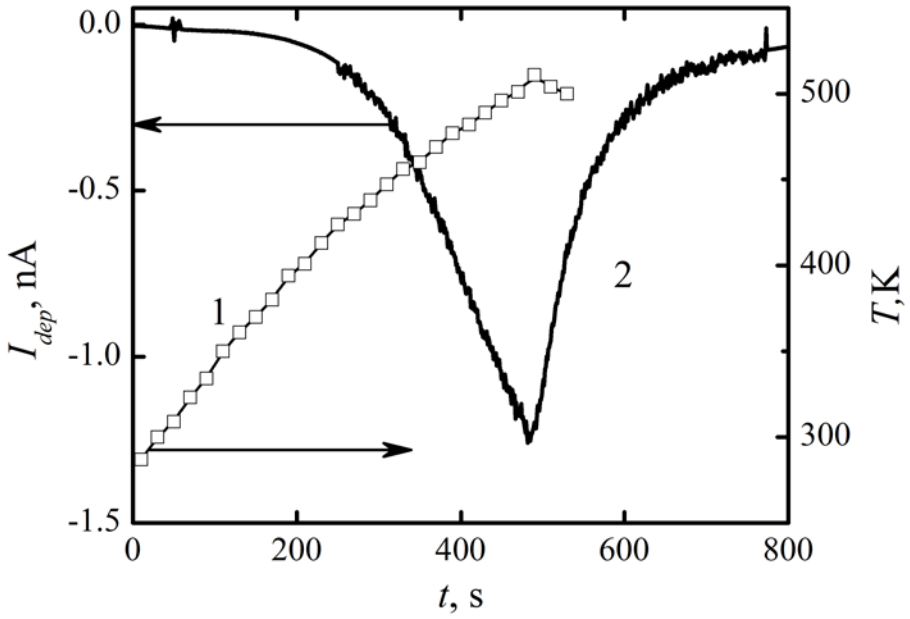

Figure 16. Kinetics of T and I_{dep}, obtained for MIM-structures based on YSZ [A3]

One can determine the charge of the polarizing ions from the area under the depolarization curve:

$$\Delta Q = \int_0^t I dt \tag{4}$$

The resulting values almost match the ones determined from the dynamic *I–V* curves.

The activation energy of the ion conductivity for the oxygen vacancies in single crystal zirconia stabilized in the cubic phase is known to fall into the range 1.0 – 1.2 eV [58, 84]. As it has been shown in [58], this activation energy consists of two nearly equal components: the energy of detachment of the ion from the lattice and the energy of its further motion over the potential barriers as it takes place in the classic mechanism of the ion migration polarization. In our case, the lower value of the activation energy probably is related to the polycrystalline (nanocrystalline) structure of the investigated YSZ films so that the oxygen ions can move along the grain boundaries [85], which were shown in Figure 6. The theory of

the ion transport along the grain boundaries is absent to date. Probably, the activation energy of the ion transport along the grain boundaries is less than the one for the ion transport in single crystals [85]. The parameters of the oxygen ion transport in the YSZ films determined by various methods are summarized in Table 5.

Table 5. The parameters of the oxygen ion transport in the YSZ films determined by various methods [A3, A10].

Measuring method	E_a, eV	N_I, cm^{-3} (500 K)
Dynamic *I-V* curves	0.55	$2.7 \cdot 10^{19}$
Thermal depolarization	0.55	$2.6 \cdot 10^{19}$
Quasi-static capacitance	0.50 – 0.53	–

The parameters of the oxygen ion transport in the YSZ films determined by various methods were consistent with each other.

Thus, using a set of low-temperature (T < 500 K) small-signal methods for investigations of the ion migration polarization in memristive MIM-structures based on YSZ, the value of one of the fundamental parameters of ion transport in nanocrystalline YSZ films was obtained – activation energy of migration of oxygen ions (0.50 – 0.55 eV), which is important for understanding the mechanisms of restoration/rupture of filaments during electroforming and resistive switching. The obtained value is ~ 2 times less than the values given in the literature for a bulk single-crystal YSZ in the temperature range 400 – 900 °C, which is associated with the predominant migration of oxygen ions along grain boundaries in nanocrystalline films.

3.3. Influence of Au nanoparticles in yttria-stabilized zirconia on the electrical properties of memristive MIM-structures

This section presents the results of investigations of capacitance-voltage characteristics (*C–V* curves) and conductance-voltage characteristics (*G–V* curves) of memristive MIM-structures based on YSZ, nanostructured by an array of Au NPs. Local charge accumulation in YSZ films with Au NPs was investigated by Kelvin Probe Force Microscopy (KPFM).

The preparation of the investigated structures is described in Chapter 2. The area of the structures was $S = 1.2 \cdot 10^{-3}$ cm^2. MIM-structures without an Au NPs were used as control structures. Investigations of structural properties are given in Section 3.1.

The presence of Au NPs resulted in nonlinear behavior of the structures, which was studied by measuring the admittance. Figure 17 shows *C–V* and *G–V* curves obtained at different temperatures and a frequency of 1 kHz.

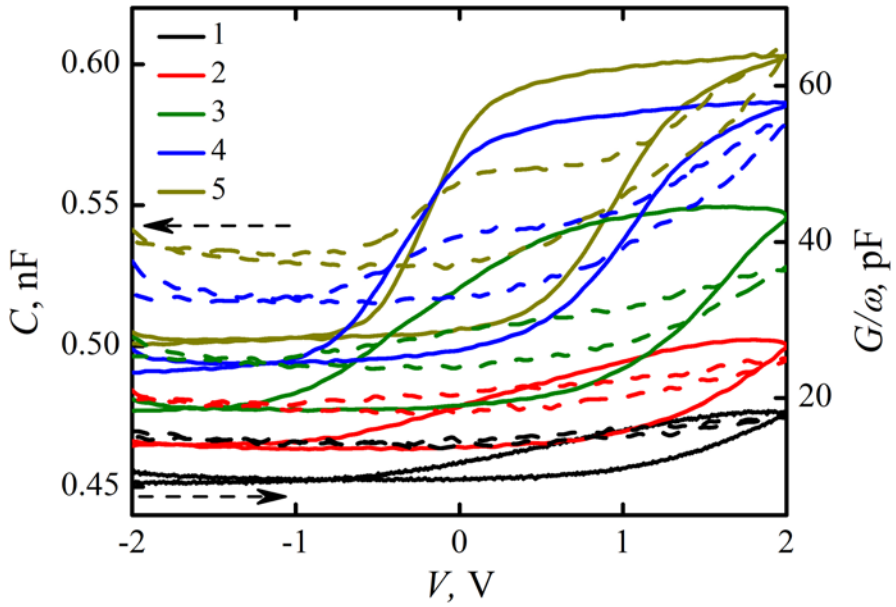

Figure 17. *C–V* (solid line) and *G–V* (dashed line) curves obtained for MIM-structure based on YSZ with Au NPs at a frequency of 1 kHz and at a temperature T, K: 380 (1), 422 (2), 455 (3), 482 (4), 502 (5). Dashed arrows shows the direction of the voltage sweep [A2]

Note that the capacitance and conductivity of the control structure (without an Au NPs) was independent of voltage. The dependencies shown in Figure 17 are typical for devices with nonlinear capacitance. The hysteresis of *C–V* curves increased with increasing temperature and behaved anomalously: the applied positive voltage shifted *C–V* curves to lower voltages. Since charging occurred only when the top electrode is under a positive voltage, this behavior of the dependences can be explained by charging the traps (generated as a result of presence of Au NPs) by electrons arriving from TiN. This could be due to the transfer of oxygen from YSZ to Zr during annealing, which, in turn, led to the appearance of a barrier at the Zr/YSZ interface, which made the transfer of electrons from the top electrode to the YSZ more difficult. Indeed, if the traps captured ions instead of electrons, the increase in the capacitance and conductivity with increasing temperature would be observed at both polarities of control voltage.

Increase in capacitance and conductivity with increasing temperature may be due to activation capture of electrons by traps, which is accompanied by overcoming the Coulomb barrier. Since $C \gg G/\omega$, the trap concentration can be estimated through the hysteresis area of the *C–V* curves. At high temperatures (480 – 502 K), the trap concentration reached saturation ($\sim 10^{12}$ cm^{-2}). This value was close to the surface densities of both Au NPs and grain boundaries. However, in the control samples and samples with NPs, the crystallites almost did not differ; therefore, the traps was associated with the presence of Au NPs in the YSZ (either with the NPs themselves or with centers located near them).

To estimate other parameters of electron traps, the temperature and frequency dependences of the difference $\Delta C = C(2\text{ V}) - C(-2\text{ V})$ between the capacitance values in the presence and in the absence of the electron capture by traps (at voltages of 2 and -2 V, respectively (Figure 18)) was analyzed. Such dependencies for the difference $\Delta G/\omega$ was also analyzed (Figure 18).

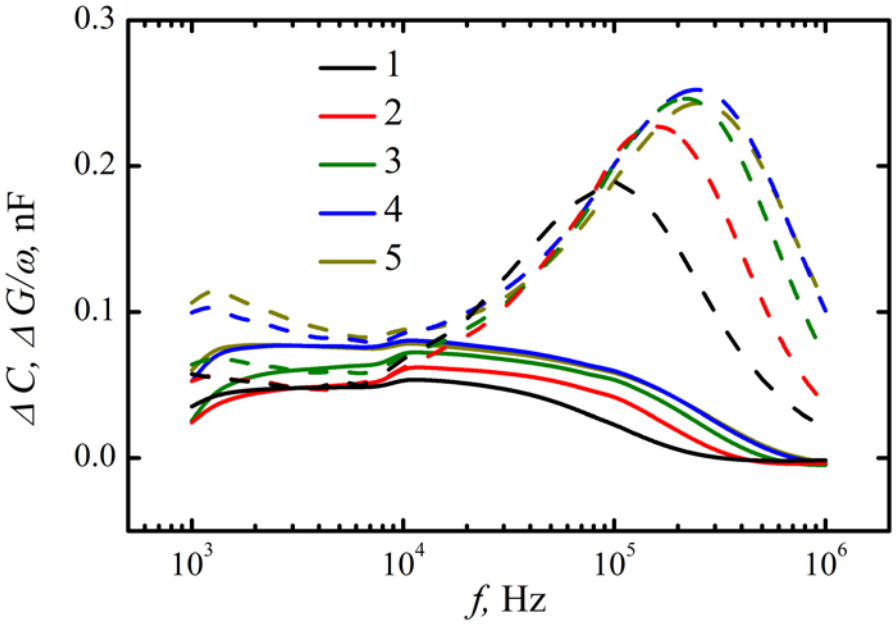

Figure 18. Frequency dependences of Δ*C* (solid line) and Δ*G*/*ω* (dashed line) obtained for MIM-structure based on YSZ with Au NPs at temperatures *T*, K: 380 (1), 422 (2), 455 (3), 485 (4), 502 (5) [A2]

The regions of frequency dispersion are clearly visible, which had a step (for Δ*C*) or a peak (for Δ*G*/*ω*) (Figure 18); the peak frequency coincided with the frequency of the corresponding step inflection. This shape of the dependences is characteristic of both polarization occurrence in an insulator [75] and capture by traps in a semiconductor [86]. The frequency dispersion regions shifted to higher frequencies with increasing temperature, which indicates the activation nature of the process. The control samples (without Au NPs) did not show a significant frequency dispersion of *C* and *G*/*ω* in the investigated frequency range. In this context, the dependencies shown in Figure 18 can be explained by the influence of traps caused by the presence of Au NPs.

The injection of electrons into NPs led to a change in the potential of the NP layer relative to the electrodes of the memristive structure by an amount (Figure 19)

$$\Delta\varphi = \frac{eN_s Nd}{\varepsilon\varepsilon_0}\left(1-\frac{d}{d_0}\right), \qquad (5)$$

where e is the elementary charge, N_s is the surface density of NPs, N is the average count of excess electrons in NPs, d_0 is the insulator thickness, d is the distance between an electrode, to which a negative voltage was applied, and a layer of NPs, ε is the dielectric constant.

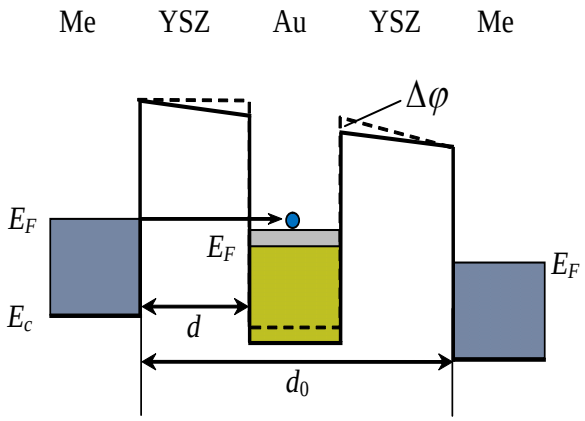

Figure 19. The energy band diagram of the memristive MIM-structure based on based on YSZ films, nanostructured by an array of Au NPs

Accordingly, the electric field strength in the gap between a layer of NPs and the electrode, to which a negative voltage was applied, decreased by $\Delta\varphi/d$, and, on the other hand, increased by $\Delta\varphi/(d_0 - d)$, which was an important factor in the processes electroforming and resistive switching.

The possibility of charge accumulation in Au NPs has been demonstrated experimentally in structures YSZ (8 nm)/Au (1 nm)/YSZ (2 nm)/n^+-Si by KPFM. Thin (10 nm thick) films without Au NPs were prepared as control samples. Figure 20a shows the KPFM image of the surface of the investigated structure after the point injection of electrons from the substrate to Au NPs at V = 3 V. The KPFM image after injection showed a feature due to the electrostatic interaction of the AFM-probe with electrons localized in Au NPs (the charge spot). Figures 20b – 20f show the KPFM images of the charge spot on the surface of the YSZ film with Au NPs, obtained at equal time intervals (1 day) after the charge was injected. Figure 21

shows the profiles of the surface potential $\Delta\Phi(x)$, where x is the coordinate in the surface plane over the charge-spot diameter. The decrease in the maxima of the profiles $\Delta\Phi_m$ with time is due to electrons leaving Au NPs and going to the n^+-Si substrate by tunneling via defects in the YSZ layer, presumably, via oxygen vacancies. Figure 22 illustrates the $\Delta\Phi_m$ parameter as a function of the time elapsed after charge injection for the series of profiles $\Delta\Phi(x)$ shown in Figure 21. As seen in Figure 22, the value of $\Delta\Phi_m$ decreased exponentially with time, and the retention time τ of the charge for that series of measurements was ~3 days.

Note that the width of the charge-spot potential profile $\Delta\Phi(x)$ (at half-maximum) was almost independent of time; i.e., there was almost no lateral charge spreading within the nanoparticle layer.

Note that in [A5, A15] the results of injection of electrons in the form of a line into such samples are presented. Analysis of the results showed that the retention time of the charge was ~ 1 hour.

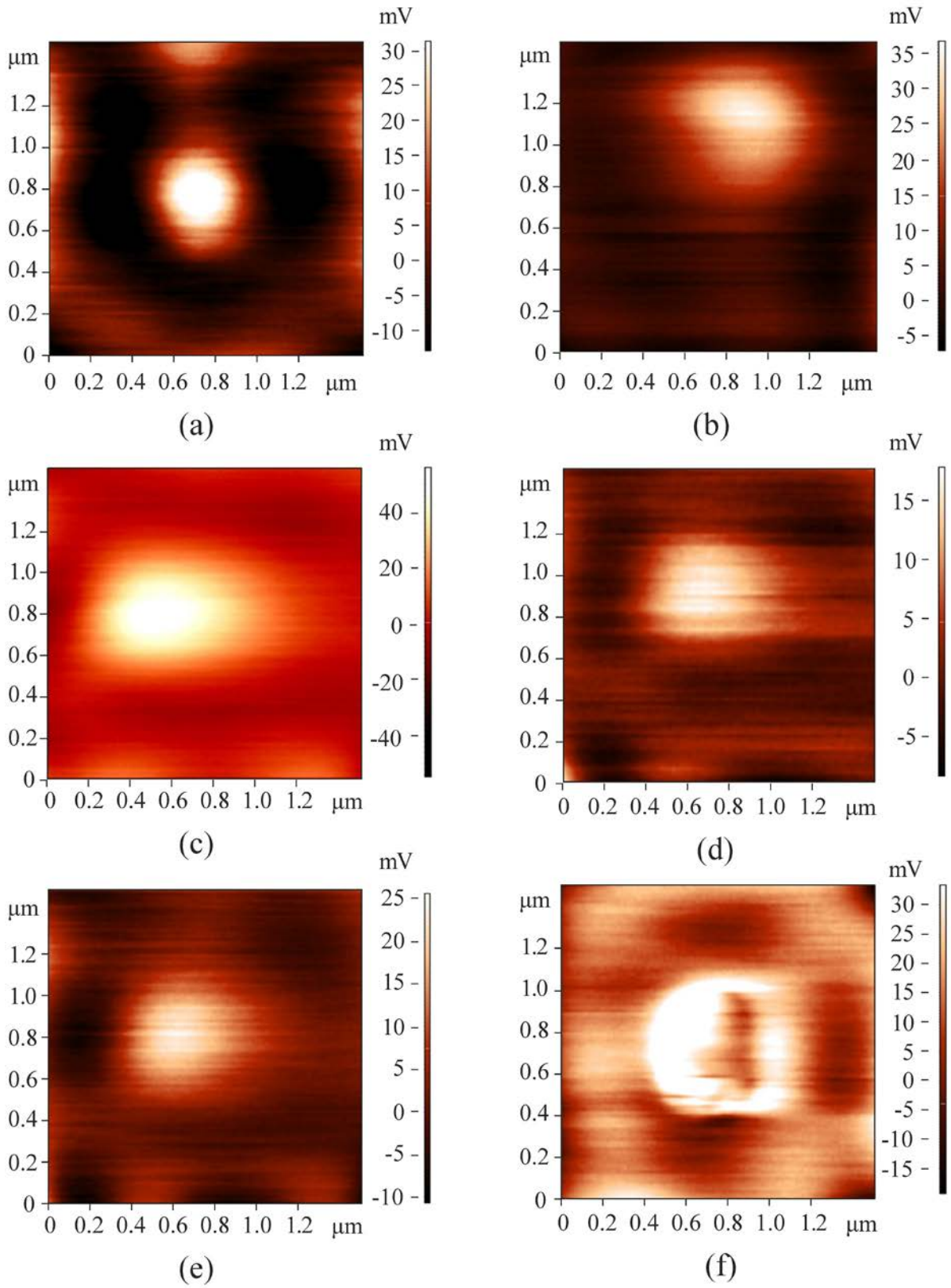

Figure 20. KPFM images of a charge spot on the surface of a YSZ film with Au NPs, obtained at various moments of time after the charge was injected *t*, days: 0 (a), 1 (b), 2 (c), 3 (d), 4 (e), and 5 (f) [A4, A14]

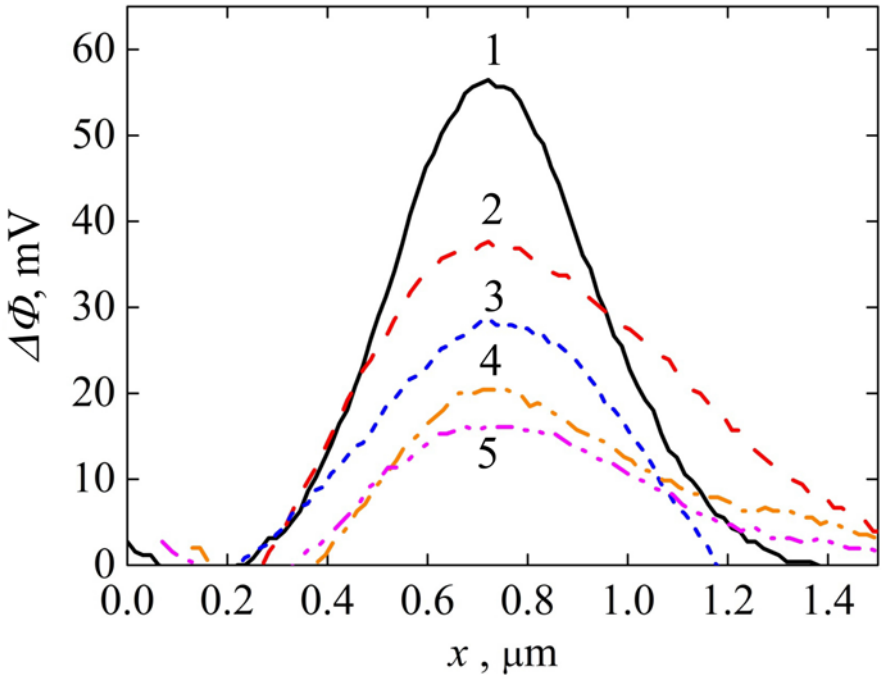

Figure 21. Profiles of the potential $\Delta\Phi$ induced by a charge injected into Au NPs in a YSZ film at various moments of time after the charge was injected *t*, days: 0 (1),1 (2), 2 (3), 3 (4), 4 (5) [A4, A14]

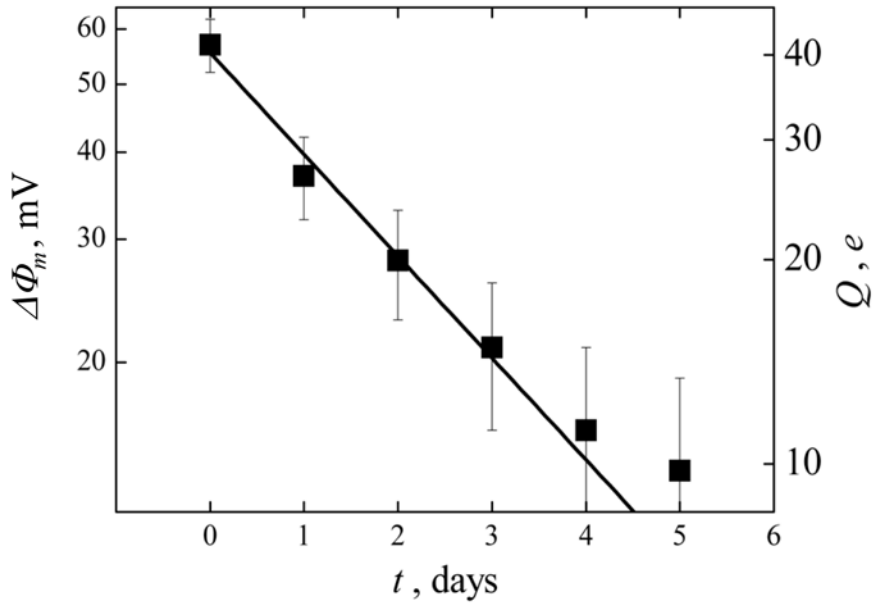

Figure 22. Maximum values of the potential $\Delta\Phi_m$ induced by the charge of electrons localized in Au NPs in the YSZ film and of the charge *Q* as functions of time t elapsed after the charge was injected [A4, A14]

Thus, nonlinearity and hysteresis of *C–V* and *G–V* curves of memristive MIM-structures based on YSZ, nanostructured by an array of Au NPs, were found. The effect was associated with the accumulation of charge in the NPs. The possibility of charge accumulation in Au NPs has been experimentally confirmed by an independent method of KPFM. This effect can be used to create memristors with nonlinear capacitance. In particular, on the basis of such elements, it is possible to create devices of combined resistive-charge memory.

3.4. Electrical properties of memristive MIS-structures based on yttria-stabilized zirconia

The investigation of resistive switching in MIS-structures is associated with two fundamental circumstances. Firstly, the opportunity to obtain more detailed information about the phenomena, occurring in the insulator, at the insulator/semiconductor interface and in the semiconductor during electroforming and resistive switching. Secondly, memristive MIS-structures have a higher functionality. This is due to the fact that the electroforming and resistive switching occurring in the MIS-structure can be controlled by the processes occurring in the semiconductor, which have been studied most widely. It should be noted that in such structures, the voltage is redistributed between the insulator and the semiconductor, which, in turn, complicates the observation of resistive phenomena.

This section discusses the electrical properties of the initial MIS-structures based on YSZ. It should be noted that the density of surface states, most likely, should have a large effect on the properties of the structure. Therefore, two variants of structures with different density of surface states were prepared and investigated. In order to decrease the density of surface states, nanometer layers of antimony were deposited (see Chapter 2).

Figure 23 shows the *C–V* and *G–V* curves of the MIS-structure Au/Zr/YSZ/SiO_2/*n*-Si ($S \sim 1 \cdot 10^{-2}$ cm^2) measured at different temperatures.

An anomalous hysteresis (Figure 23, curves 2 and 3) was observed in the *C–V* and *G–V* curves at $T > 300$ K. This kind of hysteresis can be attributed to the ion migration in YSZ [87], whereas the normal hysteresis (Figure 23, curve 1) typical for the *C–V* and *G–V* curves of the MIS-structures originates from the exchange by electrons or holes between the semiconductor substrate and the surface states at the semiconductor/insulator interface.

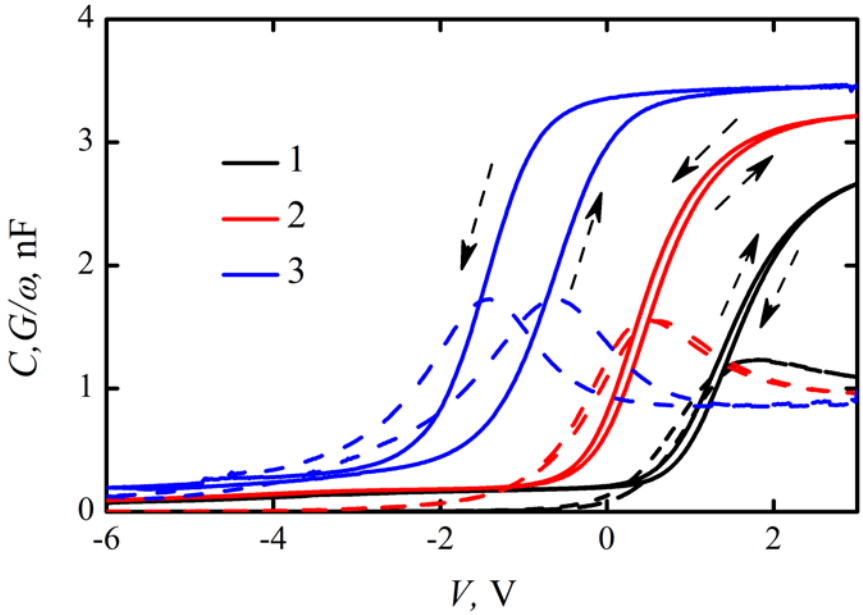

Figure 23. *C–V* (solid line) and *G–V* (dashed line) curves of MIS-structures Au/Zr/YSZ/SiO_2/*n*-Si, obtained at a frequency of 100 kHz and at a temperature *T*, K: 323 (1), 414 (2), 500 (3). Dashed arrows shows the direction of the voltage sweep [A3]

The values of area within the hysteresis loops increased with increasing temperature in the temperature range 350 – 400 K. At higher temperatures, the hysteresis loop width tended to saturate and even decreased with increasing temperature. The values of the surface state density were obtained from the frequency and temperature dependencies of the admittance [86] of the MIS-structures using the model of single level surface states. The ionization energy 0.47 eV and the density of the surface states $4.7 \cdot 10^{11}$ cm^{-2} were found. The specific density of the surface states at

$V = V_{FB}$ (V_{FB} is the flat band voltage) was estimated using the differential method [86] to be < $5 \cdot 10^{11}$ cm^{-2} eV^{-1}.

Temperature dependencies of the flat band voltage shift ΔV_{FB} and the ones of the reduced mobile ion density N_I are shown in Figure 24.

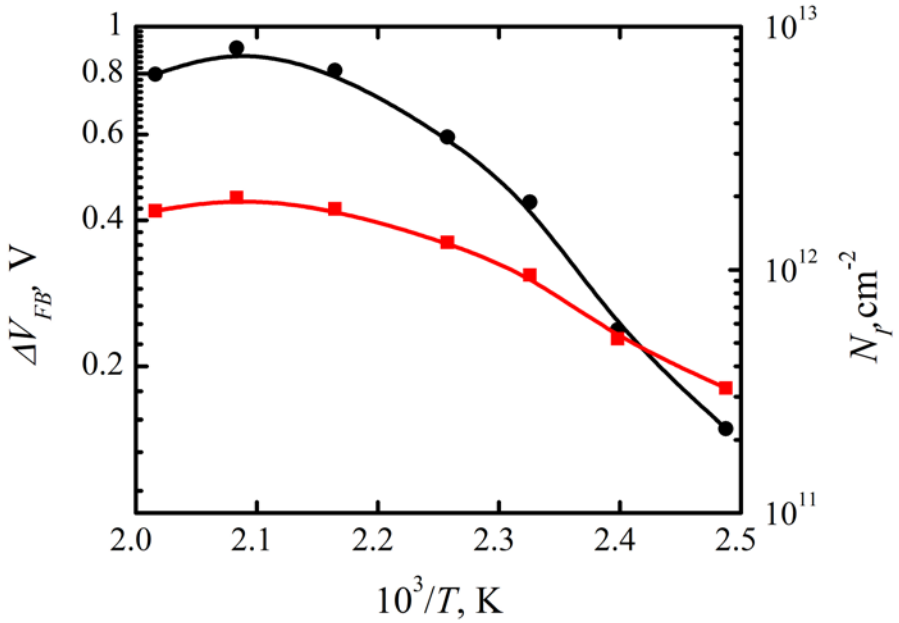

Figure 24. Temperature dependencies of ΔV_{FB} (●) and N_I (■) [A3]

The temperature dependence of ΔV_{FB} obeyed Arrhenius law with the activation energy ~ 0.5 eV. At higher temperatures, the saturation and even some decay of ΔV_{FB} with increasing temperature was observed. Within this temperature interval, the highest concentration of the mobile ions responsible for the anomalous hysteresis was reached. The reduced surface density of the mobile ions was estimated using the following equation [86]:

$$N_s = C_D \cdot \Delta V_{FB} / qS \,, \qquad (6)$$

where C_D is the capacitance of the insulator determined from the saturated capacitance in the C–V curves (Figure 23) and q is the elementary charge. The value of N_s was ≈ $2 \cdot 10^{12}$ cm^{-2}. Assuming the mobile ions to be distributed uniformly inside

the YSZ film, the mobile ion concentration N_I can be estimated (~ $5 \cdot 10^{17}$ cm^{-3}). This value is an underestimate obviously since typical value of the oxygen vacancy concentration in single crystal YSZ is ~ 10^{21} cm^{-2} [84]. The obtained value is underestimated due to the fact that the anomalous and normal hysteresis was opposite in direction. In this case, an increase in temperature led to an increase in the density of surface states and, accordingly, an increase in normal hysteresis and a decrease in anomalous one.

Figure 25 shows the *C*–*V* and *G*–*V* curves of MIS-structure Au/Zr/YSZ/Sb/SiO_2/*n*-Si (S ~ $1.2 \cdot 10^{-3}$ cm^2), measured at different frequencies.

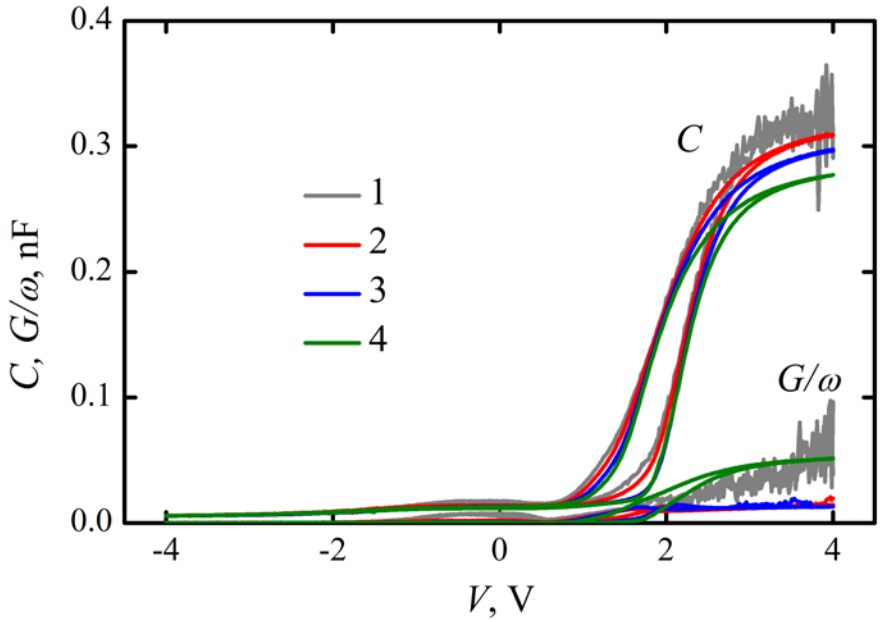

Figure 25. *C*–*V* and *G*–*V* curves of the investigated structure, measured at a frequency *f*, kHz: 1 (1), 10 (2), 100 (3), 1000 (4). Dashed arrows shows the direction of the voltage sweep [A6]

These curves reveal (i) absent frequency dispersion of capacitance in the region of its maximum modulation and (ii) the absence of maxima in *G*/*ω* dependences. Both these facts are indicative of a low density of «fast» surface states (manifested in the 1 – 1000 kHz range) on the insulator/semiconductor interface. Accordingly, the time for the transition of an electron from the bulk to such surface states was 10^{-3} – 10^{-6} s.

The density of these states estimated in the framework of the phenomenological theory of G/ω [86] proved to be below 10^{10} cm^{-2} eV^{-1}.

Hysteresis of the *C–V* curves can be related to the capture of charge carriers on states in the insulator with large relaxation times. A shift relative to the zero voltage corresponds to the flat band voltage $V_{FB} \approx 2$ V and can be explained by the presence of a built-in charge in the insulator. The density of this charge corresponds to a surface concentration $3.1 \cdot 10^{12}$ cm^{-2}.

Thus, the electrical properties of MIS-structures have been studied. It was found that the presence of a passivating Sb layer between the YSZ and the semiconductor reduced the concentration of surface states to values < 10^{10} cm^{-2} eV^{-1}.

The activation energy of migration of oxygen ions in YSZ films (0.5 eV) in MIS-structures has been determined, which is in good agreement with the results obtained in MIM-structures. Also, it was found that the *C–V* measurements of the MIS-structures with relatively high density of the surface states at the YSZ/Si interface gave the underestimated values of the mobile oxygen ion concentration. The origin of the underestimate was related to the impact of the surface states at the YSZ/Si interface.

3.5. Main results of Chapter 3

It was found that YSZ films had a nanocrystalline structure and a well-developed interface with the top electrode.

It was found that nanoscale gold layers in a sandwich structure YSZ/Au/YSZ during annealing coagulated into two-dimensional arrays of NPs with a diameter 2.3 ± 0.4 nm, an average distance between NPs 3.7 ± 1.6 nm and surface density $(7.3 \pm 6.3) \cdot 10^{12}$ cm^{-2}.

Using a set of low-temperature (T < 500 K) small-signal methods for investigations of the ion migration polarization in memristive MIM- and MIS-structures based on YSZ, the value of one of the fundamental parameters of ion

transport in nanocrystalline YSZ films was obtained – activation energy of migration of oxygen ions (0.50 – 0.55 eV), which is important for understanding the mechanisms of restoration/rupture of filaments during electroforming and resistive switching.

Nonlinearity and hysteresis of *C–V* and *G–V* curves of memristive MIM-structures based on YSZ, nanostructured by an array of Au NPs, were found. The effect was associated with the accumulation of charge in the NPs. The possibility of charge accumulation in Au NPs has been experimentally confirmed by an independent method of KPFM. This effect can be used to create memristors with nonlinear capacitance. In particular, on the basis of such elements, it is possible to create devices of combined resistive-charge memory.

The electrical properties of MIS-structures have been studied. It was found that the presence of a passivating Sb layer between the YSZ and the semiconductor reduced the concentration of surface states to values $< 10^{10}$ cm^{-2} eV^{-1}.

CHAPTER 4. Electroforming and resistive switching of memristive MIM-structures based on yttria-stabilized zirconia

This chapter shows the results of investigations of processes of electroforming and resistive switching of metal-insulator-metal (MIM) structures based on yttria-stabilized zirconia (YSZ), the properties of which before electroforming were discussed in Chapter 3. Section 4.1 presents the results of investigations of the effect of current compliance on the process of electroforming and subsequent resistive switching, as well as, sustainability of the parameters of the resistive switching of memristive structures to low and high temperatures. In Section 4.2, using the method of small-signal measurement of admittance at zero bias voltage on the structure, the values of the dielectric constant of YSZ, dielectric loss tangent and resistances of structures after electroforming and resistive switching were determined. An interpretation of the obtained results is given. Section 4.3 discusses the properties of the developed memristive devices are presented. Section 4.4 summarizes the results obtained in Chapter 4.

4.1. Electroforming and resistive switching of memristive MIM-structures based on yttria-stabilized zirconia. Effect of current compliance

It is known from the literature data (given in Chapter 1) that the properties of MIM-structures, demonstrating resistive switching, significantly depend on the modes of electroforming. In particular, it is noted that the values of the current compliance can significantly affect the form of the current-voltage characteristics (*I–V* curves) and the parameters of resistive switching. Below, the effect of resistive switching of MIM-structures based on YSZ is considered separately for structures that have undergone electroforming at a high value of current compliance (Section 4.1.1) and a low value of current compliance (Section 4.1.2). It is shown that the observed resistive switching is bipolar and exhibits features that

can be associated with the space-charge-limited current (SCLC) mechanism. In Section 4.1.3, on the basis of the experimental data presented in Sections 4.1.1 and 4.1.2, it was concluded that bipolar resistive switching in the investigated structures can be caused by electrostatic/electronic effects, and experimental *I–V* curves, characterizing observed resistive switching, are approximated within the framework of a model that takes into account the effects of capture of conduction electrons by electron traps in the YSZ and the emission of electrons from these traps. The results of studying the effect of temperature on resistive switching of the investigated structures are presented in Section 4.1.4.

4.1.1. Characteristics of resistive switching of MIM-structures after electroforming at a high value of current compliance

During electroforming at high values of current compliance, a sufficiently high power in the region of filament formation is released. This leads to a significant increase in temperature, an increase in the diffusion mobility of oxygen ions (oxygen vacancies) and, as a result, the formation of a filament with a high current-carrying capability. Large currents accelerate both the transfer of ions inside of the filament and redox-reactions at the active electrode/insulator interface (interfaces) in the region of the filament (filaments), and, as a result, the resistive switching process itself [88].

This section presents the results of a study of the features of resistive switching of memristive MIM-structures based on YSZ after electroforming at a high value of current compliance.

Figure 3 shows a schematic representation of the investigated structure. Figure 26 shows measured at room temperature *I–V* curves, demonstrating electroforming and bipolar resistive switching from low resistance state (LRS) to high resistance state (HRS) (RESET process) and vice versa (SET process), of the investigated structure.

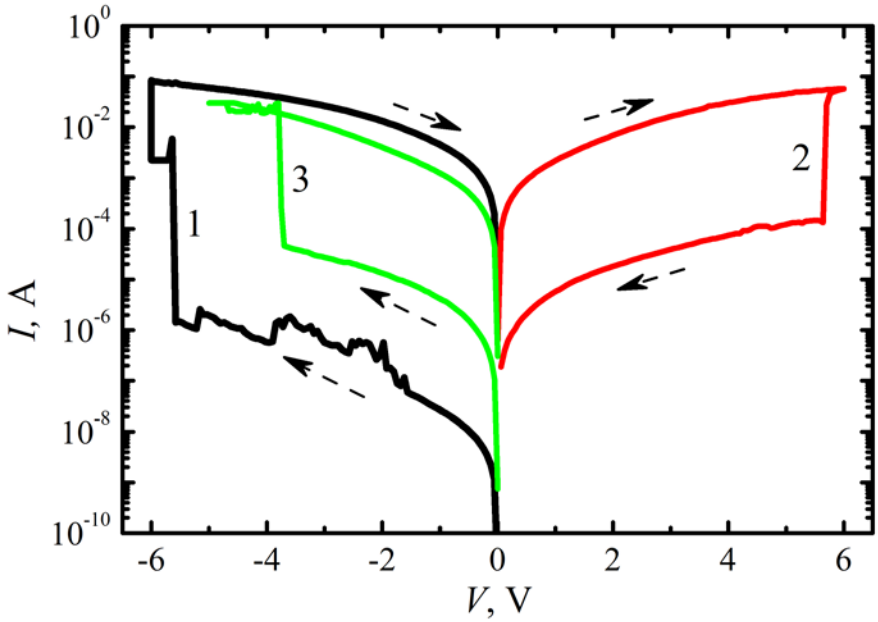

Figure 26. *I–V* curves of the memristive MIM-structure Au/Zr/YSZ/TiN/Ti/SiO_2/Si, demonstrating electroforming (1) and bipolar resistive switching from LRS to HRS (2) and from HRS to LRS (3). Dashed arrows shows the direction of the voltage sweep [A1]

Electroforming of the structures was carried out at a negative voltage in the range from 0 to -6 V. The value of current compliance for presented on Figure 26 *I–V* curves was 100 mA.

When a negative potential was applied to the top electrode, electrons were injected into the insulator. The densest electron current channels were formed in regions of electric field concentration (for example, at grain boundaries in polycrystalline films [73]). According to high-resolution Transmission Electron Microscopy (TEM) data, the Zr/YSZ had a well-developed interface (see Figures 6, 27), which is associated with the columnar structure of the polycrystalline YSZ film. Figure 27 shows the results of TEM investigations: distribution of the concentration of Zr, Y, and O in the structure Au/YSZ/TiN/Ti/SiO_2/Si before (a) and after electroforming (b). The profiles were measured at a depth of ~ 12 nm under the Au electrode.

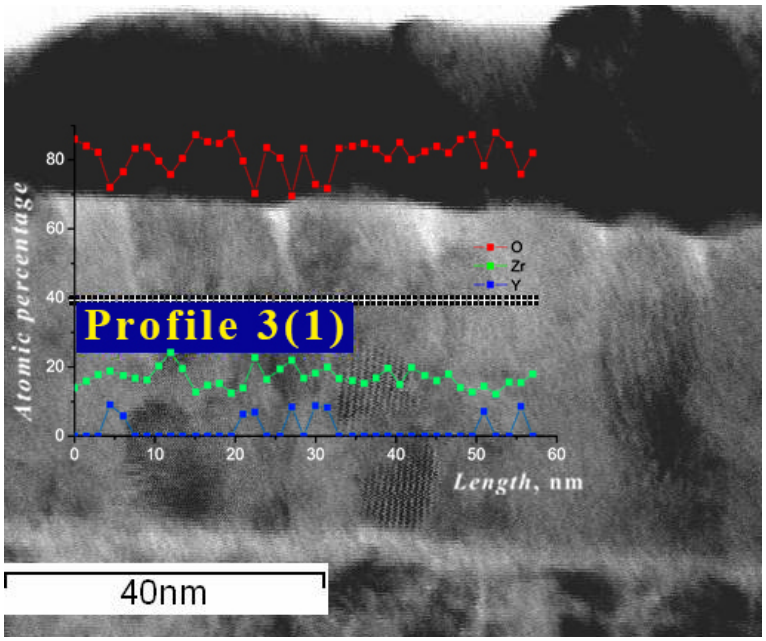

(a)

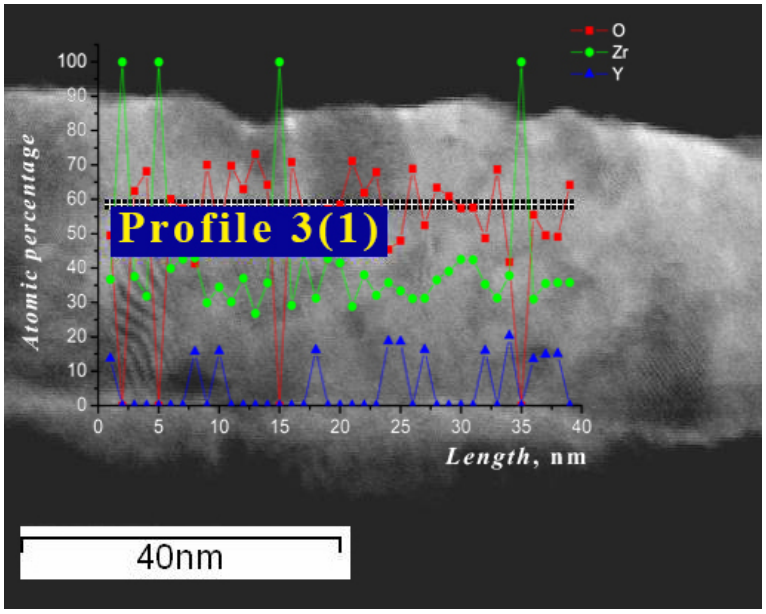

(b)

Figure 27. Distribution of the concentration of Zr, Y, and O in the structure Au/YSZ/TiN/Ti/SiO_2/Si before (a) and after electroforming (b) [A10]

Before electroforming, the distribution of the concentration of elements was uniform within the experimental error. After electroforming, a significant redistribution of the concentration of zirconium and oxygen was observed (an increase in Zr and a decrease in O). These redistributions (bursts of concentration) coincide with the position of grain boundaries in the YSZ. The obtained results

indicate that grain boundaries are the most probable regions in the structure of an YSZ film for the formation of metal bonds, accumulation of oxygen vacancies and, accordingly, filaments. It should be noted here that the filaments formed along the grain boundaries do not all simultaneously participate in a single resistive switching (this conclusion is confirmed by the absence, within the experimental error, of the dependence of the current value on the area of the top electrode, as will be shown below).

It is important to note that the work function of Au is 5.1 eV [79], Zr is 4.05 eV [79], and TiN (Ti) is 4.2 eV [81]. The presence of the Zr sublayer in the structure significantly reduced the work function of top electrode. Since the work function of Zr is less than the work function of TiN, then the injection of an electron from the top electrode into the insulator should be much more efficient than that from the bottom electrode at the same voltage. Therefore, in order to reduce the voltage of electroforming, it was carried out in the process of applying negative voltage. The regions of filament formation were heated as a result of reaching value of current > ~ 10^{-6} A (Figure 26) [89]. In this case, the diffusion mobility of oxygen ions and the rate of alignment of oxygen vacancies along the field in the region of increased electric field strength (grain boundaries) increased, and, filaments, consisting of oxygen vacancies, were formed from the top interface to the bottom one. Some of the oxygen ions could cross the boundary of the bottom interface and form the TiO_xN_y compound [see, for example, 90]. The priority of filament growth from the side of the top electrode is also indicated by the asymmetry of the *I–V* curves ($V_{SET} < V_{RESET}$).

As a result of electroforming, the structures were switched to the LRS. Subsequent application of positive voltage to the structures switched it from LRS to HRS (Figure 26, curve 2). Reverse switching – from HRS to LRS (Figure 26, curve 3), occurred with an increase in the value of the negative voltage.

It is believed that the formed filament is not completely destroyed during RESET (only in a layer of ~ several nm in the region of the top interface [89]). This

leads to the fact that the remaining part of the filament is less exposed to the electric field. This part serves as a nucleus for the restoration of the filament during subsequent switching of the structure. In addition, such a conducting nucleus acts as a concentrator of the electric field, which should lead to a more efficient restoration of the filament and provide a smaller spread of the parameters of the resistive switching of the memristor during subsequent switching and the stability of the device over time. It should be noted that in the process of resistive switching under «hard» conditions (long switching pulse duration, high electric field strength), the structure of the filament can change many times, which leads to fluctuations of the switching voltage and the resistance value in subsequent cycles [49].

In order to establish the mechanisms of conduction in LRS and HRS, *I–V* curves, shown in Figure 26, are presented in Figure 28 on a double logarithmic scale.

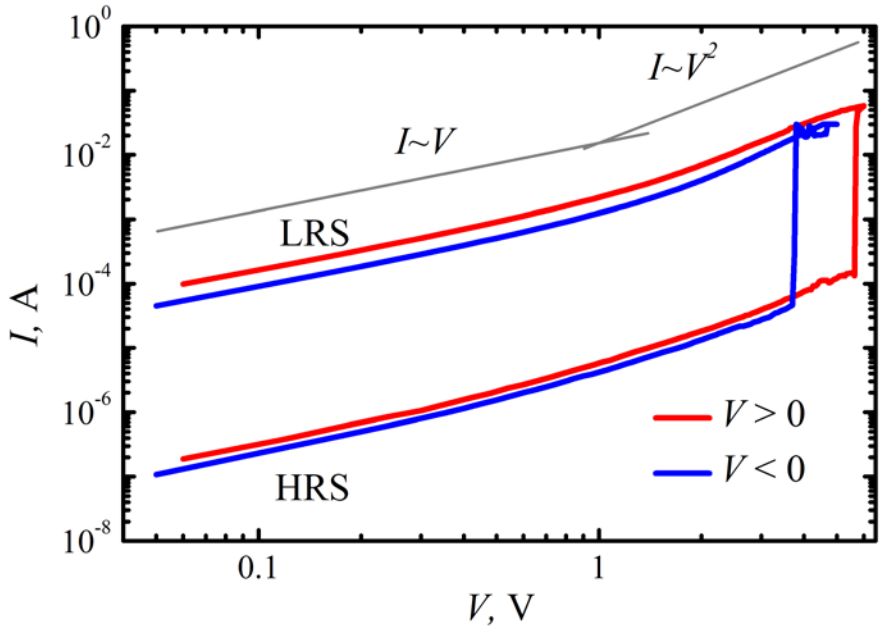

Figure 28. Dependence of the current in the LRS and HRS on the voltage on a double logarithmic scale. Black curves are lines approximating sections of the *I–V* curves with different slopes [A1]

These dependences demonstrate the values of the slope of the tangent: coinciding at $V < 0$ and $V > 0$ and equal to 1.0 in HRS and LRS in the low voltage region; equal to 1.9 in the HRS and 2.1 in the LRS in the high voltage region. The transition from the low voltage region to the high voltage region occurs almost at the same negative and positive voltage (~ 0.7 V in HRS and ~ 1.1 V in LRS). Thus, both at positive and negative voltages with an increase in voltage, these dependences initially have a behavior close to ohmic, and with a further increase in voltage, a dependence $I \sim V^n$ with n~2 is observed, which may be associated with the SCLC mechanism [77].

4.1.2 Characteristics of resistive switching of MIM-structures after electroforming at a low value of current compliance

Figure 29 shows several cycles of *I–V* curves of the memristive structure Au/Zr/YSZ/TiN/Ti/SiO_2/*n*-Si, measured at different values of current compliance. It is seen that at current compliance equal 30 mA, the structures demonstrated a relatively abrupt switching from LRS to HRS. At the same time, as value of current compliance decrease, the gradual behavior of switching from LRS to HRS began to dominate. The observed effect was interpreted within the framework of the filamentary model. In the case of a low value of current compliance, the temperature inside the filament during electroforming is relatively low. Therefore, a «loose» filament with a small cross section and low current-carrying capability (lower current in LRS, higher resistance), than in the case of high value of current compliance, is formed [88, 91]. The count of vacancy chains inside of filament, involved in the current transfer, is limited and decreases with decreasing of value of current compliance, which, in turn, leads to a decrease in currents in the LRS and instability of the resistive switching parameters (Figure 29d). The non-monotonicity of this transition is due to the statistical nature of the processes of rupture and restoration of a small count of conducting channels (atomic chains) inside of filament (filaments).

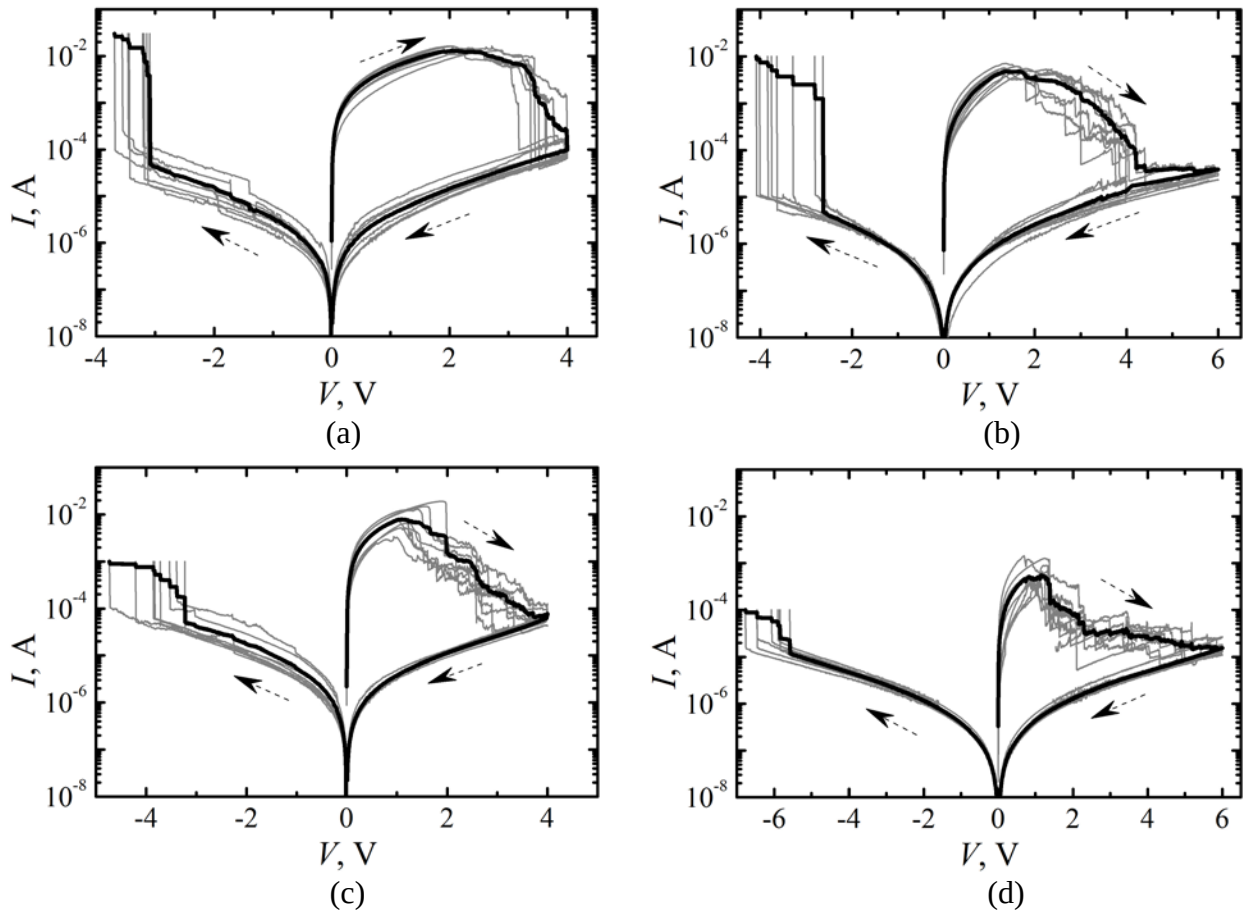

Figure 29. *I–V* curves of the memristive structure Au/Zr/YSZ/TiN/Ti/SiO_2/*n*-Si, obtained at different values of current compliance: 30 mA (a), 10 mA (b), 1 mA (c) and 100 μA (d). Dashed arrows shows the direction of the voltage sweep

It should be noted that the I_{RESET} exceeded the value of current compliance only in the case of 1 mA and 100 μA. This is most likely due to the fact that in this experiment the flowing current was limited by the measurement instrument. Due to the low response speed of the measurement instrument (in relation to the high switching speed in the RRAM), instrument compliance is unable to effectively limit current through RRAM devices during resistive switching [92]. It should be noted here that the given data indicate the possibility of controlling the I_{RESET} value using current compliance, which can be applied in multi-level cells and neuromorphic devices.

A decrease in the value of the currents flowing through the structure (that is, a decrease in the value of the current compliance) leads to an increase in the lifetime of

the device (endurance) both in the case of single cell and in the case of array structure.

Two possible mechanisms of failure of the memristive structure Au/Zr/YSZ/TiN were observed experimentally: oxygen escape through the top electrode at $V > 0$, followed by detachment not only of the top electrode, but also of the oxide layer (as in [93]), as well as the gradual loss of oxygen due to continuous oxygen-scavenging effect of the TiN bottom electrode over time (as in [94]).

It is important to note that the process of single resistive switching is most likely controlled by one filament (a limited count of oxygen vacancy chains). The obtained experimental data about influence of the top electrode area on the value of the current through the memristive structure in the LRS showed the independence of currents on the top electrode area within the experimental error (Figure 30). During switching of the memristive structure to HRS, there was rupture (oxidation) of filament in the region of the interface with the electrode. Subsequent switching to LRS was accompanied by the restoration of the filament, however, its structure and interface structure, as noted above, may have changed [89]. This basically determines the scatter of the memristor parameters from switching to switching.

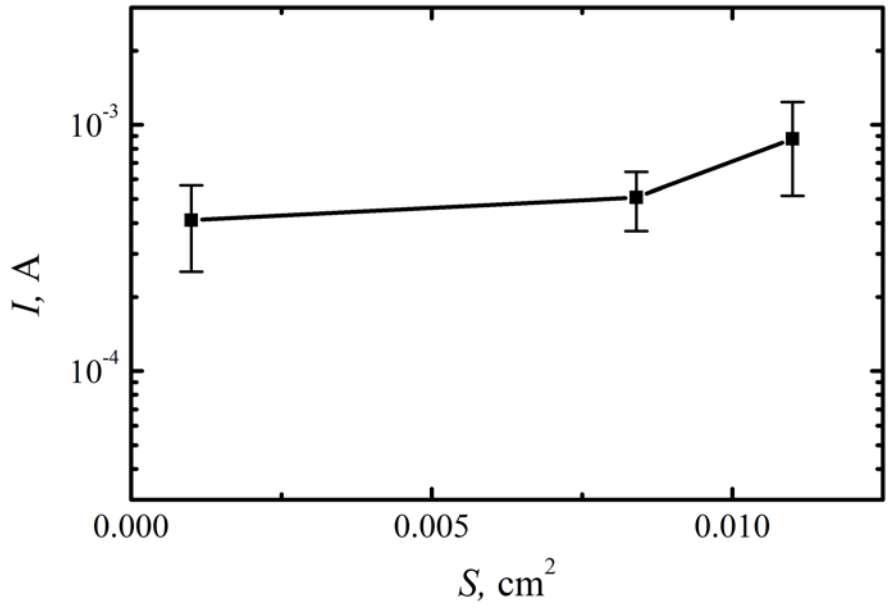

Figure 30. Dependence of the values of current in the LRS (at 0.5 V) on the top electrode area

4.1.3 Model of resistive switching of the investigated MIM-structures

In the previous sections, it was shown that the investigated Au/Zr/YSZ/TiN/Ti/SiO_2/Si structures exhibit ohmic conduction at low negative and positive voltages; however, as the voltage increases, the *I–V* curve has the form $I \sim V^n$ with n~2. These *I–V* curves indicate that the conduction mechanism in HRS and in LRS is due to SCLC mechanism [95]. Such bipolar resistive switching of MIM-structures, caused by electrostatic/electronic effects, in particular, the effects of the capture of conduction electrons by electron traps and electron emission from traps, was considered by the authors of [30, 96] (see also the bibliography given in these articles).

The SCLC mechanism was considered earlier, as a rule, in those cases when the flowing current was controlled by the bulk properties of the sample material [95]. Recently there has been an increase in interest in the consideration of cases where traps located near the metal/insulator interface appear in the SCLC mechanism. In accordance with this, some authors [30, 96] believe that the switching region, containing high concentration of electron traps and in which occurs rupture and restoration of filaments, is located in a thin nanometer insulator (oxide) layer adjacent to the top electrode. At the same time, in the region adjacent to the bottom electrode, the filaments do not undergo significant changes during resistive switching. Each such residual filament can be considered as an ohmic contact with the bottom electrode. In this case, the *I–V* curves, characterizing the resistive switching, have the same form as the *I–V* curves of our samples (see Figure 28) and can be interpreted within the framework of monopolar (electron) injection, which leads to SCLC mechanism.

In HRS, the traps in the insulator are not occupied by electrons, and the concentration of conducting electrons in it is low. When a negative voltage is applied to the structure, electrons are injected from the top electrode into the insulator. The injected electrons are captured by traps. When the traps are completely filled, their

influence on the current compliance disappears and, therefore, current abruptly increased as a result of the fact that additionally injected electrons begin to take part in conduction. In this case, the structure was switched to LRS. When the direction of the negative voltage sweep was changed, the traps remained filled and the LRS was saved. The state was saved even at a positive voltage and did not change until the moment when most of the conduction electrons and electrons captured by the traps did not transitioned into the top electrode. The structure was switched to HRS.

From the point of view under consideration, the appearance of filaments in the oxide during electroforming occurred both near the top electrode (which manifested itself in the emission of electrons from the top electrode into the switching region) and near the bottom electrode (which manifested itself in the formation of a residual filament).

Usually, the presence of traps in an insulator led to a strong decrease in the current at low injection levels, since empty traps could capture most of the injected charge carriers. For the existence of LRS and HRS, it is necessary that there is no thermally activated emission of electrons from the traps, that is, the traps must be deep. On the other hand, switching from LRS to HRS should occur as a result of the emission of trapped electrons from traps.

The following indicated the possibility of using the resistive switching model, due to SCLC mechanism, to analyze the characteristics of the investigated structures after electroforming at a high value of current compliance. First of all, the TEM data, presented for the investigated structures, indicated a significant roughness of the YSZ film at the interface with the top electrode. Therefore, electric field concentrators at the top electrode/YSZ film interface were formed, the presence of which facilitated the emission of electrons from the top electrode into the oxide during electroforming when a negative voltage was applied. The emergence of the mechanism under consideration was also facilitated by the presence in the YSZ of such point defects as C-defects (associated with oxygen vacancies) and T-defects (associated with oxygen divacancies) with sufficiently high concentrations (~10^{20} and ~10^{19} cm^{-3}, respectively

[84]), which are deep centers for conduction electrons and can be located in the defect (associated with oxygen vacancies) band, the so-called α-band (see the energy band diagram of the investigated structure in Figure 13).

As shown in Chapter 3, the Fermi level of Zr was below the bottom of the conduction band of the YSZ and approximately coincided with the position of the α-band, which led to the absence of a barrier for conduction electron in the α-band. Therefore, electroforming at a negative voltage and a high value of current compliance facilitated the filling of deep centers with a high density. Since the concentrations of oxygen vacancies and the considered traps in YSZ are high, it was believed that the main process determining electroforming at a high value of current compliance is the injection of electrons into the filaments. The work function of TiN was 4.2 eV. In accordance with this, the barrier for the transfer of electrons from TiN to the α-band was 0.35 eV and was low, which contributed to the appearance of an ohmic electrode at the oxide/bottom electrode interface during electroforming. This was also facilitated by the fact that, as a result of the diffusion of oxygen ions from YSZ into TiN, a transition layer, containing a mixture of TiO_xN_y compounds, appeared above the TiN surface [90]. The presence of this layer, a high concentration of oxygen vacancies, and an increased electronic conduction determined resistive switching. Thus, in the investigated structures during electroforming the conditions at the YSZ/TiN interface allowed the formation of a residual filament.

Thus, the performed analysis of the experimental characteristics of bipolar resistive switching, which observed in MIM-structures after electroforming at a high value of current compliance, allowed to conclude that bipolar resistive switching in the investigated structures can be caused by electrostatic/electronic effects. The experimental *I–V* curves, characterizing this switching, was approximated within the framework of a model that takes into account the effects of capture of conduction electrons by electron traps and emission of electrons from traps into the YSZ. This made it possible to find out what microscopic processes occur during resistive switching in the investigated structures.

In the case of MIM-structures based on YSZ after electroforming at a low value of current compliance, the processes that determine the electroforming can be both the injection of electrons into the filaments and the movement of oxygen vacancies in the filaments. Since the concentrations of oxygen vacancies and the traps in the YSZ are high, it can be assumed that the electronic processes in the YSZ during electroforming and resistive switching are determined by the energy band diagram shown in Figure 13. In particular, it can be assumed that the electronic conduction in the YSZ is due to the transfer of electrons in the α-band.

It should be noted that the above model of electron current transfer in the memristor is valid for voltages < V_{SET}, V_{RESET}. At voltages close to V_{SET} and V_{RESET}, the resistive switching mechanism changed, for example, to the mechanism of electron direct tunneling from the filament to the electrode.

4.1.4 Influence of temperature on parameters of resistive switching of memristive MIM-structures based on yttria-stabilized zirconia

Below are the results of investigation of the influence of temperature T on the parameters of resistive switching of memristive structures based on YSZ. The I–V curves of the structures were measured in the temperature range 77 – 490 K.

Figure 31 shows the I–V curves of the memristive MIM-structure Au/Zr/YSZ/TiN/Ti/SiO_2/n-Si, obtained at -196, 36, 126, and 231 °C. With an increase in temperature, starting from a certain value of T_c, there was an abrupt decrease in the switching efficiency, which was characterized by the fact that the values of the current in the LRS and HRS approached (the ratio of the resistances R_{HRS}/R_{LRS} decreased) at all considered voltages.

Figure 32 shows the dependences of the current in the LRS and HRS on the inverse temperature of the investigated structure, obtained at V = 0.5 V.

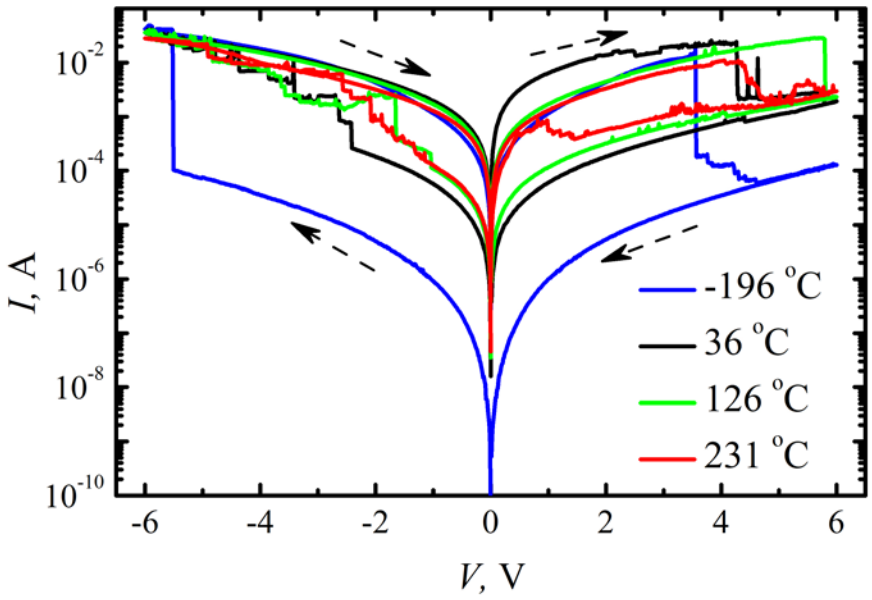

Figure 31. *I–V* curves of the investigated memristive structure obtained at different temperatures. Dashed arrows shows the direction of the voltage sweep

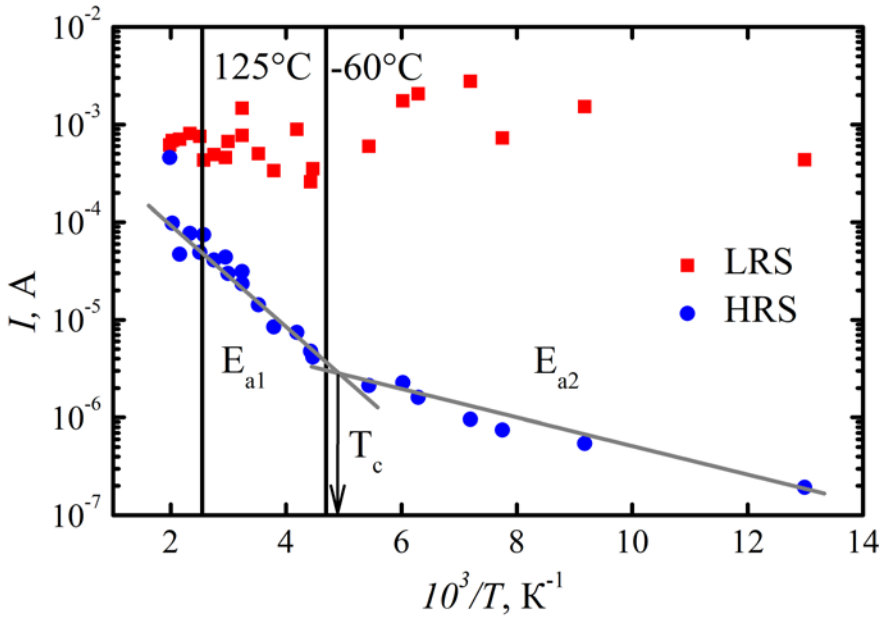

Figure 32. Dependences of the current in the LRS (■) and HRS (●) on the inverse temperature of the investigated structure, obtained at V = 0.5 V

The numerical values of R_{HRS}/R_{LRS} of the investigated structure at certain temperatures and voltage V = 0.5 V are given in Table 6. The error of R_{HRS}/R_{LRS}, indicated in the table, was determined by the scatter of the experimental values obtained from the dependence of the currents in the LRS and HRS at room

temperature on the number of switching cycles in the region in which the ratio R_{HRS}/R_{LRS} was stable. The specified scatter was determined by the stochastic nature of the rupture and restoration of filaments.

Table 6. The numerical values of R_{HRS}/R_{LRS} of memristive structure Au/Zr/YSZ/TiN/Ti/SiO_2/*n*-Si, obtained at temperatures of -60, 22 and 125 °C and V = 0.5 V.

Temperature, °C	-60	22	125
R_{HRS}/R_{LRS}	96.0 ± 6.5	70.0 ± 4.8	11.2 ± 0.8

An important factor determining the decrease in R_{HRS}/R_{LRS} with increasing temperature was the activation behavior of the growth of the current in the HRS at $T > T_c$ (see Figure 32). Based on this data, the values of T_c and activation energies of the growth of the current in the HRS (E_{a1} at $T > T_c$ and E_{a2} at $T < T_c$) were estimated. It should be noted that the dependences shown in Figure 32 generally demonstrates the semiconductor conduction in HRS and the close to metallic conduction in the LRS. Table 7 shows the values of T_c, E_{a1} and E_{a2} for the investigated structure.

Table 7. The numerical values of T_c, E_{a1} and E_{a2} of memristive structure Au/Zr/YSZ/TiN/Ti/SiO_2/*n*-Si

Parameter	T_c, °C	$E_{a1} \pm \Delta E_{a1}$, eV	$E_{a2} \pm \Delta E_{a2}$, eV
Value	-66	0.121 ± 0.012	0.028 ± 0.003

Figure 33 shows the temperature dependences of the current in the LRS, obtained at V = 0.1 V and different values of current compliance.

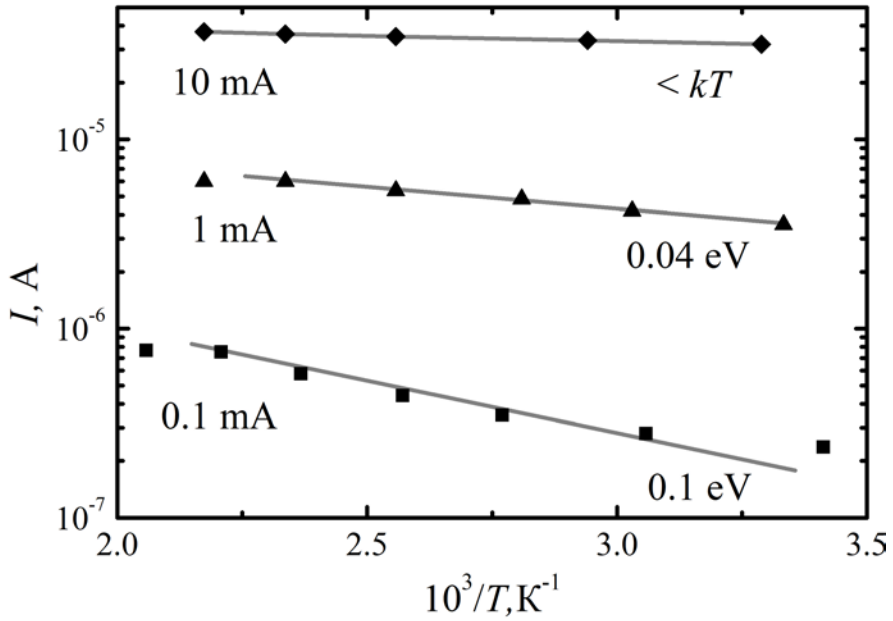

Figure 33.Temperature dependences of the current of the memristive structure Au/Zr/YSZ/TiN/Ti/SiO_2/Si in LRS, obtained at V = 0.1 V and different values of current compliance

These data demonstrate the effect of a decrease in the resistance of the investigated structure in the LRS with an increase in current compliance. It is shown that with an increase in values of current compliance, the value of the resistance decreases by more than an order of magnitude, and the value of the activation energy of this process decreases down to values lower than kT. A decrease in the activation energy is associated with an increase in the density of metal ions in the filaments and a corresponding increase in the electron current.

The above analysis of the temperature dependences of the I–V curves of the memristive MIM-structures Au/Zr/YSZ/TiN/Ti/SiO_2/n-Si is of interest both for studying the mechanisms of electroforming and resistive switching, and for creating elements of resistive memory with increased temperature sustainability.

4.2 Capacitance–voltage curves of memristive MIM-structures based on yttria-stabilized zirconia

This section presents the results of investigation of the admittance of memristive MIM-structure Au/Zr/YSZ/TiN/Ti/SiO_2/*n*-Si ($S \sim 1 \cdot 10^{-2}$ cm^2).

Figures 34–37 show the equivalent circuit of memristor, frequency dependences of capacitance, resistance and dielectric loss tangent of investigated structure in initial state (IS), LRS and HRS. The parameters obtained from the parallel equivalent circuit for capacitor are determined by the processes in the oxide.

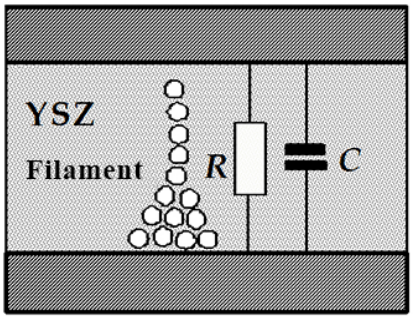

Figure 34. Equivalent circuit of memristor

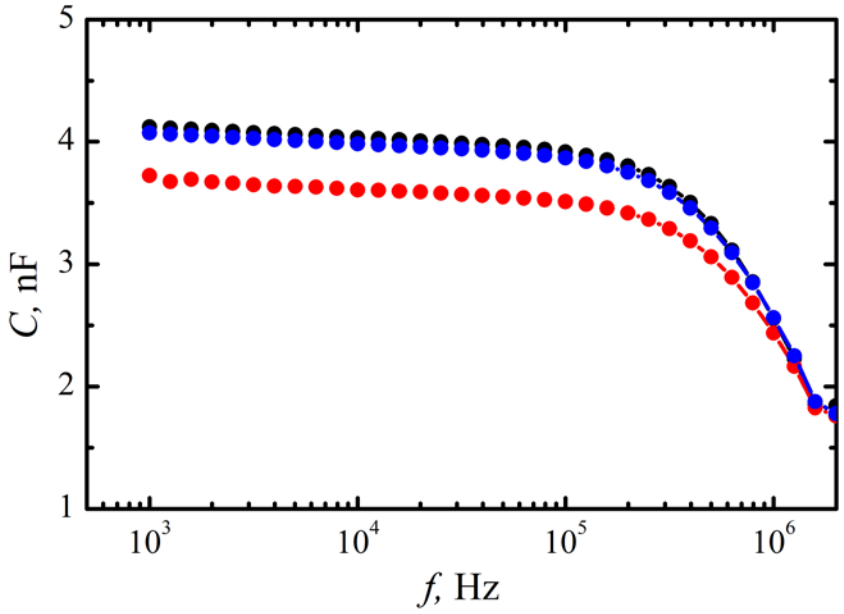

Figure 35. Frequency dependences of capacitance of investigated structure in IS (black), LRS (red) and HRS (blue), obtained from the parallel equivalent circuit for capacitor

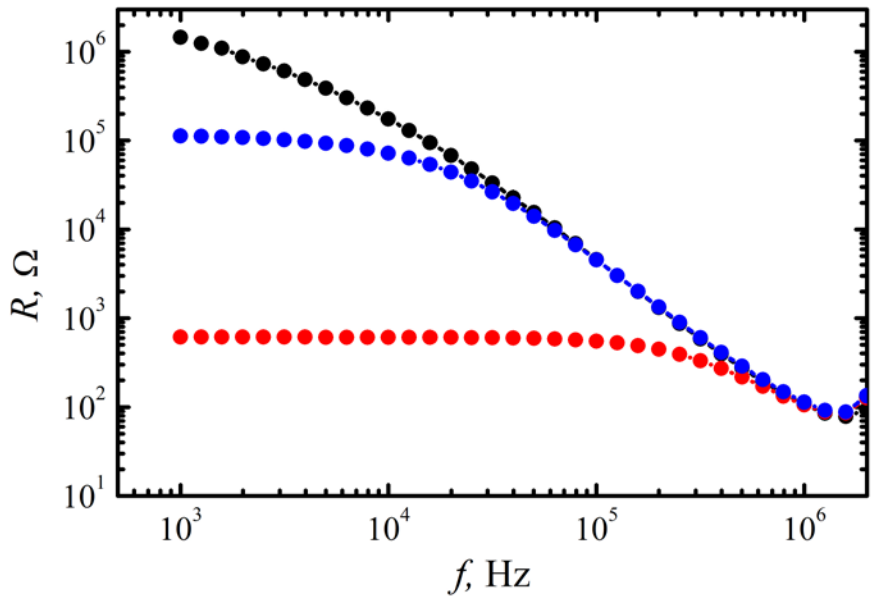

Figure 36. Frequency dependences of resistance of investigated structure in IS (black), LRS (red) and HRS (blue), obtained from the parallel equivalent circuit for capacitor

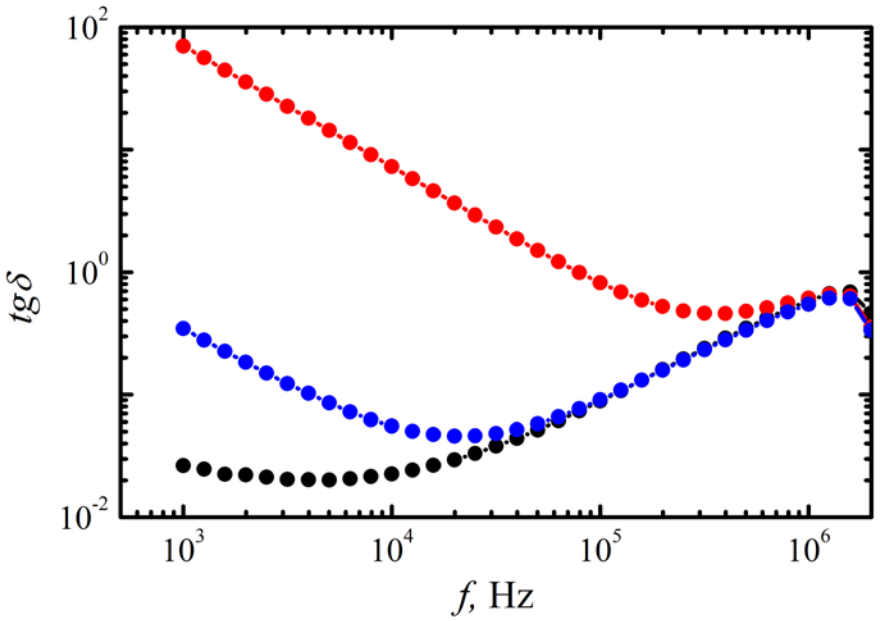

Figure 37. Frequency dependences of dielectric loss tangent of investigated structure in IS (black), LRS (red) and HRS (blue), obtained from the parallel equivalent circuit for capacitor

Small-signal measurements of admittance [74, 75] at V = 0 V were used to determine the values of the dielectric constant (ε_1, ε_2) of YSZ (determined from the value of the capacitance measured from the parallel equivalent circuit for capacitor),

the dielectric loss tangent ($tg\delta_1$, $tg\delta_2$) and resistances (R_1, R_2) of the structure, where 1 refers to a frequency of 1 kHz, and 2 – to a frequency of 100 kHz (Table 8).

Table 8. Parameters of the investigated memristive structure in IS, LRS and HRS, obtained from small-signal measurements of admittance measured from the parallel equivalent circuit for capacitor [A1].

State	ε_1	ε_2	$tg\delta_1$	$tg\delta_2$	R_{p1}, Ω	R_{p2}, Ω
IS	23	22	$2.6\cdot10^{-2}$	$8.9\cdot10^{-2}$	$1.5\cdot10^{6}$	$4.6\cdot10^{3}$
LRS	21	19	70.0	$8.2\cdot10^{-1}$	611	552
HRS	22	21	$3.5\cdot10^{-1}$	$9.1\cdot10^{-2}$	$1.1\cdot10^{5}$	$4.5\cdot10^{3}$

Parameters of MIM-structures in IS were discussed in Chapter 3. Note that the dielectric constant of the YSZ films almost did not change upon switching of the structure. The decrease in dielectric loss tangent in the LRS by almost two orders of magnitude when the frequency changes from 1 kHz to 100 kHz can be associated with the hopping nature of the conduction in the filaments (in the case of low value of current compliance).

It can be concluded that the investigated structure had large dielectric losses in the high-frequency region, while the formation of filaments manifested ohmic losses in the low-frequency region, and the intensity of these losses increased with increasing value of current compliance. It should also be noted that the value of the dielectric loss tangent in HRS determines the contribution of other dielectric loss mechanisms. As can be seen from the Table 8, the difference in the dielectric loss tangent in LRS and HRS is about 2 orders of magnitude, that is, the integral contribution of other dielectric loss mechanisms is negligible compared to the contribution of the filament.

The results of small-signal measurements of admittance make it possible to establish a direct relationship between the dielectric loss tangent and the cross-

sectional area of the filament (as well as its diameter). Figure 38 shows a vector diagram of a real and an imaginary parts of the impedance, which provides theoretical confirmation of the above changes in the dielectric loss tangent ($\delta_1 > \delta_2$, which means $tg\delta_1 = 1/R_{LRS}\omega C > tg\delta_2 = 1/R_{HRS}\omega C$).

It is assumed that in LRS the conduction inside of filament is carried out mainly via metallic bonding, then:

$$R = \frac{\rho_{Zr} \cdot l}{S}, \tag{7}$$

where ρ_{Zr} is the electrical resistivity of Zr ($41 \cdot 10^{-6}$ Ω·cm [97]), l is the filament length (in fact, YSZ film thickness – 40 nm), S is the cross-sectional area of the filament.

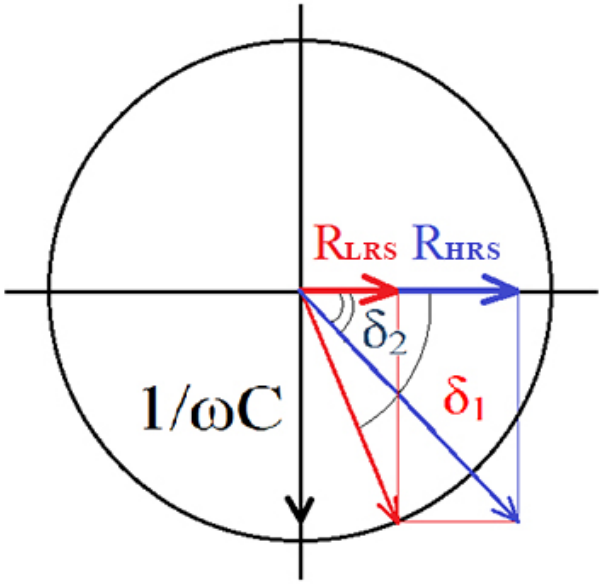

Figure 38. Vector diagram of a real and an imaginary parts of the impedance of the memristor

The filament diameter can be estimated using the following equation:

$$d = \sqrt{\frac{4S}{\pi}} \tag{8}$$

The results are shown in Table 9.

Table 9. Cross-sectional area and diameter of the filament.

State	S (at f = 1 kHz)	S (at f = 100 kHz)
LRS	26.82 nm^2	29.64 nm^2
	d (at f = 1 kHz)	d (at f = 100 kHz)
HRS	5.84 nm	6.14 nm

The obtained values are in good agreement with the data available in the literature [89]. The number of atoms in one filament with such a diameter is about 400.

The results obtained in this section indicate that the dielectric loss tangent is a macroscopic parameter that makes it possible to control the formation of a filament in the insulator and to characterize its current-carrying capability.

4.3. Electroforming and resistive switching of memristive devices based on yttria-stabilized zirconia

This section demonstrates the results of the development and research of memristive devices on the basis of MIM-structures Au (40 nm)/Zr (8 nm)/YSZ (40 nm)/TiN (25 nm)/Ti (25 nm)/SiO_2 (500 nm)/Si.
To implement this task, end-to-end computer-aided design Cadence and topological editor Virtuoso was used (E.G. Gryaznov, Russian Federal Nuclear Center – All-Russian Scientific Research Institute of Experimental Physics «Measuring Systems Research Institute named after Yu.Ye. Sedakov»). A photo of a test crystal with memristive devices (after packaging into standard closed metal/ceramic integrated circuit packages) is shown in Figure 39.

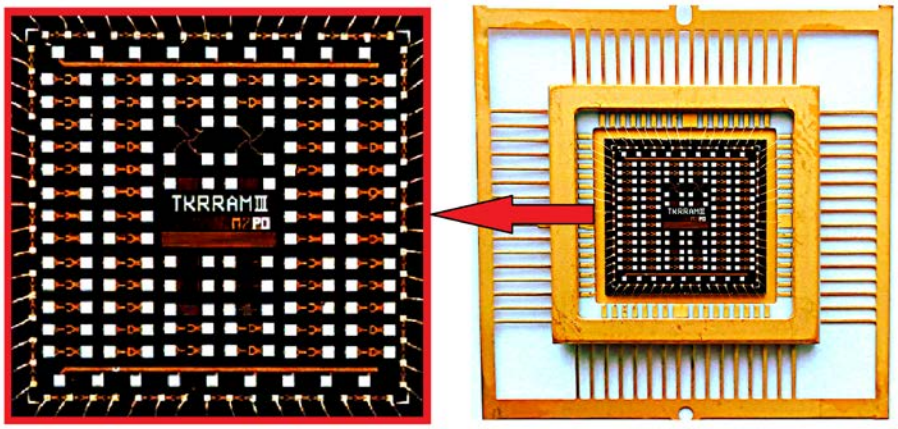

Figure 39. A photo of a test crystal with memristive devices

This test crystal was developed taking into account scientific and technological solutions and design options obtained at the previous stages of the investigation. It should be noted that for the developed topology, the frequency of occurrence of critical defects (for example, rupture of the contact of memristive elements) was ~ 4%. Device yield in the peripheral area was 91%. Figure 40 shows microscopic images of memristive devices with an area of 100×100 μm^2 before and after electroforming and resistive switching. It can be seen that no visible changes occurred after electroforming and resistive switching. Figure 41 shows the *I*–*V* curves of one of the memristive devices with an area of 20×20 μm^2.

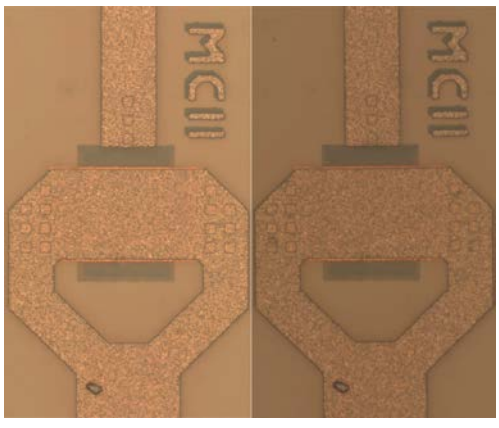

(a) (b)

Figure 40. Microscopic images of memristive devices before (a) and after (b) electroforming and resistive switching

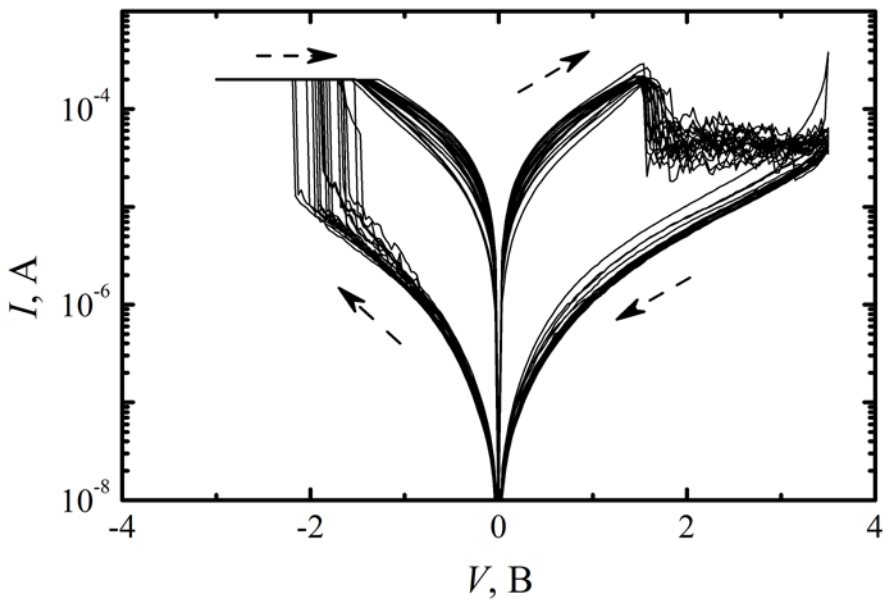

Figure 41. The first 20 cycles of resistive switching of one of the memristive devices. Dashed arrows shows the direction of the voltage sweep

Electroforming was carried out at -9.8 V. The measurements were carried out between the pins of the package in a cyclic mode at room temperature and a current compliance 200 μA. Selection of the optimal combination of current compliance during SET and voltage sweep during RESET made it possible to obtain switching between reproducible resistive states in a given range of resistances.

Memristive devices demonstrated up to 10^6 switches (with final sticking in HRS) and the ratio of resistances in HRS and LRS > 10 (Figure 42), switching time ~ 70 ns (Figure 43) and operating temperature up to 125 °C (Figure 44). It should be noted that the obtained value of the switching time is limited by the capabilities of the experimental setup, that is, the real switching time of the memristive device may be less than or equal to the obtained value.

The value of lifetime of device (i.e. endurance), shown on Figure 42, are shorter with a respect to memristive devices, based on Ta_2O_5 [98] and HfO_2 [99]; also, the value of switching time, shown on Figure 43, are longer with a respect to the same memristive devices [98, 99]. In fact, memristive devices $Pt/Ta_2O_{5-x}/TaO_{2-x}/Pt$ demonstrated up to 10^{12} switches with switching time ~ 10 ns [98] and memristive

devices Ta/HfO_2/Pt demonstrated up to ~10^{11} switches with switching time ≤ 5 ns [99]. However, these memristive devices also have disadvantages. The value of current in the HRS (and, accordingly, the ratio of currents in LRS and HRS) strongly depended on the cell size [98]: I_{LRS}/I_{HRS} <10 in the case of a cell size of 0.5×0.5 μm^2; I_{LRS}/I_{HRS} > 10 in the case of a cell size of 30×30 μm^2, but the value I_{HRS} varied chaotically within two orders of magnitude throughout all switching cycles. And also, the ratio of resistances in HRS and LRS is ~ 2.5 [99], which is much less than the result given in this section. Moreover, a two-layer dielectric memristive device can be considered to improve all of these parameters. This approach was done in [100], where devices Au/Ta/YSZ/Ta_2O_5/TiN/Ti demonstrated a significant stabilization of I_{LRS}/I_{HRS} after several hundred cycles and a complete absence of changes in the magnitude of I_{LRS} and I_{HRS} for 10^4 seconds at room temperature.

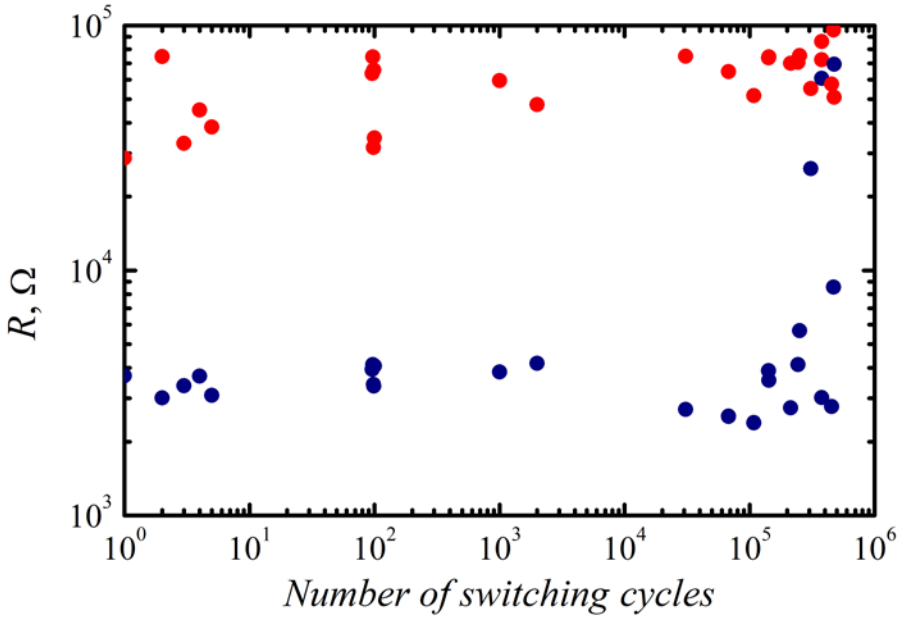

Figure 42. Dependence of resistance in LRS (red) and HRS (blue) of memristive devices on the number of switching cycles (switching amplitude +2.86 V / -6.6 V, reading amplitude 1.76 V)

It should be noted that the latest (at the time of writing this dissertation work) developed and constructed (together with an industrial partner Russian Federal Nuclear Center – All-Russian Scientific Research Institute of Experimental Physics

«Measuring Systems Research Institute named after Yu.Ye. Sedakov») test crystal topology provides for the combination of memristive devices into a passive cross-point 16×16 for subsequent use as a weight matrix in the development of neuromorphic systems (Figure 45).

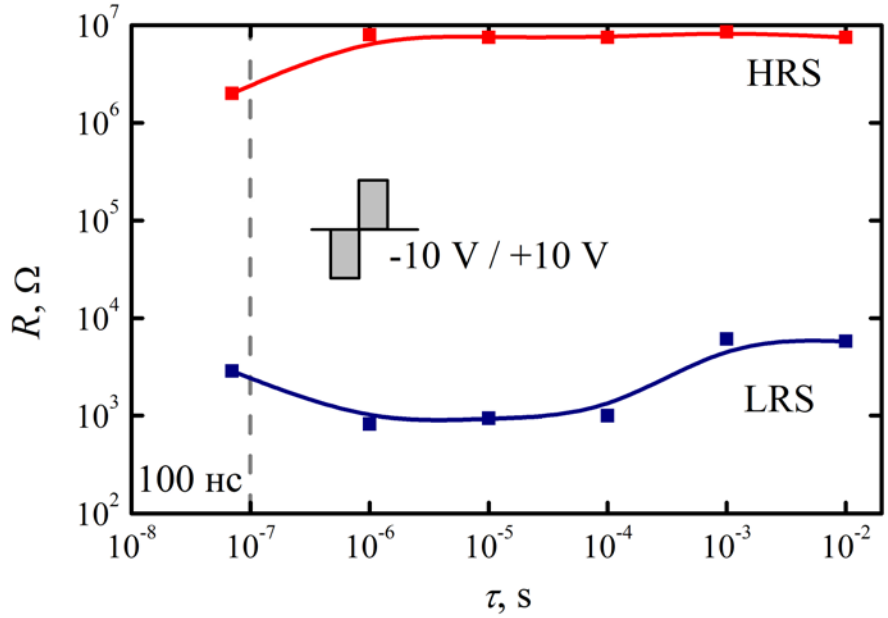

Figure 43. Dependence of resistance in HRS (red) and LRS (blue) of memristive devices on the duration of a switching pulse with an amplitude ± 10 V

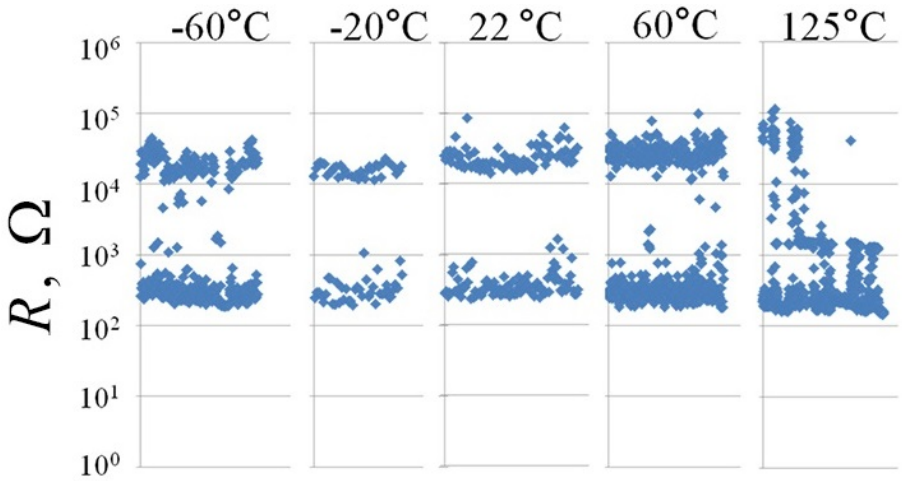

Figure 44. Temperature tests of memristive devices

Thus, stable resistive switching with a small scatter of switching parameters of memristive devices on the basis of MIM-structures Au (40 nm)/Zr (8 nm)/YSZ (40 nm)/TiN (25 nm)/Ti (25 nm)/SiO_2 (500 nm)/Si, developed and constructed together with an industrial partner Russian Federal Nuclear Center – All-Russian Scientific Research Institute of Experimental Physics «Measuring Systems Research Institute named after Yu.Ye. Sedakov». Memristive devices demonstrated up to 10^6 switches, switching time ~ 70 ns, operating temperature up to 125 °C and the ratio of resistances in HRS and LRS > 10.

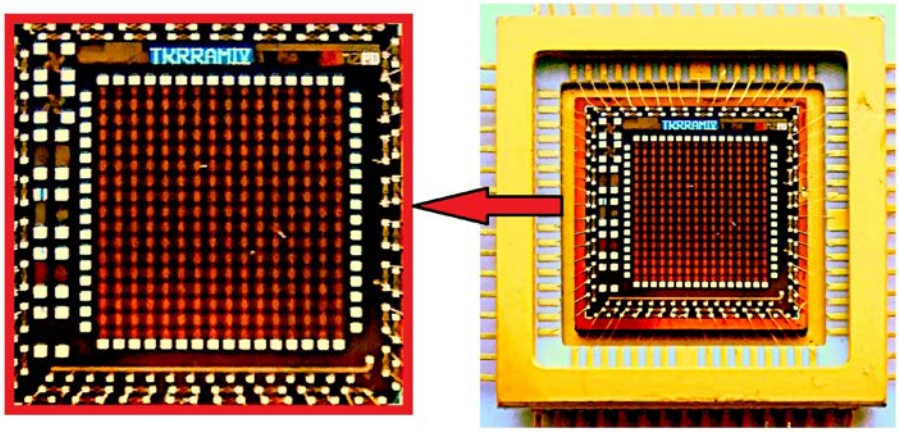

Figure 45. A photo of a test crystal with memristive devices combined into a passive cross-point 16×16

4.4. Main results of Chapter 4

It was found that the mechanism of current transfer in the investigated MIM-structures is space-charge-limited current. The conduction in LRS and HRS was of an activation behavior. The activation energy of conduction in the LRS decreased with increase in value of current compliance, and, accordingly, the behavior of the conduction tended to be metallic.

It was found that resistive switching was accompanied by a change in the dielectric loss tangent, which is due to the rupture and restoration of filaments.

It was found that the investigated structures demonstrated the resistive switching at high temperatures (up to 125 °C), which indicated that these structures are promising for creating elements of resistive memory with increased temperature sustainability.

Memristive devices were prepared on the basis of the investigated MIM-structures. Devices demonstrated up to 10^6 switches, switching time ~ 70 ns, operating temperature up to 125 °C and the ratio of resistances in HRS and LRS > 10.

CHAPTER 5. Resistive switching of memristive MIS-structures based on yttria-stabilized zirconia stimulated by optical radiation

Electroforming and resistive switching are studied in most cases in metal-insulator-metal (MIM) structures. These processes are primarily determined by the electric field strength in the insulator. Therefore, it is possible to use corresponding (with the same top electrode and insulator) metal-insulator-semiconductor (MIS) structures instead of MIM-structures.

At the same time, the manifestation of the resistive switching effect in MIS-structures is associated with two fundamental circumstances. On the one hand, the presence of two metal electrodes in MIM-structures complicates, especially in the case of symmetric structures, the identification of phenomena, occurring at the interfaces of the insulator with the top and bottom electrodes, in the investigation of electroforming and resistive switching. On the other hand, using of a semiconductor as one of the electrodes of the memristive structure and applying currently well developed methods for studying the electrical properties of MIS-structures make it possible to obtain a variety of information about electronic and ionic processes in an insulator, at the interface between an insulator with a semiconductor and a metal electrodes during electroforming and resistive switching. In addition, MIS-structures, demonstrating resistive switching, have a higher functionality than the corresponding MIM-structures. For example, the influence of optical radiation on the MIS-structure can be used to control the resistive switching.

The effect of light-induced resistive switching has also been studied in other oxide matrices, for example, Al_2O_3 [101], SiO_x [102] and graphene oxide [103]. In [101] it was shown that memristive structures $Pd/Al_2O_3/SiO_2/p$-Si demonstrated resistive switching under the influence of optical radiation by LED with a wavelength of 390 – 950 nm. In contrast to the reasoning given in this chapter, the authors of [101] associate the effect of light-induced resistive switching with the modulation of trapped electrons in the Al_2O_3 layer. In the case of $V > 0$, electrons, photogenerated in

silicon, are injected into the Al_2O_3 layer and saturate it, thereby increasing its resistivity. Thus, high resistance state (HRS) is achieved. And low resistance state (LRS) is achieved due to the gradual removal of trapped electrons from the Al_2O_3 layer when $V < 0$ is applied. The authors of [102] have shown that memristive structures ITO/SiO_x/*p*-Si, where ITO – indium tin oxide, demonstrated resistive switching under the influence of laser radiation with a wavelength of 410 – 650 nm, as well as white light from a tungsten filament bulb. The authors argue that the mechanism responsible for the effect of light-induced resistive switching is to enhance the injection of electrons into traps in the oxide layer (due to the generation of electron-hole pairs in a silicon electrode using optical radiation) and the subsequent generation of Frenkel pairs, which, in turn, stimulates the formation of oxygen vacancies and, accordingly, the formation of filaments. The latter is due to the fact that Frenkel pairs consist of oxygen vacancies and oxygen interstitial ions with a low value of the height of migration barriers (around 0.2 eV). In [103], the effect of optical radiation of a LED with a wavelength of 380 – 625 nm on the resistive switching of two types of memristive devices based on graphene oxide (vertical (Ag/graphene oxide/ITO) and planar (ITO/graphene oxide/ITO)) was studied. The authors argue that both types of devices showed significant photoconductivity effects. This effect is explained by the photoexcitation of electrons into the conduction band of graphene oxide. It should be noted that, in the case of long wavelength radiation, the effect of photoconductivity was purely reversible, while in the case of ultraviolet radiation there was both the effect of reversible photoconductivity and an irreversible change in the electrical properties due to the reduction of graphene oxide.

Separately, it is worth highlighting the works devoted to memristive electro-optical converters: a programming electrical input signal is converted into an optical output (electronics-to-optics modulation) [104] and a programming optical input signal is converted into an electrical output (optics-to-electronics detection) [105]. The authors of [104] considered atomic scale plasmonic switch. In this work, a

silicon waveguide was connected to memristive device Ag/*a*-Si/Pt. Depending on the applied voltage, the atomic-scale Ag filament was restored or ruptured. In the case of a ruptured filament, the transmission spectrum has a pronounced minimum at a wavelength of 1450 nm. This behavior is mainly due to the excitation of plasmon resonance. In the case of the restored filament, the transmission spectrum has a pronounced minimum at a wavelength of ~ 1350 nm. Thus, when a radiation source with a wavelength of 1450 nm was used at the input, the authors obtained a weak change in the radiation intensity in the case of a restored filament and a strong decrease in the intensity (i.e., almost complete absorption) of radiation in the case of a ruptured filament. The authors of [105] also considered atomic scale photodetection enabled by a resistive switching in memristive system Ag/SiO_2/Pt. When light is turned on, the resistance abruptly increases due to the partial rupture of the Ag filament under the influence of the thermal diffusion prevailing at this moment. When the light is turned off, the resistance abruptly decreases by several orders of magnitude due to the restoration of the filament under the influence of the electric field prevailing at this moment.

One should also note the works in which the effect of light-induced resistive switching in memristive devices with organic materials in their composition was discovered. For example, in [106] investigated device consisted of vertically oriented ZnO nanorods coated with a photoactive azobenzene polymer, poly(disperse red 1 acrylate). Optical radiation caused trans-cis isomerization of azobenzene molecules, which expanded or contracted the polymer layer and changed the resistance of resistive states, their ratio, and retention time. In [107] investigated device consisted of vertically oriented Au nanorods (fabricated by electrodeposition of Au into substrate-supported porous Al_2O_3 templates), poly-L-histidine and eutectic alloy composed of Ga and In. Each Au nanorod forms a tunnel junction with the top GaIn contact. During the tunneling process, the inelastically tunneled electrons excite plasmons in the nanorod, which can subsequently decay radiatively into photons, whereas those electrons that elastically tunnel generate hot electrons in the tips of the

nanorods. The hot electrons can be harvested for inducing chemical reactions in a chosen gas environment. The gas environment can promote oxidation or reduction reactions, or maintain an inert state with or without applied bias. Thus, the gas environment affects the resistivity of the tunnel junction. Optical coding of the tunnel junctions is also possible using hot electrons generated in the tunnel junctions by an external optical radiation in the respective gas environments. Under external optical radiation of the nanorod from the substrate side, the plasmonic modes are excited. The plasmonic excitation exists across the whole nanorod length, and hot electrons are generated not only at the side walls in the lower part of the nanorods but also at their tips; the latter can be used directly for the activation of chemical reactions in the tunnel junctions.

Section 5.1 presents the results of investigations of the influence of optical radiation on the resistive switching of memristive MIS-structures based on yttria-stabilized zirconia (YSZ) on Si substrates. Section 5.2 summarizes the results obtained in Chapter 5.

5.1. Electrical properties of memristive MIS-structures based on yttria-stabilized zirconia, demonstrating resistive switching stimulated by optical radiation

This section shows resistive switching of memristive MIS-structures Au/Zr/YSZ/Sb/SiO_2/*n*-Si stimulated by optical radiation. The methods of preparation of studied MIS-structures are described in Chapter 2. The properties of the original (before electroforming) structures are described in Chapter 3. The values of the density of surface states in the investigated structures, determined from measurements of small-signal capacitance-voltage and conductance-voltage characteristics, are given in Chapter 3. Photoexcitation was carried out with unfocused white light from a halogen lamp (50 W). Figure 46 shows the cyclic

current-voltage characteristics (*I–V* curves) of memristive MIS-structures Au/Zr/YSZ/Sb/SiO_2/*n*-Si, measured in the dark and under illumination.

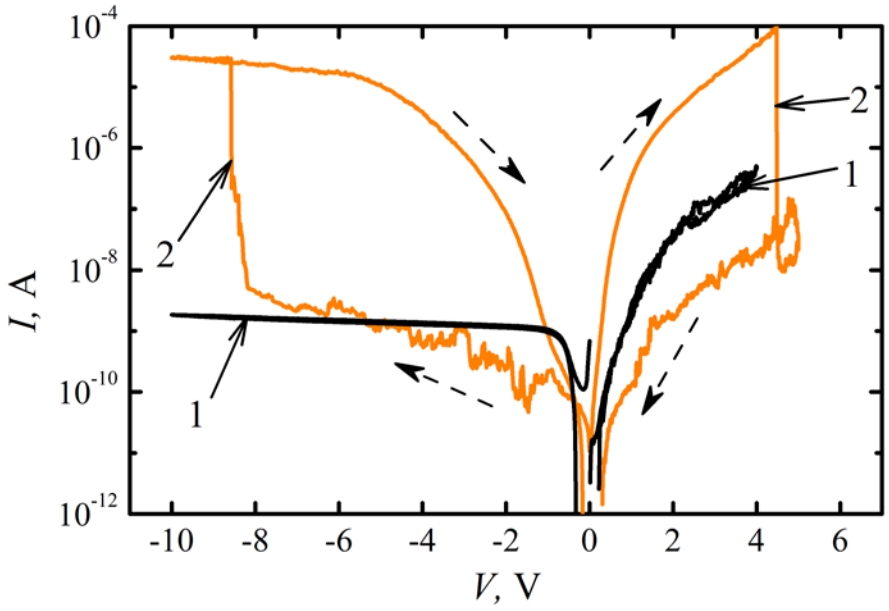

Figure 46. Cyclic *I–V* curves of memristive MIS-structures Au/Zr/YSZ/Sb/SiO_2/*n*-Si, measured in the dark (1) and under illumination (2). Dashed arrows shows the direction of the voltage sweep [A6]

Hysteresis was not observed on the *I–V* curves measured in the dark (Figure 46, curve 1). Photoexcitation led to the appearance of a hysteresis on the *I–V* curves associated with the formation of filaments in the YSZ layer (electroforming) and resistive switching with further cyclic voltage sweep (Figure 46, curve 2). The ratio R_{HRS}/R_{LRS} was ~ 2 orders of magnitude, as in the case of MIM-structures (see Chapter 4).

The mechanism of the influence of optical radiation on the resistive switching was as follows. Figure 47 qualitatively shows the energy band diagram of the inversely shifted MIS-structure ($V < 0$) in the dark and under illumination with a photon energy $h\nu > E_g$ (E_g is the band gap of Si). Under the action electromagnetic radiation with a photon energy $h\nu > E_g$, electron-hole pairs were generated in the Si substrate due to interband optical absorption.

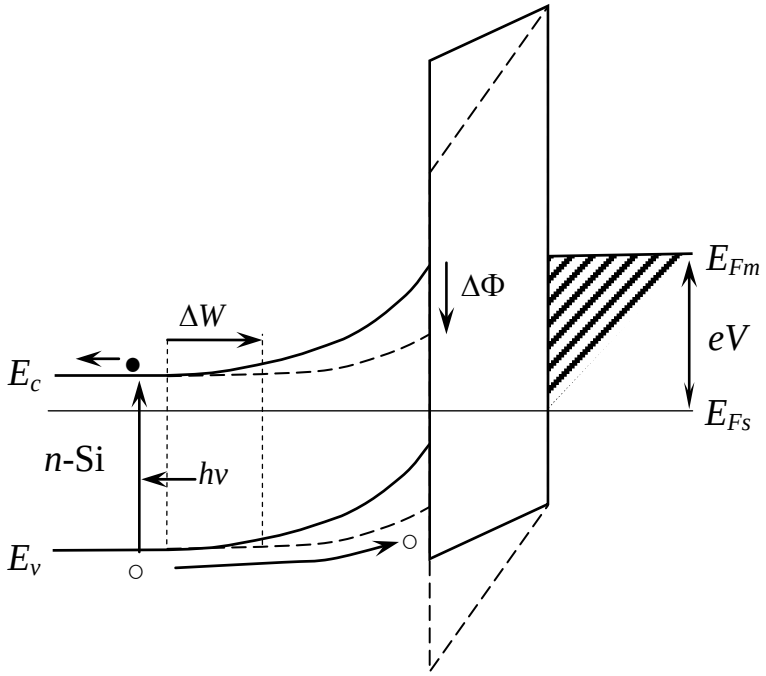

Figure 47. Energy band diagram (qualitatively) of MIS-structure on *n*-Si substrate, when applying reverse bias, in the dark (solid line) and with interband photoexcitation with a photon energy $h\nu > E_g$ (dashed line)

Since the coefficient of interband optical absorption Si $\alpha \sim 1$ cm^{-1} at $h\nu \sim E_g$ [77], the most of optical radiation was absorbed in the substrate outside of the space charge region (SCR) of the semiconductor/insulator barrier. In this case, excess minority charge carriers (holes) diffused to the SCR boundary of the semiconductor/insulator barrier. Then, under the influence of the electric field of the SCR, the holes were transferred to the semiconductor/insulator interface, where they were accumulated in a triangular potential well near the interface. As a result, the external voltage V was redistributed between the SCR and the insulator, so that the electric field strength in the insulator increased, thereby stimulating electroforming and resistive switching.

The change in the height of the potential barrier at the semiconductor/insulator interface $\Delta\Phi$ in the case of a low intensity of photoexcitation can be estimated by the equation [108]:

$$\Delta\Phi \cong \frac{qkT}{e}\ln\left(1+\frac{eI_0}{j_s}\frac{\alpha L_p}{1+\alpha L_p}\frac{S}{S+D_p/L_p}\right), \quad (9)$$

where e is the elementary charge, q and j_s are the quality factor and saturation current of the MIS-diode, respectively, I_0 [photon/(cm^2·s)] is the intensity of photoexcitation at the semiconductor/insulator interface, L_p (D_p) is the length (coefficient) of diffusion of minority charge carriers in a semiconductor (in the case of a n-Si – holes), S is the surface recombination rate at the semiconductor/insulator interface. The latter determines the excess concentration of holes in a triangular potential well near the semiconductor/insulator interface in a stationary state (in this case, the surface recombination rate is equal to the rate of holes influx to the SCR boundary) [109]. It should be noted that the effect of photoexcitation on the resistive switching was most pronounced in MIS-structures, in which passivating Sb layers were embedded at the YSZ/SiO_2 interface. These structures were characterized by a lower density of surface states (compared to structures without passivating Sb layers, see Chapter 3) and, accordingly, a lower surface recombination rate.

A decrease in the height of the potential barrier at the semiconductor/insulator interface under illumination ($\Delta\Phi$) was accompanied by a decrease in the SCR thickness W by ΔW (Figure 47). In the case of weak photoexcitation (concentration of excess electrons and holes Δn, $\Delta p << N_D$, N_D is the concentration of shallow donors in n-Si), the SCR thickness W is related to $\Delta\Phi$ by the Schottky equation:

$$W = \sqrt{\frac{2\varepsilon\varepsilon_0(\varphi_0 - \Delta\Phi)}{eN_D}}, \quad (10)$$

where ε is the semiconductor dielectric constant, φ_0 is the height of the potential barrier semiconductor/insulator in the dark.

Note that equation (9) is valid as long as the condition $\Delta\Phi << \varphi_0$ is satisfied. In the case of $I_0 \to \infty$, $\Delta\Phi \to \varphi_0$ and undergoes saturation, while Δn, $\Delta p >> N_D$, and $W \to 0$.

In the case of $V > 0$ and under illumination, the majority charge carriers (electrons) accumulated at the semiconductor/insulator interface, which also led to a decrease in φ_0, an increase in the electric field strength in the insulator, a decrease in the SCR thickness W, and, as a result, electroforming and resistive switching have been stimulated.

Thus, in both cases ($V < 0$ and $V > 0$), the interband photoexcitation of excess charge carriers in the Si substrate led to a decrease in the voltage drop across the SCR of the semiconductor/insulator barrier and, accordingly, to an increase in the voltage drop across the insulator, which, in turn, led to a decrease in both V_{SET} and V_{RESET}.

The above-described mechanism of the influence of optical radiation on the resistive switching in MIS-structures includes the interband mechanism of optical absorption in a semiconductor, accompanied by the generation of electron-hole pairs. Thus, for the implementation of such mechanism of the influence of optical radiation on the resistive switching in MIS-structures, photoexcitation with the photon energy $h\nu > E_g$ is necessary.

Figure 48 shows the photosensitivity spectrum (PS) S_{ph} (300 K), measured in the mode of small-signal photo-electromotive-force at $V = 0$, of the studied MIS-structure. The spectrum observed a band of the intrinsic PS of Si in the range of photon energies $h\nu > 1.0$ eV, due to intrinsic optical absorption in the Si substrate. This band overlapped with the maximum of the emission spectrum of the halogen lamp (the emission wavelength of the maximum is ~ 1 μm) used for photoexcitation. Note that the band gap of the YSZ (5.5 eV [72]) was far in the ultraviolet region of the spectrum, beyond the blue edge of the emission spectrum of the halogen lamp, so that the YSZ film was almost transparent for the used photoexcitation.

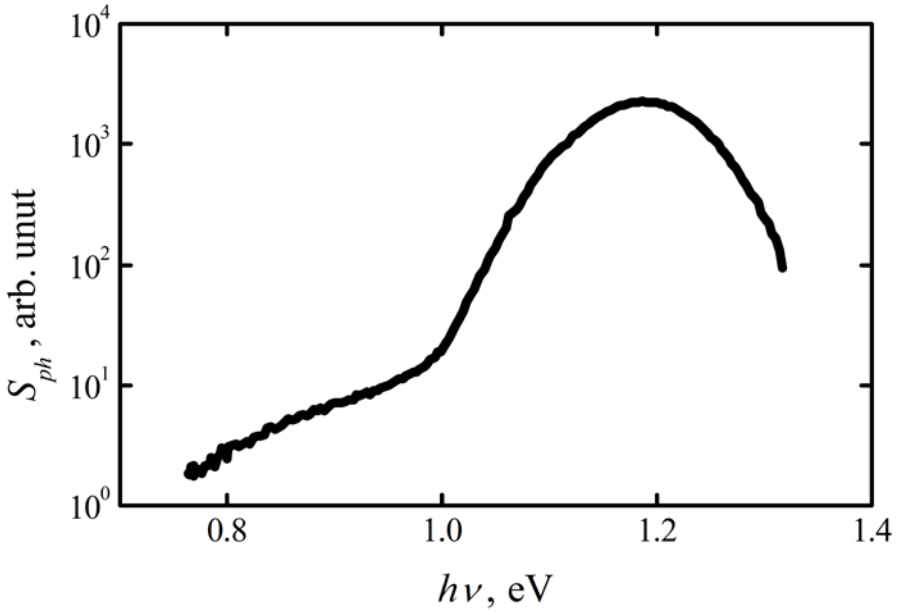

Figure 48. Photosensitivity spectrum (300 K) of memristive MIS-structure based on YSZ on Si substrates [110]

In addition to the band of the intrinsic PS of Si (in the range of photon energies $h\nu > 1.0$ eV), in the spectrum of the PS (Figure 48), a band of the impurity PS was observed in the spectral region $h\nu < 1.0$ eV. This result indicated the influence of photoexcitation on the resistive switching in MIS-structures, possibly also in the case of impurity absorption.

5.2. Main results of Chapter 5

Thus, this chapter shows the stimulation by optical radiation of resistive switching of memristive MIS-structures. This effect is associated with the redistribution of the voltage between the insulator and the semiconductor, caused by the appearance of photo-electromotive-force at the semiconductor/insulator barrier due to interband optical absorption in the *n*-Si substrate. The influence of optical radiation was most pronounced in MIS-structures, in which passivating Sb layers were embedded at the YSZ/SiO_2 interface.

CHAPTER 6. Noise-induced resistive switching of the memristors based on yttria-stabilized zirconia

The current understanding of the resistive switching mechanism in the metal oxides is based on the concept of the formation of the conductive filaments consisting of the oxygen vacancies. The switching of a memristor from low resistance state (LRS) to high resistance state (HRS) is achieved by the rupture of the filament by a voltage pulse (so-called RESET process). The filament can be restored by a voltage pulse of the opposite polarity that results in the switching from HRS back to LRS (so-called SET process). It should be emphasized that the resistive switching is a stochastic process. In fact, the intrinsic fluctuations in structure, chemistry, physical values and switching times, which can occur on multiple lengths and time scales during switching events, are of a stochastic nature and this causes the stochastic of resistive switching [111-115]. Moreover, this is also related to typical small size of the filament cross-section, which falls into the range from 1 to 10 nm [116]. Usually, the rupture and restoring of the filaments in oxides takes place randomly at its interface with one of the electrodes through the jumps of the oxygen ions via the oxygen vacancies in a small volume (several cubic nanometers) near the filament tip. A very limited (countable) number of the oxygen ions (or the oxygen vacancies) are involved into the resistive switching [117]. The aforementioned factors, from one switching cycle to another (so-called cycle-to-cycle scatter), lead to a wide dispersion of the resistive switching parameters, such as the switching voltage from HRS to LRS (V_{SET}) and back (V_{RESET}), etc., which can reach one hundred percent [118]. The natural dispersion of the resistive switching parameters currently limits the application of the memristors [89, 119].

The memristor can be treated as a bistable (in the simplest case) or multistable nonlinear system. It should be noted that the coexistence of several metastable states for a given set of parameters has been observed in many natural and experimental systems in such different areas as laser and semiconductor physics, chemistry,

ecology, neuroscience, climate dynamics (see the review [120] and references therein). Multistable systems are characterized by a high degree of complexity in their behavior due to the «interaction» among the attractors and can be describe by the methods of statistical physics. Specifically, in such systems, the well-known stochastic resonance phenomenon [121-124] can occur, where noise plays a constructive role [125-130]. In fact, there are many known examples of classical and quantum physics, in which the synergistic cooperation between the non-linearity of the system and the environmental noise gives rise to counterintuitive dynamical behaviors [131-150].

Within the framework of the above-mentioned approach, from a theoretical point of view a memristor can be described by a two-well (or more complex) potential profile. Several authors attempted to apply this approach. Moreover, some phenomena inherent to the stochastic multistable systems have been observed experimentally in memristors. In particular, the beneficiary role of adding the white noise to the switching pulses on the stability of the resistive switching parameters has been observed [141]. However, it is still unclear whether this approach is applicable for the description of memristors.

The results of the experimental investigations of resistive switching of memristive devices based on yttria-stabilized zirconia (YSZ)/Ta_2O_5 under a white Gaussian noise signal are presented in Section 6.1. The results of the experimental investigations of the response of the contact between a conductive atomic force microscope probe and an YSZ film on a conductive substrate to an external digitally synthesized noise signal are presented in Section 6.2. Conductive Atomic Force Microscopy (CAFM) has been proven to be a powerful tool for studying the local resistive switching at the nanometer scale [151, 152]. In such experiments, the CAFM-probe contact to an insulator film on a conductive substrate can be treated as a nanometer-sized virtual memristor. Typical size of the contact area between the metal-coated CAFM-probe tip and YSZ films D_p is < 10 nm at reasonable loading forces F_n ~ 1 nN [66] that matches the expected sizes of memristors in future RRAM

devices [153]. So far, CAFM-probe contact to the insulator film surface on a conductive substrate appears to be a good model system for studying the local resistive switching at the nanometer scale [154]. Particularly, the electrical properties of individual filaments can be studied using CAFM. Section 6.3 summarizes the results obtained in Chapter 6.

6.1. Noise-induced resistive switching of memristive devices based on yttria-stabilized zirconia

This section presents the results of the experimental investigations of resistive switching of memristive devices based on YSZ/Ta_2O_5 under a white Gaussian noise signal. Sample preparation and method of investigation are described in Chapter 2. Memristive devices based on YSZ/Ta_2O_5 have been selected as sample objects for experimental studies because of the longer duration of such devices [100].

In Figure 49 the typical cyclic current-voltage characteristics (*I*–*V* curves) of the investigated memristive devices is shown, including the electroforming process and several hysteresis loops, typical for bipolar resistive switching. Due to the asymmetry of the structure, different values of V_{SET} ~ -1.5 V and V_{RESET} ~ +2.4 V are measured.

In this investigation, the waveforms of the current flowing through the memristive device $I(t)$ were recorded subject to the parameters of the input noise signal σ_V and V_{offset}. Three typical waveforms $I(t)$ and respective distribution histograms of I, under the external noise signal with V_{offset} = 0.5 V and with different values of σ_V, are shown in Figure 50. For some parameters of the noise signal, the memristive device switches between HRS and LRS as a random telegraph signal (RTS) (see Figure 50b). This behavior is typical for bistable or even multistable systems in a heat bath.

In the following Figure 51 is shown the plot of the parameter space, $\sigma_V - V_{offset}$, in which the continuous resistive switching was observed (black triangles) or was not

observed (white circles). Specifically, the experiments, in which the continuous resistive switching of the memristive device under the noise signal was observed, are marked by black triangles. These points define a field in the space of the experiment parameters, inside which the noise-induced continuous resistive switching of the memristive device takes place. Outside this field, the memristive device acts as nonlinear resistor being either in HRS (see Figure 50a) or in LRS (Figure 50c). Accordingly, the respective distribution histograms of I deviates from the Gaussian one, inherent to the input noise signal (see the right panels of Figure 50).

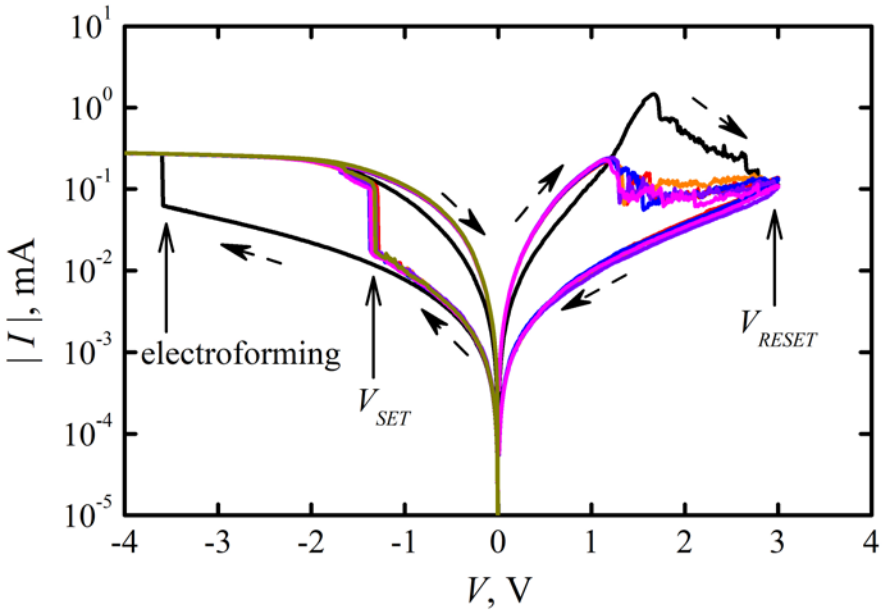

Figure 49. Electroforming and typical *I–V* curves of the investigated memristive devices, obtained at current compliance 300 μA. Arrows shows the direction of the voltage sweep [A7]

In order to analyze the distribution of the current *I*, the cyclic *I–V* curve of an ideal memristor was considered (Figure 52a). The branches corresponding to HRS and LRS are represented by linear functions, that is, the memristor is represented as a linear switching device. Consider a random voltage with Gaussian distribution applied to the memristor. In HRS, the distribution of the current through the memristor *I* will be Gaussian. In LRS, the distribution of *I* will be Gaussian too, but its width will be greater than in HRS. If the memristor switches between HRS and

LRS many times within an observation period of time, the resulting distribution of I would be a superposition of two Gaussian functions with respective widths.

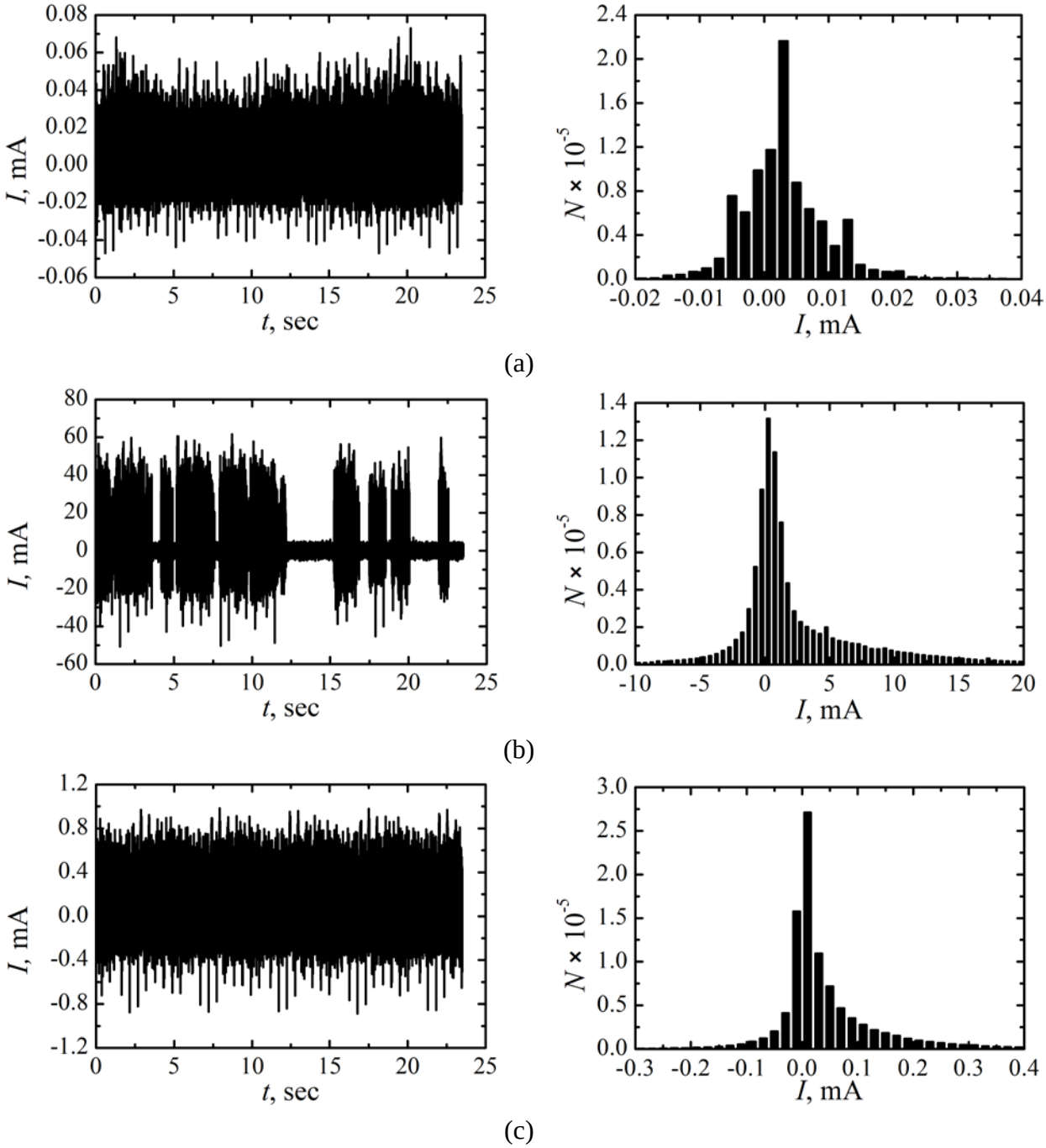

Figure 50. Typical waveforms (left) and related distribution histograms (right) of the current flowing through the memristive device under the noise signal with V_{offset} = 0.5 V and σ_V, V: 0.4 (a), 0.75 (b), and 1.2 (c) [A7, A16]

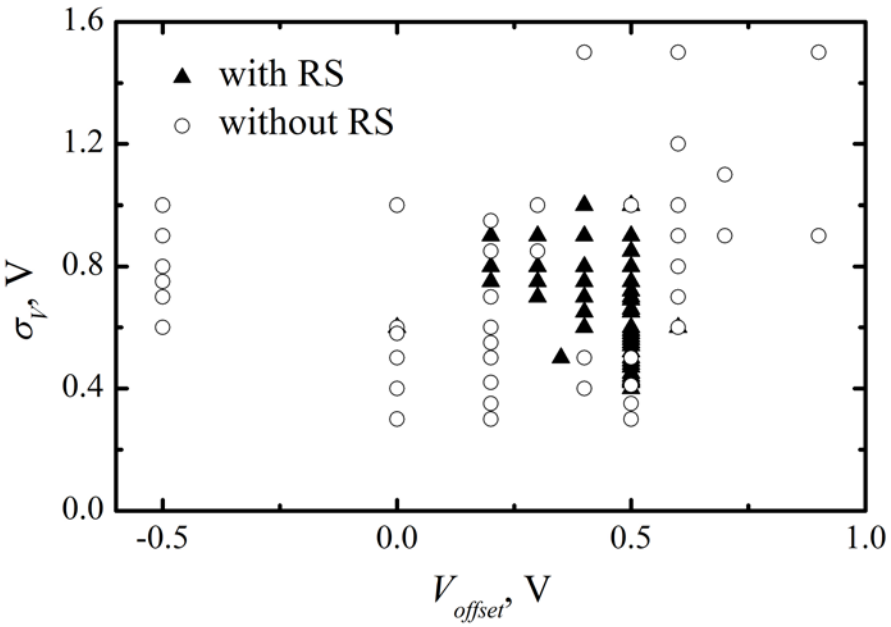

Figure 51. The plot of the parameter space of the experiment: $\sigma_V - V_{offset}$, in which the continuous resistive switching was observed (black triangles) or was not observed (white circles) [A7, A16]

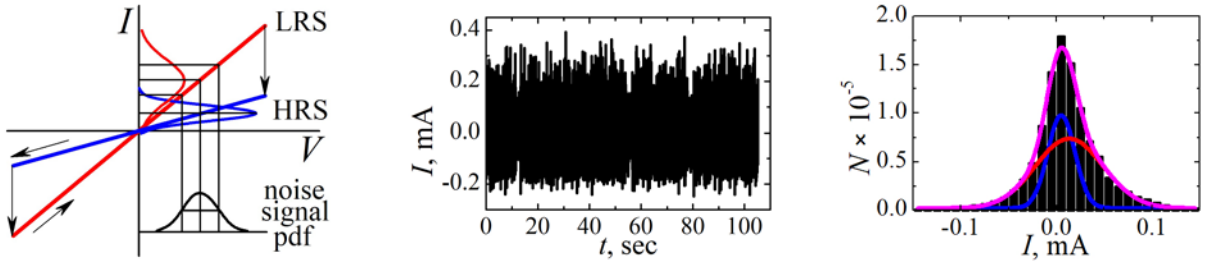

(a) (b) (c)

Figure 52. (a) Analysis of the current response of an ideal memristor to Gaussian white noise; (b) waveform and (c) distribution histogram of the current flowing through the memristive device in the noise-induced resistive switching mode (V_{offset} = 0.5 V and σ_V = 0.85 V), for LRS (red curve), HRS (blue curve) and superposition (purple curve) [A7]

Indeed, the experimental distribution of I in the noise-induced resistive switching mode can be approximated by a superposition of two Gaussian functions as shown in Figure 52c, the distribution histograms of the current flowing through the memristive device in the noise-induced resistive switching mode (V_{offset} = 0.5 V and σ_V = 0.85 V), for LRS (red curve), HRS (blue curve) and superposition of the previous curves (purple curve) are shown. In the case when a non-zero V_{offset} is added to the Gaussian noise signal, the centers of the corresponding Gaussian distributions of I in HRS and

in LRS would be shifted with respect to each other as shown in Figure 52a. This effect explains the asymmetry of the distribution histogram of I shown in Figure 52c. If $V_{offset} = 0$, the centers of both Gaussian distributions will take place at $I = 0$, and the resulting distribution of I will be symmetric.

The state of the memristive device, at a given time t, was characterized by the mean resistance $R(t) = \sigma_V / \sigma_I(t)$, where

$$\sigma_{\mathrm{I}}(t) = \sqrt{\frac{\sum_{i=1}^{M}(I_i - \overline{I_{\mathrm{t}}})^2}{M(M-1)}} \tag{11}$$

is the standard deviation of I calculated for a short time period $T_a << \tau$, $\overline{I}$ is the averaged current over the time period T_a, and M = 100 is the number of points in the time series of the current I, measured within the period T_a.

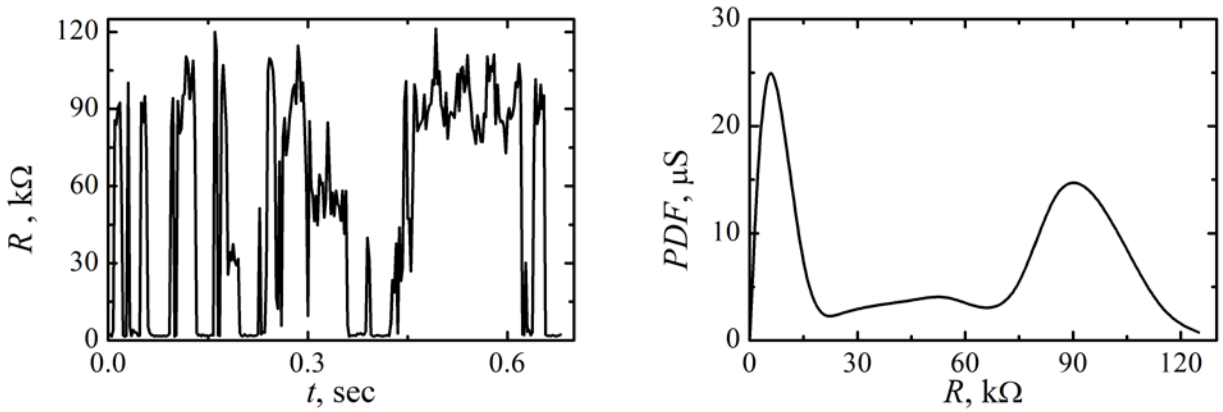

(a) (b)

Figure 53. Waveform (a) and corresponding PDF (b) of resistance R of the memristive device in the noise-induced resistive switching mode. Data obtained under the noise signal with V_{offset} = 0.5 V and σ_V = 0.75 V [A7, A16]

In Figure 53a waveform $R(t)$ calculated, according to the procedure described above, for the memristive device in the noise-induced resistive switching mode are shown. As one can see from Figure 53a, the waveform $R(t)$ demonstrate typical RTS shape. In Figure 53b, the corresponding probability density function (PDF) of R is

presented. The PDF manifest trimodal distributions of R that corresponds to the switching of the memristive device between 3 metastable states under the noise signal.

In Figures 54a and b, the long-time-scale waveforms of I and R of the memristive device in the noise-induced resistive switching mode are shown. During the experiment, the RTS patterns changed. Four examples of different $I(t)$ and $R(t)$ waveform patterns, recorded in selected time windows during the records shown in Figure 54 with corresponding PDFs of R are shown in Figure 55.

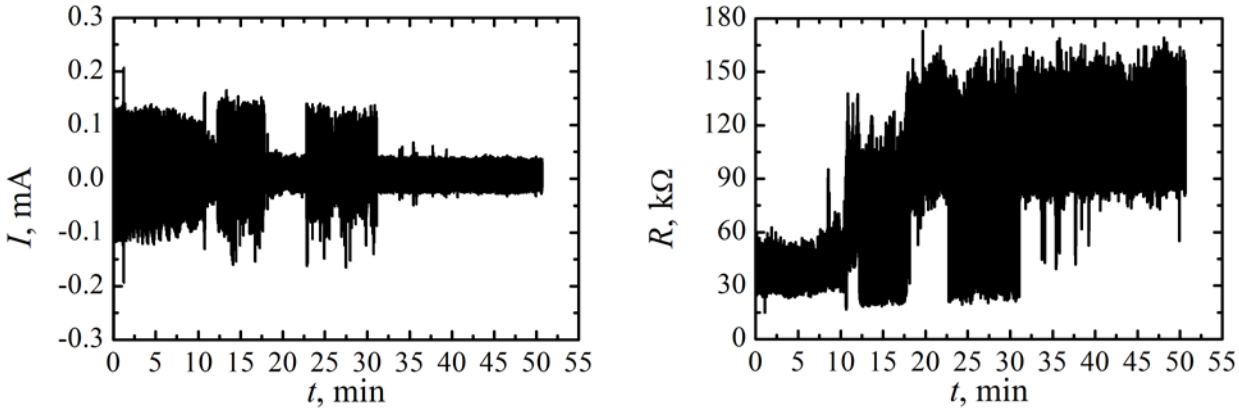

(a) (b)

Figure 54. Long-time-scale waveforms of I (a) and R (b) for the memristive device under noise signal with V_{offset} = 0.35 V and σ_V = 0.5 V [A7, A17]

In the beginning of the waveforms (Figure 54), the averaged (in the long-time-scale $t >> T_a$) resistance of the memristive device increases gradually, and this behavior can be interpreted as the degradation of the memristive device. However, afterwards the noise-induced resistive switching mode restored abruptly. Earlier, it was shown that the resistive switching of a memristor can be restored after complete degradation by applying a suitable electrical signal [155]. The results, presented in Figures 54 and 55, demonstrate the restoring of resistive switching by a noise signal.

The abrupt degradation and restoring of the memristive device have been observed several times during the experiment (see Figure 54). Note that the RTS patterns changed suddenly as well (see, for example, Figure 55b and c). The observed

sudden changes in the behavior of the memristive device during the experiment may be interpreted as a result of sudden change of the electrical properties of the memristive device under the external noise signal. Burning out of the active filament and the wakeup of the next potential filament can be one of such sudden events [156, 157]. Finally, the memristive device froze in HRS, which corresponded to its complete degradation (Figure 55d).

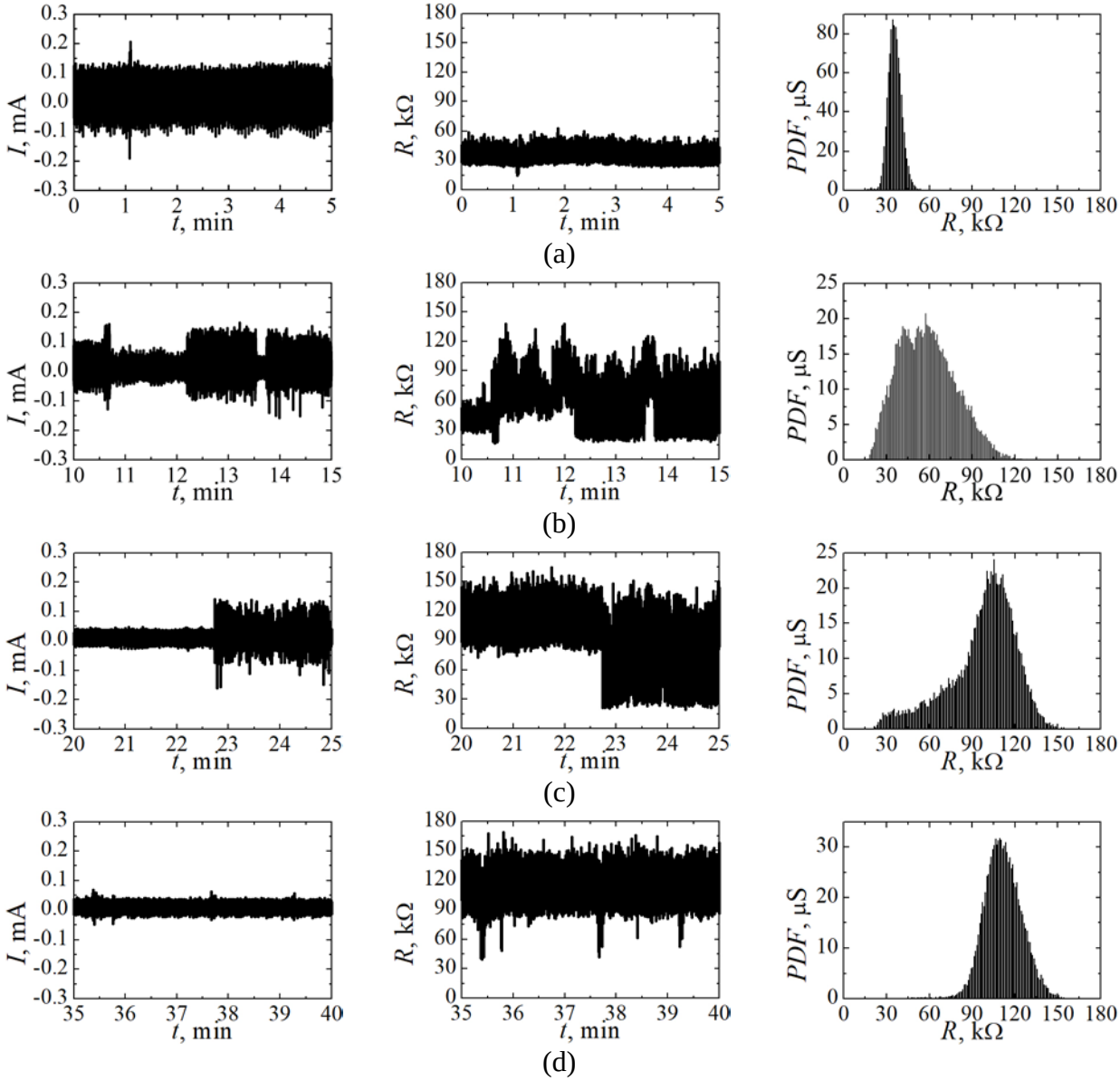

Figure 55. $I(t)$ (left) and $R(t)$ (middle) recorded in different time windows during the experiment: 0 – 5 min (a), 10 – 15 min (b), 20 – 25 min (c), and 35 – 40 min (d), and corresponding PDF of R (right). Data obtained under the noise signal with V_{offset} = 0.35 V and σ_V = 0.5 V [A7, A17]

In Figure 56, the time evolution of the PDF of *R* during the experiment is shown. The evolution of the PDF of *R* reflects the changes of the electrical properties of the memristive device during the experiment under the impact of the noise signal. These observations confirm the multiplicative character of the noise signal on the dynamical behavior of the memristive device.

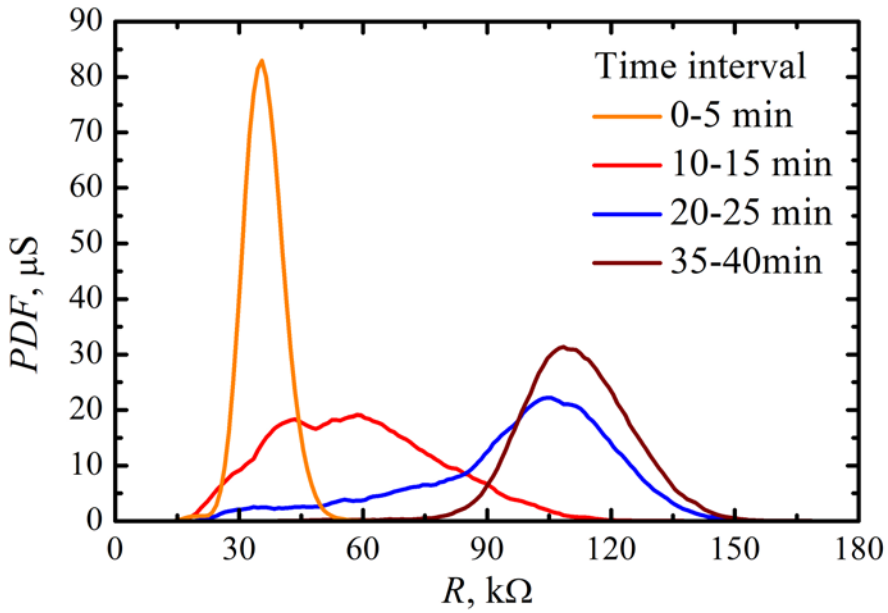

Figure 56. The time evolution of the PDF of *R* during the experiment. Data obtained under the noise signal with V_{offset} = 0.35 V and σ_V = 0.5 V [A7, A17]

Note that in [A18] the results of investigation of the long-time-scale response of another, but the same composition, memristive device to an external noise signal (with the same parameters as in Figures 54-56) are presented. A stochastic switching of the memristive device between resistance states in the RTS mode and the evolution of the PDF of *R* during the experiment was observed.

Stochastic behavior of a memristor can be qualitatively described within the framework of the simplest model using the Langevin equation with additive noise:

$$\frac{dV}{dt} = -\gamma V + \sqrt{D}\xi(t)\,, \tag{12}$$

where $V = R(q)\cdot I$ is the applied voltage (in this case it is a noise signal), γ is the reverse correlation time, $\xi(t)$ is the white noise with amplitude D, and $R(q)$ is the resistance (for an ideal memristor $R(q) = 1+q^2$ [158]), q is the charge, I is the current flowing through the memristor ($I = \mathrm{d}q/\mathrm{d}t$). The values of γ and D were chosen corresponding to experimental noise signal: $\gamma = 1$ and $D = 0.36$. Data obtained under the noise signal with $V_{offset} = 0$.

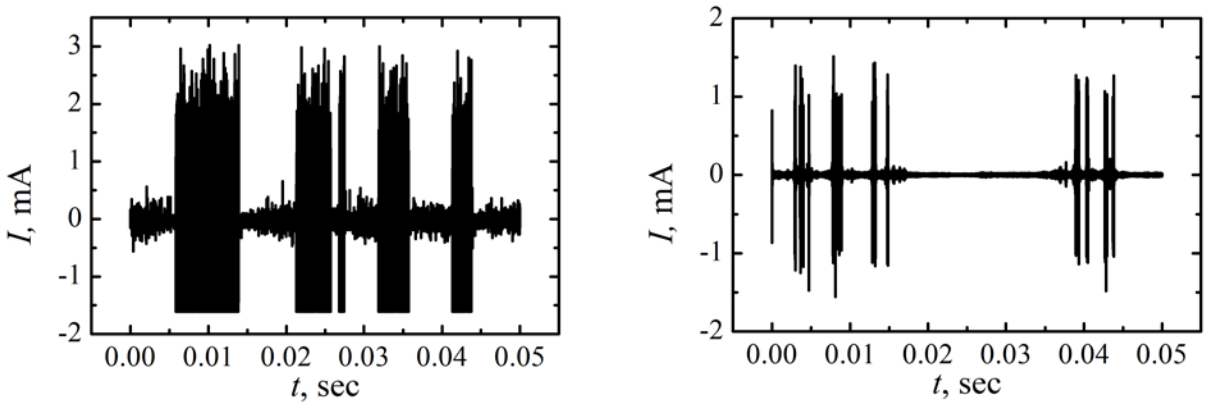

(a) (b)

Figure 57. Waveform of the current flowing through the memristive device. Results of experiment (a) and numerical simulation (b)

The simulated behavior of the memristor is close to the experimental data. However, they have significant differences: absence of dependence of the number of local maxima of the PDF of memristors resistance on the applied noise signal parameters and absence of the changes in PDF over time. For a more realistic description of memristive systems, it is necessary to use more complex models, in particular, the use of multiplicative noise in the equations [159].

Thus, the response of the memristive devices based on YSZ/Ta_2O_5 to a white Gaussian noise signal has been experimentally investigated. A stochastic switching of the memristive devices between resistance states in the random telegraph signal mode has been observed. The restoring of resistive switching by a noise signal has been observed. It was found that switching from LRS to HRS is much faster when a noise signal is applied (these results were obtained for memristive devices based on SiO_x

and are not subject to consideration in this dissertation work; however, the applied approach is fundamentally universal, in particular, for memristors based on various oxides with filamentary mechanism of resistive switching; therefore, the conclusions, obtained in the study of memristive devices based on SiO_x, can be applied to memristive devices based on YSZ; research data available in [160]), that is, the external noise signal stimulates the processes of rearrangement of the atomic configuration of the filament. The approach based on the analysis of the response of multistable nonlinear systems to a noise signal made it possible to determine, that memristors are more complex dynamic system than a system with a simple two-well fixed potential and the influence of noise on the memristors has a multiplicative behavior, that is, the noise perceived by the memristor depends on the state of the system and its electrical properties are influenced by the noise signal. The first conclusion is justified by the presence of more than two peaks in the PDF, and the second – by the changes of the PDF of resistance under the influence of a noise signal. The results of numerical simulation of the description of the memristors behavior by simplest model using the Langevin equation with additive noise are presented. The simulated behavior of the memristor is close to the experimental data.

6.2. Experimental investigations of local stochastic resistive switching of yttria-stabilized zirconia film on a conductive substrate

This section presents the results of the experimental investigations of the local resistive switching in the contact of a CAFM-probe to a nanometer-thick YSZ film on a conductive substrate under a Gaussian noise voltage applied between the probe and the substrate.

Sample preparation and method of investigation are described in Chapter 2. Figure 58 shows the typical cyclic *I*–*V* curve of the CAFM-probe/YSZ contact (I_t is the CAFM-probe current and V_g is the bias voltage).

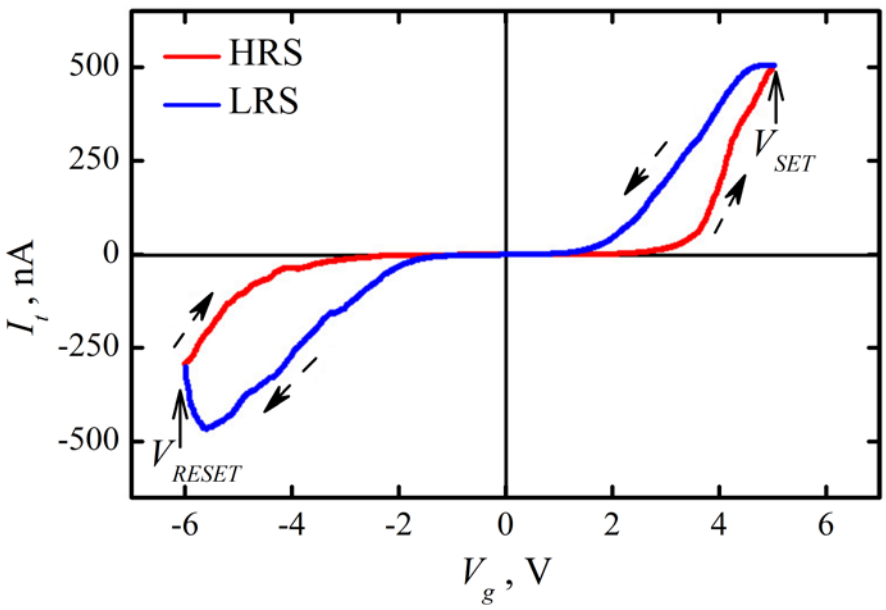

Figure 58. Typical *I–V* curve of the CAFM-probe/sample contact. Arrows shows the direction of the voltage sweep [A8]

A pronounced hysteresis typical for the bipolar resistive switching has been observed. One can note different values of $V_{SET} \approx 5$ V and $V_{RESET} \approx$ -6 V owing to the asymmetry of the virtual memristor structure: the YSZ layer contacted with chemically active TiN conductive layer from the bottom side and to the chemically inert diamond-like coating of the CAFM-probe at the surface.

In this investigation, the waveforms of I_t were recorded subject to the parameters of the input noise signal σ_V and V_{offset}. In Figure 59 are shown waveforms of I_t, recorded at V_{offset} = -1 V and different values of σ_V (corresponding to different noise magnitude), and the respective PDFs. At σ_V = 0.3 V, for values of V_g within the linear region in the *I–V* curve of the virtual memristor, the distribution of I_t had an almost Gaussian form as that of the input voltage V_g (Figure 59a). In this case, the virtual memristor acted as a linear resistor (in the HRS) and the distribution of I_t simply reflect that of V_g. Slight deviation of I_t from the Gaussian shape can be attributed to the nonlinearity of the *I–V* curve of the virtual memristor. In the presence of the digitally synthesized external noise signal with σ_V = 0.9 V, the virtual memristor switches between HRS and LRS randomly as a RTS (Figure 59b). Such a

behavior is typical for bistable systems. The noise-induced resistive switching was observed in the range of V_{offset} from -1 V to -0.5 V. Note that this range of V_{offset} corresponds to the mean value of V_{SET} and V_{RESET} in the cyclic I–V curve of the CAFM-probe/sample contact (Figure 58).

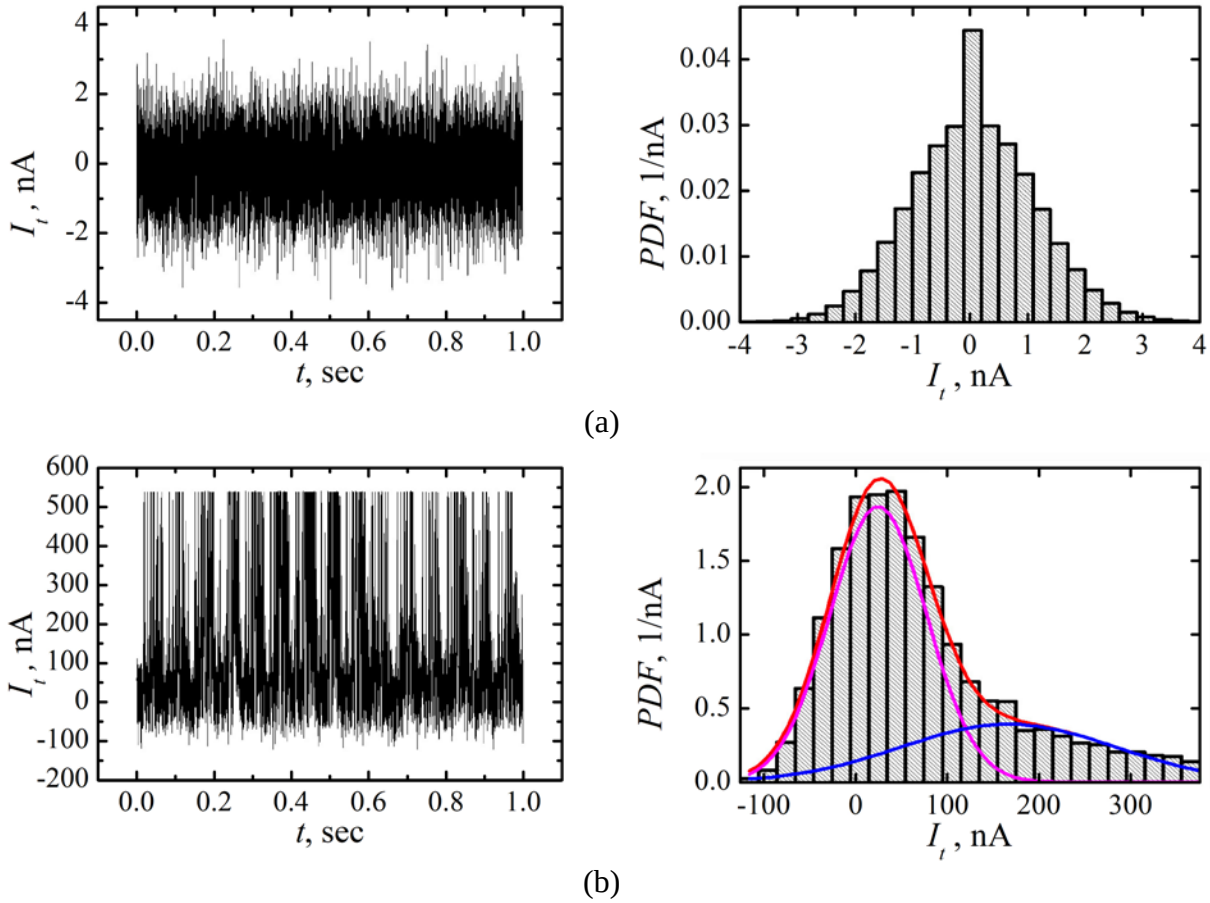

Figure 59. The waveforms (left) and respective PDFs (right) of the CAFM-probe current I_t, obtained under noise signal with V_{offset} = -1 V and σ_V, V: 0.3 (a) and 0.9 (b) [A8, A19]

The current distributions in this case can be interpreted in the framework of the analysis of the influence of a random voltage with a Gaussian distribution on an ideal memristor, as was done in Section 6.1 (see Figure 52a). Indeed, the experimental PDF of I_t can be approximated by a superposition of two Gaussian functions as shown in Figure 59b, where the PDFs for LRS (purple curve), HRS (blue curve) and superposition of the previous curves (red curve) are shown. In the case when a non-zero V_{offset} was added to the Gaussian noise signal, the centers of the corresponding

Gaussian distributions of I_t in HRS and in LRS were shifted with respect to each other. This effect explains the asymmetry of the PDF of I_t shown in Figure 59b. If V_{offset} = 0, the centers of both Gaussian distributions will take place at I_t = 0, and the resulting distribution of I_t will be symmetric.

The state of the virtual memristor, at a given time t, was characterized by the mean resistance $R(t)$, as in Section 6.1. As seen in Figure 60a, $R(t)$ changes in time as RTS: the virtual memristor switches between two metastable states, which are reflected in the PDF of R, plotted in Figure 60b, where two peaks, corresponding to HRS and LRS, were observed.

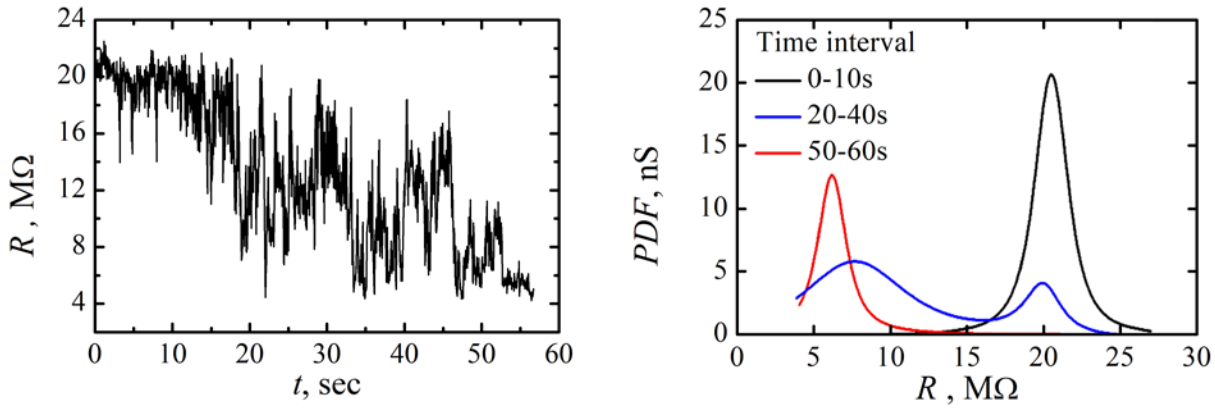

(a) (b)

Figure 60. Waveform (a) and PDF (b) of the virtual memristor resistance R in the noise-induced resistive switching mode. Data obtained under the noise signal with V_{offset} = -1 V and σ_V = 0.9 V [A8, A19]

Note, that CAFM method allows investigating local resistive switching. In other words, using this method, it is possible to consider the life of only one filament. In contrast to studies on micrometer-sized electrodes, where after burning out the current filament, a new one with new resistance characteristics is formed. Therefore, the peculiarities obtained for micrometer-sized electrodes can be different from ones, obtained for nanometer-sized electrodes.

Thus, this section shows the results of the experimental investigations of the response of a CAFM-probe contact to an YSZ film on a conductive substrate, a

virtual memristor, to an external Gaussian white noise signal. A stochastic switching of the virtual memristor between two metastable resistance states in the RTS mode under the noise signal and constant offset has been observed.

6.3. Main results of Chapter 6

Thus, this chapter shows the response of the memristive devices based on YSZ/Ta_2O_5 to a white Gaussian noise signal. A stochastic switching of the memristive devices between resistance states in the random telegraph signal mode has been observed. The results indicate that memristors are more complex dynamic system than a system with a simple two-well fixed potential and the influence of noise on the memristors has a multiplicative behavior.

Experimental investigations of the response of a CAFM-probe contact to an YSZ film on a conductive substrate, a virtual memristor, to an external Gaussian white noise signal has been observed. A stochastic switching of the virtual memristor between two metastable resistance states in the random telegraph signal mode under the noise signal has been observed.

The obtained results highlight the applicability of the physical statistical formalism usually applied to the description of the behavior of nonlinear multistable systems to the description of the memristors. Also, it should be noted that the approach based on the analysis of the response of a memristor to an artificial noise signal is applicable not only to the oxide-based memristor utilizing the filamentary resistive switching mechanism, but also to the memristors based on other resistive switching types, such as conducting bridge.

CHAPTER 7. Stochastic resonance in memristive systems

Despite significant progress in the physics and technology of memristive devices, their widespread practical application is constrained by insufficient stability (high variability) of resistive switching parameters, as well as their degradation during operation [89, 161]. A combination of diverse transport phenomena under the influence of concentration gradients, electric field and temperature, as well as redox reactions are responsible for the filaments reconstruction even in the simplest metal-oxide devices. These physical-chemical phenomena occur on different time scales and conditions far from equilibrium; therefore, the resistive switching process has a pronounced stochastic nature. Traditional approaches to increase the stability of resistive switching parameters include engineering memristive devices by selecting the optimal stacks of oxide and electrode materials [8] and the use of multilayer structures [100, 162], as well as special programming techniques [163, 164]. These approaches are quite effective for demonstration purposes in the implementation of small-sized prototypes of computing systems [152, 165]. However the incurring technology and circuit-level overheads call into question the prospects for their further scaling. Relatively new approaches to control the dynamic response of memristors based on the use of attractors [166], bifurcations [167] and deterministic chaos [168] have not yet been implemented experimentally. The main reason for this is that a memristive device is not a deterministic dynamical system, but a complex stochastic system, the description of which requires taking into account noise and nonlinear fluctuation phenomena inherent in real systems with a discrete structure.

Recent studies have convincingly shown that, in nonlinear systems, the effect of noise can induce new, more ordered regimes that lead to the formation of more regular structures, increase the degree of coherence, cause an increase in the gain and signal-to-noise ratio (SNR) at the output of the system, etc. Specifically, in such systems, the well-known stochastic resonance phenomenon [121-124] can occur, where noise plays a constructive role [125-130].

The stochastic resonance observed in various nonlinear systems under the simultaneous perturbation by noise and a periodic signal (experimentally, for example, in a tunnel diode [169], and theoretically, for example, in a model of two competing species [170]; see also [171]). Under some conditions, an increase in the intensity of internal or external noise leads to an increased response to a periodic perturbation. In this case, the amplitude of the system response is described by a function of the resonant type, in which the argument is the noise intensity. It should be noted the works on noise-enhanced stability (for example, experimental [172] and theoretical ones [173-175]), in which the effect of noise is considered from the point of view of stabilizing the changing state of the system, that is, increasing the lifetime of the system in this state.

To detect the stochastic resonance, it is necessary to have threshold-type nonlinearity, periodic perturbation, and a source of white or colored noise in the system under study. These conditions can be realized for metal-oxide memristive devices. The filament-type resistive switching process is nonlinear and has pronounced threshold properties. The standard endurance test is carried out by applying periodic bipolar pulse trains that meet the requirements of a coherent driving signal. The imposition of noise on such a signal at its sub-threshold amplitude can lead to the stabilization of resistive switching parameters and many other useful effects associated with the constructive role of noise (for example, resonant activation [176]).

Theoretical work [139] was the first to use an approach, based on the use of the stochastic resonance phenomenon, to stabilize resistive switching itself, that is, its presence. The authors concluded that the superposition of noise with optimal intensity on the periodic driving field (which in itself did not lead to switching) led to an increase in the hysteresis loop of the current-voltage characteristics (*I*–*V* curves). In addition, it was shown that the dependence of the SNR on the noise intensity has a maximum. In a mainly experimental work [141], the white Gaussian noise of adjustable intensity was superimposed on the rectangular switching signal. An

increase in the temporal stability of the memristor was noted in the case of switching with superimposed noise. The effect was most pronounced at certain noise intensity, indicating the possibility of the stochastic resonance manifestation in memristive devices. Preliminary experimental data on the influence of external noise on the resistive switching driven by a sinusoidal signal have been recently reported [177], and the authors continue to explore some positive applied aspects of this effect [178]. However, up to date there is no information in the literature on deeper experimental studies of the stochastic resonance phenomenon in memristive devices both in terms of resistive switching parameters improvement and basic stochastic resonance regularities.

Section 7.1 presents the results of the experimental investigations of stochastic resonance phenomenon for memristive devices based on yttria-stabilized zirconia (YSZ)/Ta_2O_5. Section 7.2 summarizes the results obtained in Chapter 7.

7.1. Stochastic resonance in memristive devices based on yttria-stabilized zirconia

This section presents the results of the experimental investigations of stochastic resonance phenomenon for memristive devices based on YSZ/Ta_2O_5. Sample preparation and method of investigation are described in Chapter 2. Memristive devices based on YSZ/Ta_2O_5 have been selected as sample objects for experimental studies because of the longer duration of such devices [100].

A classical experiment to confirm the phenomenon of stochastic resonance [122] consists in the applying of a periodic driving signal to a nonlinear system with the amplitude that is insufficient to cause a regular response of the system to the periodic signal. As the noise intensity added to the driving signal increases, the system response becomes regular and, when the optimum noise intensity is reached, the maximum SNR is realized. With a further increase in the

noise intensity, the system behavior is no longer determined by the driving periodic signal, but follows the dynamics of noise effect.

In Figure 49 the typical cyclic *I*–*V* curves of the investigated memristive devices is shown. To carry out experimental investigations of the stochastic resonance phenomenon sinusoidal voltage signal was superimposed with white Gaussian noise (see Chapter 2). At the beginning of the study, the value of the sub-threshold level of the periodic driving signal was found by investigation of the response of memristive device to sinusoidal voltage signal with period of 0.1 s and amplitude in the range from 0.5 to 2.0 V. At amplitudes lower than 0.8 V, the resistive switching was not revealed, and, at amplitudes greater than 1.5 V, a reproducible switching between the extreme resistive states was observed. It should be noted here that as a result of the multilevel nature of resistive switching, the so-called «memory window», that is, the presence of differences between two resistive states, can be achieved not only with V_{SET} and V_{RESET} (see Figure 49), that is, extreme resistive states, but also when applying $|V| < V_{RESET}, |V_{SET}|$ (see for example [55]). Thus, amplitude of 1 V was chosen as amplitude of the periodic driving signal. Typical input voltage signals are shown in Figure 61 and consist of a sinusoidal signal (amplitude of 1 V) with superimposed white Gaussian noise with different intensities.

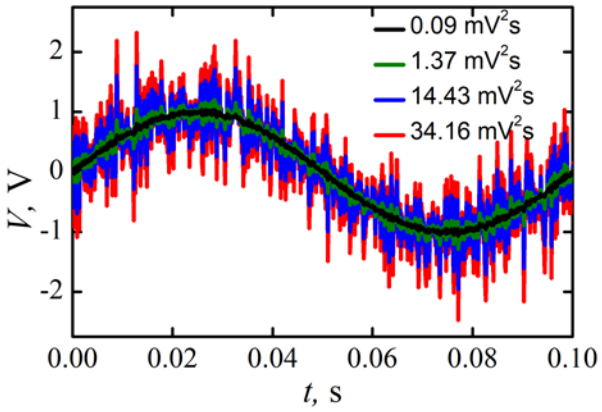

Figure 61. Typical waveform of input voltage signal: a sinusoidal signal (amplitude of 1 V) with superimposed noise with different intensities [A9]

Note that after each application of an input signal with different noise intensities, the *I–V* curves were measured in order to control the presence of resistive switching and confirm the reproducibility of their parameters. Also, before each application of an input signal with different noise intensities, the memristive device was switched to the initial high resistance state (HRS).

The response of the memristive device to the input signal with different noise intensities are shown in Figure 62 (the right and left panels differ only in time scale). The current jumps corresponding to typical SET (switching from HRS to low resistance state (LRS)) and RESET (from LRS to HRS) transitions during one sinusoidal period are marked by arrows in Figure 62b. On both time scales, it is seen that the switching is irregular. This is due to the fact that not every negative half-cycle of a sinusoidal signal leads to a complete SET process, and not every positive half-cycle ends in a complete RESET transition. With an increase in the noise intensity, the variation of resistive states after the SET and RESET transitions decreases significantly (Figure 62b, d and f).

The corresponding *I–V* curves are shown in Figure 63. *I–V* curves were obtained from the waveforms of current (Figure 62, left panel) and corresponding input voltage signal, and then averaged. Note, that memristive devices did not demonstrate resistive switching without applying noise. The addition of low-intensity noise (0.09 $mV^2 \cdot s$) resulted in resistive switching, as shown in Figure 63a as a small hysteresis in the *I–V* curves. Further increases in noise intensity led to an increase in hysteresis (Figure 63b and c). With a further increase in the noise intensity, the hysteresis on the *I–V* curves decreased significantly (Figure 63d). Note that in the case of high noise intensities, resistive switching occurs even at amplitudes of the periodic driving signal below 1 V.

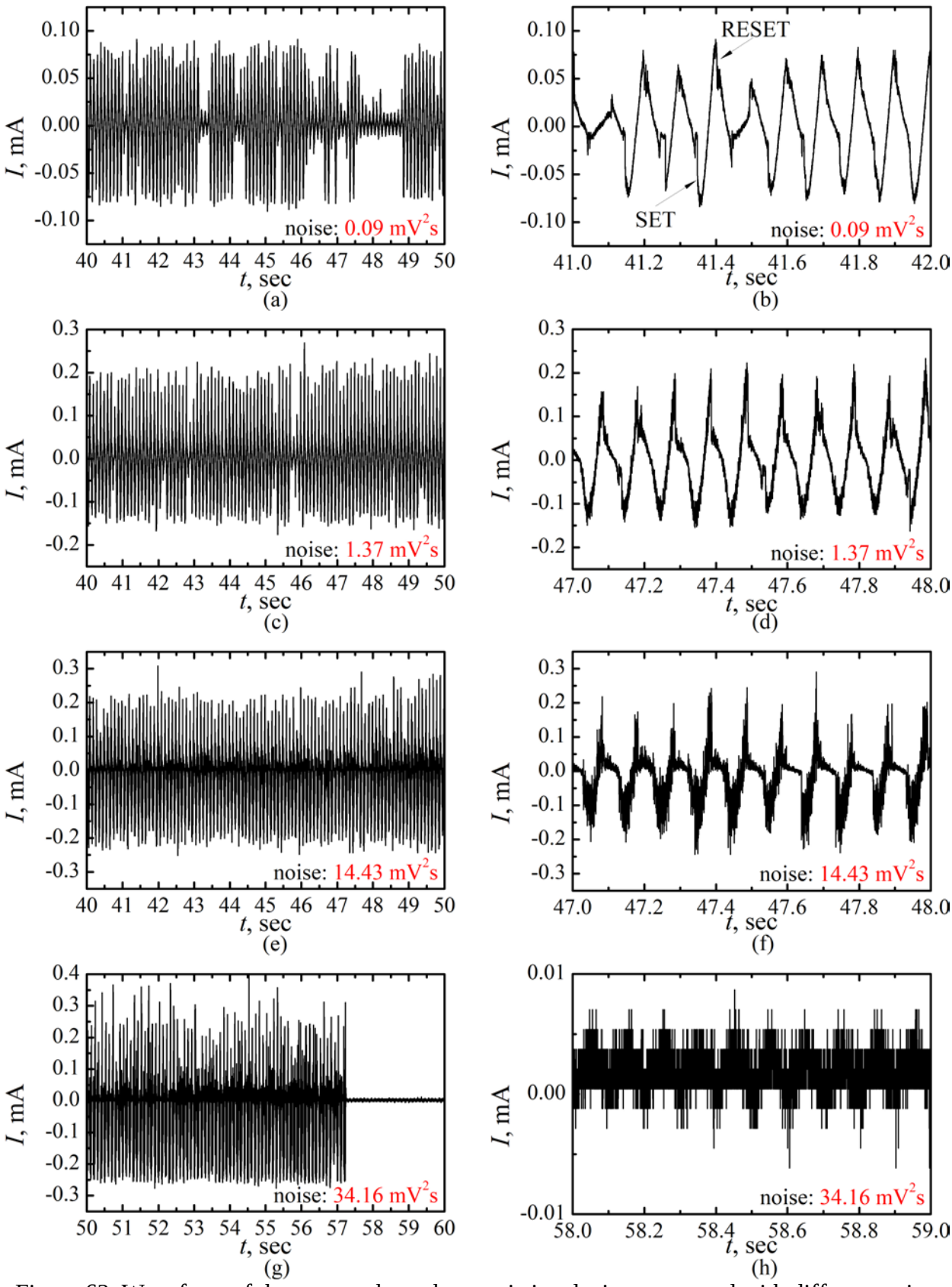

Figure 62. Waveform of the current through memristive device, measured with different noise intensities (the right and left panels differ only in time scale) [A9]

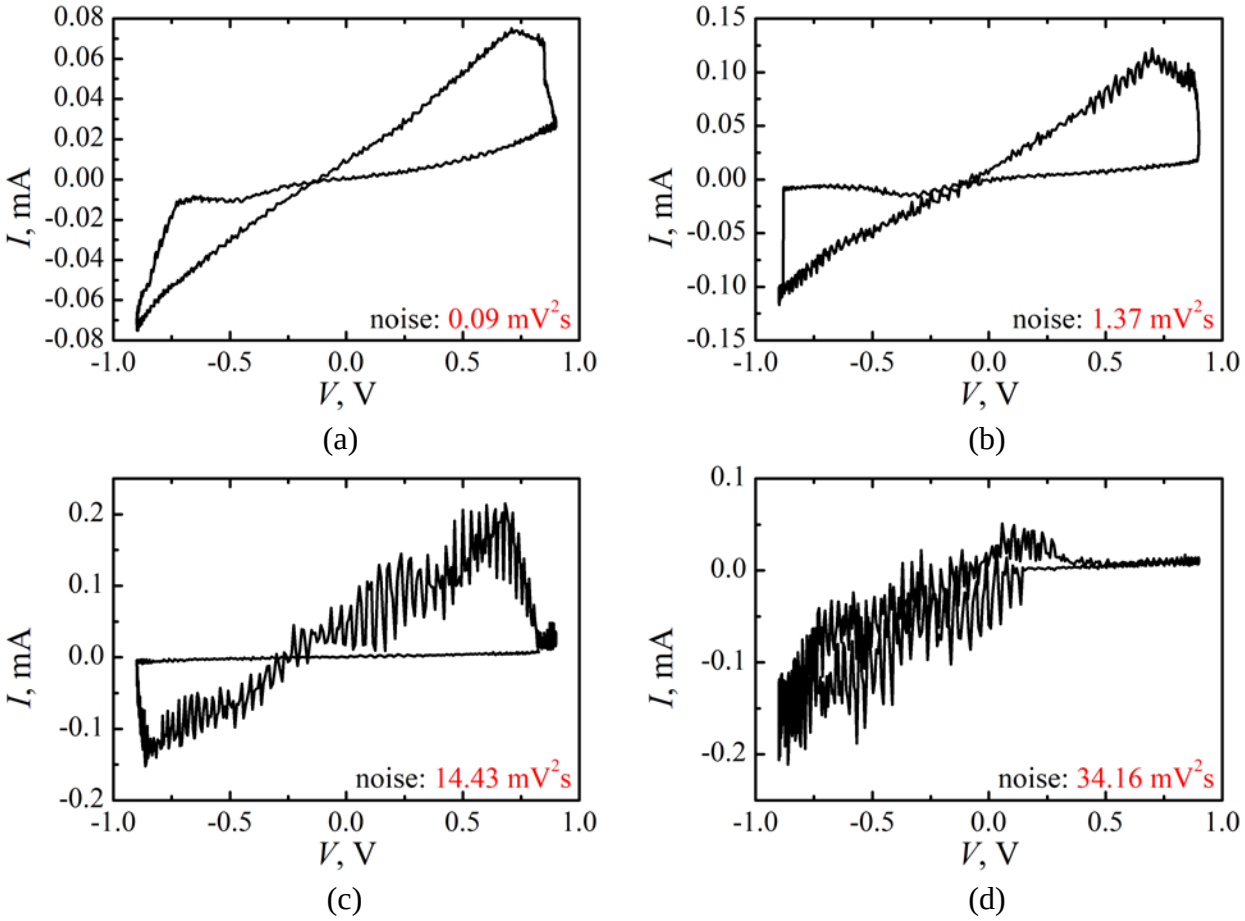

Figure 63. *I–V* curves of the memristive device obtained at different noise intensities [A9]

When the intensity of noise is increased, the following basic regularities are established. First, with increasing noise intensity, the resistive switching becomes regular even for the sub-threshold driving signal, the switching completeness (degree of completion of the SET and RESET processes) increase, which leads to an increase in the ratio of currents (resistances). By analogy with the early theoretical and experimental works [139, 141], we can regard this relation as a useful signal in the memristor response and as a measure of the switching quality. Second, increasing the noise intensity increases the switching stability, which is manifested in a significant decrease in the variation of resistive states after SET and RESET transitions. Third, exceeding the optimum noise intensity leads to a deterioration of the switching parameters.

By using experimental *I–V* curves (which are partially shown in Figure 63), the average values of current through memristor were determined in resistive states at the

V = 0.5 V. Since the current is limited to a compliance value of 300 μA during the SET transition, the current variation in the HRS after RESET switching was taken as a measure of switching stability. Both of these quantitative characteristics are presented in Figure 64, depending on the noise intensity. From Figure 64 it follows that the current ratio depends non-monotonically on the noise intensity and has a pronounced maximum for a noise intensity of 14.43 $mV^2 \cdot s$. An additional maximum at 1.37 $mV^2 \cdot s$ is noteworthy and most likely corresponds to the optimum noise intensity to stabilize the SET transition. The variation of current after switching to HRS decreases with increasing noise intensity and reaches saturation when the optimum noise intensity values are achieved. The small variation values for noise intensities below 1.37 $mV^2 \cdot s$ are associated with the incomplete SET process and lower current absolute values in the LRS. Thus, the revealed resistive switching regularities are in qualitative agreement with the classical stochastic resonance phenomenon.

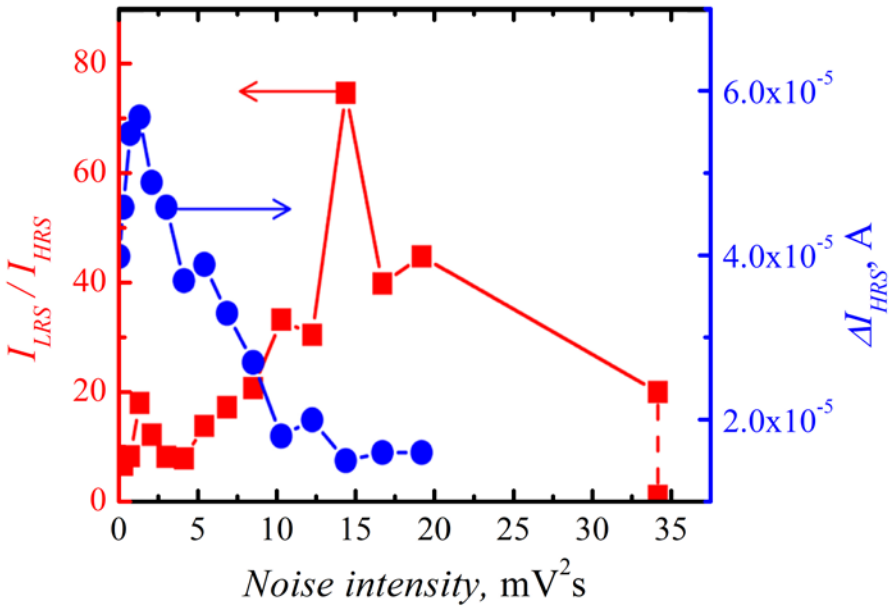

Figure 64. Dependences of the ratio of the current in LRS and HRS (I_{LRS} / I_{HRS}) and variation of current after switching to HRS (ΔI_{HRS}) on noise intensity [A9]

The most informative parameter of resistive switching is the value of memristance R_m. The power spectra of R_m for different noise intensities were calculated by the fast Fourier transform technique. The typical power spectrum of R_m is shown in Figure 65. The dependence of the SNR on the intensity of the superimposed noise was obtained (Figure 66) from the spectrum of R_m (at a fundamental frequency of 10 Hz). At very low noise intensity, the most common SNR dependence is observed: the SNR decreases with increasing external noise. Then the SNR reaches a minimum and begins to grow (stochastic resonance is often defined as a noise-induced rise of the SNR in a nonlinear system). The maximum SNR is reached at 10 – 12 $mV^2 \cdot s$, and then the SNR decreases again. This behavior is very similar to the classical case of stochastic resonance for symmetric bistable or threshold systems with additive noise [171] as well as to the more sophisticated asymmetric cases with multiplicative and additive noise sources [179].

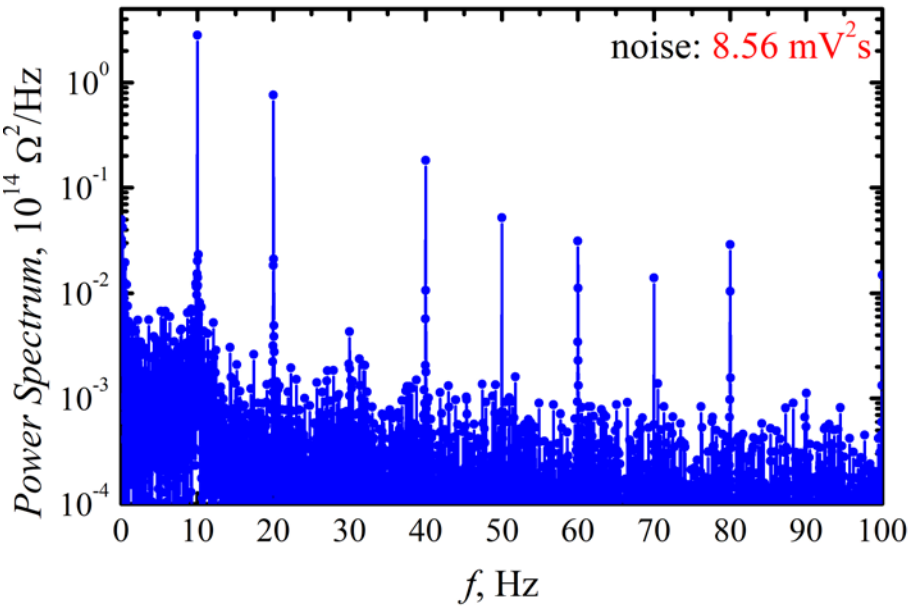

Figure 65. Typical power spectrum of memristance obtained for noise intensity of 8.56 $mV^2 \cdot s$ [A9]

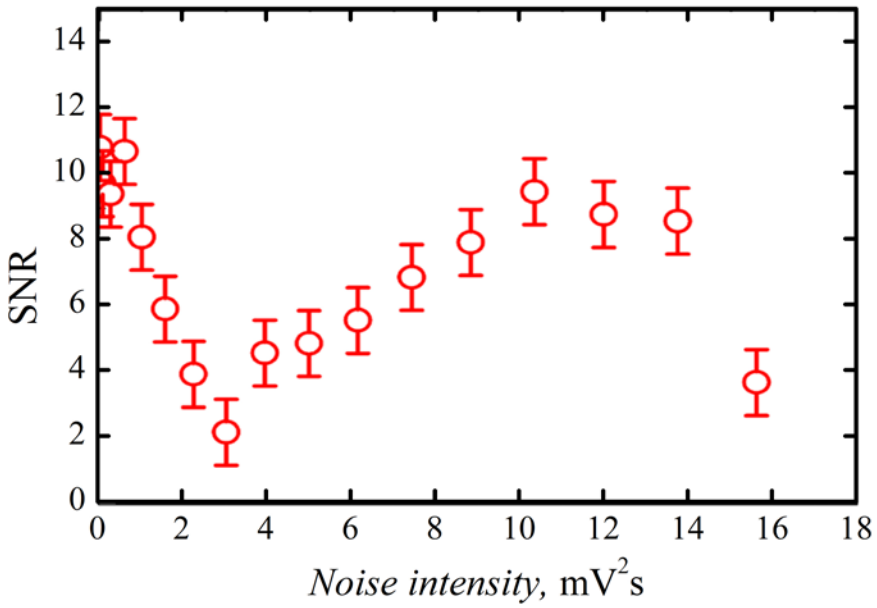

Figure 66. Dependence of the signal-to-noise ratio of memristance on the noise intensity, obtained experimentally [A9]

Thus, this section shows the results of the experimental investigations of the main features of resistive switching parameters variation under the application of white Gaussian noise added to the driving voltage. Applying of a periodic driving signal with amplitude of 1 V with superimposed white Gaussian noise provides the appearance of regular resistive switching, which is observed as hysteresis loop in *I*–*V* curves. The size of hysteresis loop initially grows with increasing in noise intensity and then decreases disappearing for large enough noise intensity. The SNR obtained for the fundamental frequency in the spectrum of memristance changes with noise non-monotonically. The SNR increases with increasing in noise intensity, reaches a maximum value, and then decreases. The last can be considered as a manifestation of stochastic resonance and the constructive role of noise in memristive systems.

7.2. Main results of Chapter 7

This chapter shows the response of the memristive devices based on YSZ/Ta_2O_5 to a periodic driving signal with amplitude of 1 V with superimposed

white Gaussian noise with different intensities. At zero noise intensity, no resistive switching was found. A gradual increase in the noise intensity led first to the appearance of resistive switching, namely, the formation of a hysteresis loop, an increase in the hysteresis loop, and, then, to its disappearance, as well as to the disappearance of resistive switching. At the same time, a non-monotonic dependence of the ratio of currents in LRS and HRS on the noise intensity was observed. The optimal value of the noise intensity, at which a maximum appears on this dependence, was found. Thus, one can conclude that resistive switching regularities are in qualitative agreement with the classical stochastic resonance phenomenon. The dependence of the SNR of memristance on the intensity of the superimposed noise was obtained. It was found that at very low noise intensity, the most common SNR dependence is observed: the SNR decreases with increasing external noise. Then the SNR reaches a minimum, begins to grow and reaches a maximum, and then the SNR decreases again. The last can be considered as a manifestation of stochastic resonance and the constructive role of noise in memristive systems.

Conclusions

Using a set of low-temperature methods for investigations of the ion migration polarization of an insulator of memristive structures, the value of activation energy of migration of oxygen ions in YSZ was obtained (0.50 – 0.55 eV in the temperature range T = 300 – 500 K).

Nonlinearity and hysteresis of C–V and G–V curves of memristive MIM-structures based on YSZ, nanostructured by an array of Au NPs, were found. The effect was associated with the accumulation of charge in the NPs. The possibility of charge accumulation in Au NPs has been experimentally confirmed by an independent method of KPFM.

It was found that the mechanism of current transfer in the MIM-structures based on YSZ is space-charge-limited current. The conduction in LRS and HRS was of an activation behavior. With an increase in value of current compliance, the activation energy of the conduction in the LRS decreased and the behavior of the conduction tended to be metallic.

It was established that change in the dielectric loss tangent in memristive MIM-structures based on YSZ during resistive switching result from the formation (rupture) of filaments in YSZ film.

It was found that investigated structures demonstrates the effect of resistive switching at high temperatures (up to 125 °C), which indicates that these structures are promising for creating elements of resistive memory with increased temperature sustainability.

Memristive devices were prepared on the basis of the investigated MIM-structures. Devices demonstrated up to 10^6 switches, switching time ~ 70 ns, operating temperature up to 125 °C and the ratio of resistances in HRS and LRS > 10.

The effect of resistive switching, stimulated by optical radiation, of MIS-structures has been observed. This effect is associated with the redistribution of the voltage between the insulator and the semiconductor, caused by the appearance of

photo-electromotive-force at the semiconductor/insulator barrier due to interband optical absorption in the *n*-Si substrate. The influence of optical radiation was most pronounced in MIS-structures, in which passivating Sb layers were embedded at the YSZ/SiO_2 interface.

A stochastic switching of the memristive devices based on YSZ/Ta_2O_5 between resistance states in the random telegraph signal mode has been observed. The restoring of resistive switching by a noise signal has been observed. It was found that switching from LRS to HRS is much faster when a noise signal is applied, that is, the external noise signal stimulates the processes of rearrangement of the atomic configuration of the filament. The approach based on the analysis of the response of multistable nonlinear systems to a noise signal made it possible to determine, that memristors are more complex dynamic system than a system with a simple two-well fixed potential and the influence of noise on the memristors has a multiplicative behavior, that is, the noise perceived by the memristor depends on the state of the system and its electrical properties are influenced by the noise signal. The first conclusion is justified by the presence of more than two peaks in the probability density function curves, and the second – by the changes of the probability density function of resistance under the influence of a noise signal.

The response of the memristive devices based on YSZ/Ta_2O_5 to a periodic driving signal with superimposed white Gaussian noise with different intensities was investigated. Dependence of the ratio of currents in LRS and HRS on the noise intensity was obtained. The optimal value of the noise intensity, at which a maximum appears on this dependence, was found (14.43 $mV^2 \cdot s$). The variation of current after switching to HRS (taken as a measure of switching stability) reaches saturation when the optimal value of the noise intensity is achieved. Thus, one can conclude that resistive switching regularities are in qualitative agreement with the classical stochastic resonance phenomenon. The dependence of the SNR of memristance on the intensity of the superimposed noise was obtained. It was found that at very low noise intensity, the most common SNR dependence is observed: the SNR decreases

with increasing external noise. Then the SNR reaches a minimum, begins to grow and reaches a maximum (at 10 – 12 $mV^2 \cdot s$), and then the SNR decreases again. The last can be considered as a manifestation of stochastic resonance and the constructive role of noise in memristive systems.

List of publications on the topic of the dissertation work

[A1] Resistive switching in the Au/Zr/ZrO_2–Y_2O_3/TiN/Ti memristive devices deposited by magnetron sputtering / O.N. Gorshkov, A.N. Mikhaylov, A.P. Kasatkin, S.V. Tikhov, D.O. Filatov, D.A. Pavlov, A.I. Belov, M.N. Koryazhkina, A.I. Bobrov, N.V. Malekhonova, E.G. Gryaznov, I.N. Antonov, M.E. Shenina // Journal of Physics: Conference Series. 2016. V. 741. P. 012174.

[A2] Capacitors with nonlinear characteristics based on stabilized zirconia with built-in gold nanoparticles / S.V. Tikhov, O.N. Gorshkov, D.A. Pavlov, I.N. Antonov, A.I. Bobrov, A.P. Kasatkin, M.N. Koryazhkina, M.E. Shenina // Technical Physics Letters. 2014. V. 40 (5). Pp. 369-371.

[A3] Ion migration polarization in the yttria stabilized zirconia based metal-oxide-metal and metal-oxide-semiconductor stacks for resistive memory / S.V. Tikhov, O.N. Gorshkov, I.N. Antonov, A.I. Morozov, M.N. Koryazhkina, D.O. Filatov // Advances in Materials Science and Engineering. 2018. V. 2018. P. 2028491.

[A4] Study of local charge accumulation in ZrO_2(Y) films with Au nanoparticles by Kelvin Probe Force Microscopy / M.N. Koryazhkina, D.O. Filatov, I.N. Antonov, M.A. Ryabova, M.S. Dunaevskii // Journal of Surface Investigation: X-ray, Synchrotron and Neutron Techniques. 2019. V. 13. PP. 30-35.

[A5] Investigation of local charge accumulation in yttria stabilized zirconia films with Au nanoparticles by Scanning Kelvin Probe Microscopy / D.O. Filatov, O.N. Gorshkov, A.N. Mikhaylov, D.S. Korolev, M.N. Koriazhkina, M.A. Ryabova, I.N. Antonov, M.E. Shenina, D.A. Pavlov, M.S. Dunaevskiy // Journal of Physics: Conference Series. 2018. V. 1124. P. 081028.

[A6] Light-induced resistive switching in silicon-based metal-insulator-semiconductor structures / S.V. Tikhov, O.N. Gorshkov, M.N. Koryazhkina, I.N. Antonov, A.P. Kasatkin // Technical Physics Letters. 2016. V. 42 (5). Pp. 536-538.

[A7] Noise-induced resistive switching in a memristor based on $ZrO_2(Y)/Ta_2O_5$ stack / D.O. Filatov, D.V. Vrzheshch, O.V. Tabakov, A.S. Novikov, A.I. Belov, I.N. Antonov, V.V. Sharkov, M.N. Koryazhkina, A.N. Mikhaylov, O.N. Gorshkov, A.A. Dubkov, A. Carollo, B. Spagnolo // Journal of Statistical Mechanics: Theory and Experiment. 2019. V. 2019. P. 124026.

[A8] Experimental investigations of local stochastic resistive switching in yttria stabilized zirconia film on a conductive substrate / D.O. Filatov, A.S. Novikov, V.N. Baranova, D.A. Antonov, A.V. Kruglov, I.N. Antonov, A.V. Zdoroveishchev, M.N. Koryazhkina, O.N. Gorshkov, A.A. Dubkov, A. Carollo, B. Spagnolo // Journal of Statistical Mechanics: Theory and Experiment. 2020. V. 2020. P. 024005.

[A9] Stochastic resonance in metal-oxide memristive device / A.N. Mikhaylov, D.V. Guseinov, A.I. Belov, D.S. Korolev, V.A. Shishmakova, M.N. Koryazhkina, D.O. Filatov, O.N. Gorshkov, D. Maldonado, F.J. Alonso, J.B. Roldán, A.V. Krichigin, N.V. Agudov, A.A. Dubkov, B. Spagnolo // Submitted to Chaos Solitons Fractals. 2020.

[A10] Resistive switching in metal-oxide memristive materials and devices / A.N. Mikhaylov, M.N. Koryazhkina, D.S. Korolev, A.I. Belov, E.V. Okulich, V.I. Okulich, I.N. Antonov, R.A. Shuisky, D.V. Guseinov, K.V. Sidorenko, M.E. Shenina, E.G. Gryaznov, S.V. Tikhov, D.O. Filatov, D.A. Pavlov, D.I. Tetelbaum, O.N. Gorshkov, A.V. Emelyanov, K.E. Nikiruy, V.V. Rylkov, V.A. Demin, and B. Spagnolo // Metal oxides for Non-Volatile Memories: Materials, Technology and Applications. – P. Dimitrakis, I. Valov, S. Tappertzhofen (Eds.) – Cambridge: Elsevier, 2021 [Accepted].

[A11] Resistive switching in the $Au/Zr/ZrO_2–Y_2O_3/TiN$ nanostacks / O.N. Gorshkov, A.N. Mikhailov, A.I. Belov, M.N. Koryazhkina, N.V. Malekhonova, I.N. Antonov, M.E. Shenina // Proceedings of 3rd International School and Conference «Saint Petersburg OPEN 2016» (Saint Petersburg). 2016. Pp. 332-333.

[A12] Investigation of thin films of yttria-stabilized zirconia with gold nanocrystals, prepared by annealing of island metal films / I.N. Antonov, O.N. Gorshkov,

D.A. Pavlov, M.E. Shenina, A.I. Bobrov, A.P. Kasatkin, M.N. Koryazhkina // Proceedings of “Forum of young scientists of Lobachevsky State University of Nizhny Novgorod” (Nizhny Novgorod). 2013. V. 1. Pp. 91-93. [In Russian]

[A13] Ion polarization processes in yttria-stabilized zirconia in MIM- and MIS-nanocapacitors / S.V. Tikhov, M.N. Koryazhkina, O.N. Gorshkov, A.P. Kasatkin, I.N. Antonov, A.I. Morozov // Proceedings of XXI International Symposium «Nanophysics and nanoelectronics» (Nizhny Novgorod). 2017. V. 2. Pp. 738-739. [In Russian]

[A14] Study of local charge accumulation in ZrO_2(Y), HfO_2(Y), SiO_2 films with Au nanoparticles by Kelvin Probe Force Microscopy / D.O. Filatov, I.N. Antonov, M.N. Koryazhkina, M.A. Ryabova, M.S. Dunaevskii // Proceedings of XXII International Symposium «Nanophysics and nanoelectronics» (Nizhny Novgorod). 2018. V. 1. Pp. 373-374. [In Russian]

[A15] Investigation of local charge accumulation in yttria stabilized zirconia films with Au nanoparticles by Scanning Kelvin Probe Microscopy / D.O. Filatov, O.N. Gorshkov, A.N. Mikhaylov, D.S. Korolev, M.N. Koryazhkina, M.A. Ryabova, I.N. Antonov, M.E. Shenina, D.A. Pavlov, M.S. Dunaevskii // Proceedings of 5th International School and Conference «Saint Petersburg OPEN 2018» (Saint Petersburg). 2018. Pp. 573-574.

[A16] Resistive switching of a memristor based on a thin-film structure ZrO_2(Y)/Ta_2O_5 by a noise signal / O. Tabakov, D. Filatov, D. Vrzheshch, A. Novikov, A. Belov, I. Antonov, A. Zdoroveishchev, M. Koriazhkina, A. Mikhaylov, O. Gorshkov, A. Dubkov, B. Spagnolo // Proceedings of the 23rd Scientific Conference on Radiophysics (Nizhny Novgorod). 2019. Pp. 508-511. [In Russian]

[A17] Statistical analysis of ZrO_2(Y)/Ta_2O_5-based memristor response to white Gaussian noise / M. Koriazhkina, D. Filatov, D. Vrzheshch, O. Tabakov, A. Novikov, A. Kharcheva, A. Belov, I. Antonov, V. Sharkov, A. Mikhaylov, O. Gorshkov, A. Dubkov, D. Valenti, B. Spagnolo // Proceedings of the International conference

“New Trends in Nonequilibrium Stochastic Multistable Systems and Memristors” (Erice). 2019. P. 25.

[A18] $ZrO_2(Y)/Ta_2O_5$-based memristor response to white Gaussian noise / M. Koriazhkina, D. Filatov, D. Vrzheshch, O. Tabakov, A. Novikov, A. Belov, I. Antonov, A. Zdoroveishchev, A. Mikhaylov, O. Gorshkov, A. Dubkov, B. Spagnolo // Proceedings of the 23rd Scientific Conference on Radiophysics (Nizhny Novgorod). 2019. Pp. 497-500.

[A19] Noise-induced resistive switching on the contact of the AFM-probe to the yttria stabilized zirconia film on a conductive substrate / D. Filatov, A. Novikov, V. Baranova, D. Antonov, A. Kruglov, I. Antonov, A. Zdoroveishchev, M. Koriazhkina, O. Gorshkov, A. Dubkov, B. Spagnolo // Proceedings of the 23rd Scientific Conference on Radiophysics (Nizhny Novgorod). 2019. Pp. 501-504. [In Russian]

List of references

1. Emerging non-volatile memories / S. Hong, O. Auciello, D. Wouters (Eds.). – Berlin-Heidelberg: Springer, 2014. 273 p.
2. Emerging Resistive Switching Memories / J. Ouyang. – Berlin-Heidelberg: Springer, 2016. 93 p.
3. Resistive Switching: From Fundamentals of Nanoionic Redox Processes to Memristive Device Applications / D. Ielmini, R. Waser (Eds.). – Weinheim: Wiley-VCH, 2016. 784 p.
4. The missing memristor found / D.B. Strukov, G.S. Snider, D.R. Stewart et al. // Nature. 2008. V. 453. Pp. 80-83.
5. Resistive switching random access memory - Materials, device, interconnects, and scaling considerations / Y. Wu, J. Liang, S. Yu et al. // Proc. 2012 IEEE International Integrated Reliability Workshop (South Lake Tahoe, CA, United States, October 14-18, 2012). Pp. 16-21.
6. Memristor-Based Nanoelectronic Computing Circuits and Architectures / I. Vourkas, G.Ch. Sirakoulis. – Berlin-Heidelberg: Springer, 2015. 241 p.
7. Memristor and Memristive Neural Networks / A. James (Ed.). – Rijeka: IntechOpen, 2018. 162 p.
8. An overview of materials issues in resistive random access memory / L. Zhu, J. Zhou, Z. Guo et al. // J. Materiomics. 2015. V. 1 (4). Pp. 285-295.
9. Review of mechanisms proposed for redox based resistive switching structures / I. Riess // J. Electroceramics. 2017. V. 39 (1-4). Pp. 61-72.
10. Resistive Switching in Oxides / A. Mehonic, A.J. Kenyon // Defects at Oxide Surfaces. – J. Jupille, G. Thornton (Eds.). – Cham: Springer, 2015. Pp. 401-428.
11. Nanoscale cation motion in TaO_x, HfO_x and TiO_x memristive systems / A. Wedig, M. Luebben, D.Y. Cho et al. // Nat. Nanotechnol. 2016. V. 11. Pp. 67-74.

12. Interfacial versus filamentary resistive switching in TiO_2 and HfO_2 devices / G. Sassine, S. La Barbera, N. Najjari et al. // J. Vac. Sci. Technol. B. 2016. V. 34. P. 012202.
13. In situ transmission electron microscopy observation of nanostructural changes in phase-change memory / S. Meister, S. Kim, J.J. Cha et al. // ACS Nano. 2011. V. 5. Pp. 2742-2748.
14. Review of Nanostructured Resistive Switching Memristor and its Applications / S.G. Hu, S.Y. Wu, W.W. Jia et al. // Nanosci. Nanotechnol. Lett. 2014. V. 6 (4). Pp. 729-757.
15. Nonvolatile resistive switching memory utilizing gold nanocrystals embedded in zirconium oxide / W. Guan, S. Long, R. Jia et al. // Appl. Phys. Lett. 2007. V. 91 (6). P. 062111.
16. Emission and conductivity of a capacitor type cathode / G.S. Kreinina, L.N. Selivanov, T.I. Shumskaya // Radiotehnika i electronika. 1960. V. 5 (8). Pp. 1338-1341. [In Russian]
17. Low-Frequency Negative Resistance in Thin Anodic Oxide Films // T.W. Hickmott // J. Appl. Phys. 1962. V. 33 (9). Pp. 2669-2682.
18. Electrical Phenomena in Amorphous Oxide Films / G. Dearnaley, A.M. Stoneham, D.V. Morgan // Rep. Prog. Phys. 1970. V. 33. Pp. 1129-1191.
19. Memristor – The missing circuit element / L. Chua // IEEE Transactions on Circuit Theory. 1971. V. 18 (5). Pp. 507-519.
20. Switching dynamics in titanium dioxide memristive devices / M.D. Pickett, D.B. Strukov, J.L. Borghetti et al. // J. Appl. Phys. 2009. V. 106. P. 074508.
21. Parallel memristive filaments model applicable to bipolar and filamentary resistive switching / X. Liu, K.P. Biju, J. Lee et al. // Appl. Phys. Lett. 2011. V. 99. P. 113518.
22. Forming-free colossal resistive switching effect in rare-earth-oxide Gd_2O_3 films for memristor applications / X. Cao, X. Li, X. Gao et al. // J. Appl. Phys. 2009. V. 106. P. 073723.

23. Resistive switching transition induced by a voltage pulse in a Pt/NiO/Pt structure / I. Hwang, M.-J. Lee, G.-H. Buh et al. // Appl. Phys. Lett. 2010. V. 97. P. 052106.
24. Atomic structure of conducting nanofilaments in TiO_2 resistive switching memory / D.-H. Kwon, K.M. Kim, J.H. Jang et al. // Nat. Nanotechnol. 2010. V. 5. Pp. 148-153.
25. Resistive Switching Characteristics of Solution-Processed Transparent TiO_x for Nonvolatile Memory Application / S. Jung, J. Kong, S. Song et al. // J. Electrochem. Soc. 2010. V. 157. Pp. H1042-H1045.
26. Nanofilamentary resistive switching in binary oxide system; a review on the present status and outlook / K.M. Kim, D.S. Jeong, C.S. Hwang // Nanotechnology. 2011. V. 22. P. 254002.
27. Forming and switching mechanisms of a cation-migration-based oxide resistive memory / T. Tsuruoka, K. Terabe, T. Hasegawa et al. // Nanotechnology. 2010. V. 21. P. 425205.
28. Bipolar resistive switching in Cu/AlN/Pt nonvolatile memory device / C. Chen, Y.C. Yang, F. Zeng et al. // Appl. Phys. Lett. 2010. V. 97. P. 083502.
29. Direct observation of microscopic change induced by oxygen vacancy drift in amorphous TiO_2 thin films / H.Y. Jeong, J.Y. Lee, S.-Y. Choi // Appl. Phys. Lett. 2010. V. 97. P. 042109.
30. Comprehensive modeling of resistive switching in the $Al/TiO_x/TiO_2/Al$ heterostructure based on space-charge-limited conduction / S. Kim, H.Y. Jeong, S.-Y. Choi et al. // Appl. Phys. Lett. 2010. V. 97. P. 033508.
31. Resistive switching memory: observations with scanning probe microscopy / M.H. Lee, C.S. Hwang // Nanoscale. 2011. V. 3. Pp. 490-502.
32. Stacked $GeO/SrTiO_x$ Resistive Memory with Ultralow Resistance Currents / C.H. Cheng, A. Chin, F.S. Yeh // Appl. Phys. Lett. 2011. V. 98. P. 052905.

33. Evolution of RESET current and filament morphology in low-power HfO_2 unipolar resistive switching memory / T.-H. Hou, K.-L. Lin, J. Shieh et al. // Appl. Phys. Lett. 2011. V. 98. P. 103511.
34. Mechanism for resistive switching in an oxide-based electrochemical metallization memory / S. Peng, F. Zhuge, X. Chen et al. // Appl. Phys. Lett. 2012. V. 100. P. 072101.
35. Improved switching uniformity in resistive random access memory containing metal-doped electrolyte due to thermally agglomerated metallic filaments / W. Lee, J. Park, S. Kim et al. // Appl. Phys. Lett. 2012. V. 100. P. 142106.
36. Nonlinear *I–V* relations and hysteresis in solid state devices based on oxide mixed-ionic-electronic conductors / A. Leshem, E. Gonen, I. Riess // Nanotechnology. 2011. V. 22. P. 254024.
37. Scaling limits of resistive memories / V.V. Zhirnov, R. Meade, R.K. Cavin et al. // Nanotechnology. 2011. V. 22. P. 254027.
38. Scaling analysis of submicrometer nickel-oxide-based resistive switching memory devices / D. Ielmini, S. Spiga, F. Nardi et al. // J. Appl. Phys. 2011. V. 109. P. 034506.
39. First-principles simulation of oxygen diffusion in HfO_x: Role in the resistive switching mechanism / S. Clima, Y.Y. Chen, R. Degraeve et al. // Appl. Phys. Lett. 2012. V. 100. P. 133102.
40. Nanoionics-based resistive switching memories / R. Waser, M. Aono // Nat. Mater. 2007. V. 6. Pp. 833-840.
41. Resistance switching of the nonstoichiometric zirconium oxide for nonvolatile memory applications / D.S. Lee, H. Choi, H. Sim et al. // IEEE Electron Device Lett. 2005. V. 26. Pp. 719-721.
42. Reproducible unipolar resistance switching in stoichiometric ZrO_2 films / X. Wu, P. Zhou, J. Li et al. // Appl. Phys. Lett. 2007. V. 90. P. 183507.
43. Modified resistive switching behavior of ZrO_2 memory films based on the interface layer formed by using Ti top electrode / Ch.-Y. Lin, C.-Y. Wu, C.-

Y. Wu et al. // J. Appl. Phys. 2007. V. 102. P. 094101.

44. Ti-Induced Recovery Phenomenon of Resistive Switching in ZrO_2 Thin Films / D.-Y. Lee, S.-Y. Wang, T.-Y. Tseng // J. Electrochem. Soc. 2010. V. 157. Pp. G166-G169.
45. Improvement of Resistive Switching Properties in ZrO_2-Based ReRAM With Implanted Ti Ions / Q. Liu, S. Long, W. Wang et al. // IEEE Electron Device Lett. 2009. V. 30. Pp. 1335-1337.
46. Unipolar resistive switching of Au^+-implanted ZrO_2 films / Q. Liu, L. Shibing, G. Weihua et al. // J. Semicond. 2009. V. 30. P. 042001.
47. Controllable oxygen vacancies to enhance resistive switching performance in a ZrO_2-based RRAM with embedded Mo layer / S. Wang, D.-Y. Lee, T.-Y. Huang et al. // Nanotechnology. 2010. V. 21. P. 495201.
48. Robust unipolar resistive switching of Co nano-dots embedded ZrO_2 thin film memories and their switching mechanism / M.-C. Wu, T.-H. Wu, T.-Y. Tseng // J. Appl. Phys. 2012. V. 111. P. 014505.
49. Resistive switching phenomena: A review of statistical physics approaches / J.S. Lee, S. Lee, T.W. Noh // Appl. Phys. Rev. 2015. V. 2. P. 031303.
50. Performance comparison of O-based and Cu-based ReRAM for high-density applications/ A. Calderoni, S. Sills, N. Ramaswamy // 2014 IEEE 6th International Memory Workshop. 2014. P. 14431683.
51. On the Switching Parameter Variation of Metal-Oxide RRAM – Part I: Physical Modeling and Simulation Methodology / X. Guan, S. Yu, H.-S. Philip Wong // IEEE Trans. Electron Devices. 2012. V. 59. Pp. 1172-1182.
52. Electrical Manipulation of Nanofilaments in Transition-Metal Oxides for Resistance-Based Memory / M.-J. Lee, S. Han, S.H. Jeon et al. // Nano Lett. 2009. V. 9. Pp. 1476-1481.
53. Self-Accelerated Thermal Dissolution Model for Reset Programming in Unipolar Resistive-Switching Memory (RRAM) Devices / U. Russo, D. Ielmini, C. Cagli et al. // IEEE Trans. Electron Devices. 2009. V. 56. Pp.

193-200.

54. A phenomenological model for the reset mechanism of metal oxide RRAM / S. Yu, H.-S. Philip Wong // IEEE Electron Device Lett. 2010. V. 31. Pp. 1455-1457.
55. Resistance-dependent amplitude of random telegraph-signal noise in resistive switching memories / D. Ielmini, F. Nardi, C. Cagli // Appl. Phys. Lett. 2010. V. 96. P. 053503.
56. Cycling-induced degradation of metal-oxide resistive switching memory (RRAM) / Z.-Q. Wang, S. Ambrogio, S. Balatti et al. // 2015 IEEE International Electron Devices Meeting. 2015. P. 15800854.
57. New conduction and reversible memory phenomena in thin insulating films / J.G. Simmons, R.R. Verderber // Proc. Math. Phys. Eng. Sci. 1967. V. 301. Pp. 77-102.
58. The mechanism of ionic conductivity in stabilized cubic zirconia / V.G. Zavodinsky // Phys. Solid State. 2004. V. 46. Pp. 453-457.
59. Ionic conductivity of ZrO_2–12 mol % Y_2O_3 single crystals / J.D. Solier, I. Cachadiña, A. Dominguez-Rodriguez // Phys. Rev. B. 1993. V. 48. Pp. 3704-3712.
60. Activation entropy and Gibbs free energy for conduction in yttria–stabilized-zirconia single crystals / I. Cachadiña, J. D. Solier, A. Domínguez-Rodríguez // Phys. Rev. B. 1995. V. 52. Pp. 10872-10876.
61. Atomic-level quantized reaction of HfO_x memristor / Y.-E. Syu, T.-C. Chang, J.-H. Lou et al. // Appl. Phys. Lett. 2013. V. 102. P. 172903.
62. Quantum conductance and switching kinetics of AgI based microcrossbar cells / S. Tappertzhofen, I. Valov, R. Waser // Nanotechnology. 2012. V. 23. P. 145703.
63. Quantum Conductance in Silicon Oxide Resistive Memory Devices / A. Mehonic, A. Vrajitoarea, S. Cueff et al. // Sci. Rep. 2013. V. 3. P. 2708.
64. A study on low-power, nanosecond operation and multilevel bipolar resistance

switching in Ti/ZrO_2/Pt nonvolatile memory with 1T1R architecture / M.-C. Wu, W.-Y. Jang, C.-H. Lin et al. // Semicond. Sci. Technol. 2012. V. 27 (6). P. 065010.

65. N.V. Malekhonova, Profiling of the composition of heteronanostructures by Z-contrast and X-ray energy dispersive spectroscopy: dis. PhD thesis / Natalya Viktorovna Malekhonova. UNN (Nizhny Novgorod, Russia), 2016. 118 p.
66. Investigation of resistive switching in the nanocomposite zirconia films by tunneling atomic force microscopy / D.O. Filatov, D.A. Antonov, O.N. Gorshkov et al. // Atomic Force Microscopy (AFM): Principles, Modes of Operation and Limitations. – H. Yang (Eds.) – New York: Nova Science Publishers, Inc., 2014. Pp.335-357.
67. Direct observation of conducting filaments on resistive switching of NiO thin films / J.Y. Son, Y.H. Shin // Appl. Phys. Lett. 2008. V. 92. P. 222106.
68. Handbook of Physical Vapor Deposition (PVD) Processing: Film Formation, Adhesion, Surface Preparation and Contamination Control / D.M. Mattox. – Westwood, New Jersey, USA: Noyes Publications, 1998. 945 p.
69. Thermal activation current spectroscopy of high-resistance semiconductors and dielectrics / Yu.A. Gorokhovatsky, G.A. Bordovsky. – Moscow: Nauka, 1991. 244p. [In Russian]
70. Kelvin probe force microscopy / M. Nonnenmacher, M.P. O'Boyle, H.K. Wickramasinghe // Appl. Phys. Lett. 1991. V. 58. Pp. 2921-2923.
71. The interactive visual development of applications of automation scientific and industrial measuring and control systems by means of LabVIEW 6i National Instruments / A.A. Andronov, A.V. Belyakov, V.A. Guryev et al. // Proceedings of "NATO Project SfP–973799 Semiconductors 2nd Workshop" (Nizhny Novgorod). 2002. P. 38.
72. Intrinsic electron and hole defects in stabilized zirconia single crystals / V.M. Orera, R. I. Merino, Y. Chen et al. // Phys. Rev. B. 1990. V. 42. Pp. 9782-9789.

73. Grain Boundary Engineering to Improve Ionic Conduction in Thin Films for Micro-SOFCs / A. Tarancón, A. Morata, D. Pla et al. // ECS Trans. 2015. V. 69. Pp. 11-16.
74. Measuring capacitor characteristics / S.L. Epstein. – Moscow: Energiya, 1965. 235 p. [In Russian]
75. Physics of semiconductors and dielectrics / P.T. Oreshkin. – Moscow: Visshaya shkola, 1977. 448 p. [In Russian]
76. High-κ gate dielectrics: Current status and materials properties considerations / D. Wilk, R.M. Wallace, J.M. Anthony // J. Appl. Phys. 2001. V. 89. Pp. 5243-5275.
77. Physics of semiconductor devices / S.M. Sze. – New York: Wiley, 1969. 812 p.
78. Electron conduction mechanism and band diagram of sputter-deposited Al/ZrO_2/Si structure / F.-C. Chiu, Z.-H. Lin, C.-W. Chang et al. // J. Appl. Phys. 2005. V. 97. P. 034506.
79. CRC Handbook of Chemistry and Physics 97th Edition / W.M. Haynes (Ed.). – UK: Taylor & Francis Group, 2017. 2643 p.
80. Physical and chemical properties of oxides: a handbook / G.V. Samsonov et al. (Eds.). – Moscow: Metallurgia, 1978. 472 p. [In Russian]
81. Titanium chemistry / G.P. Lucinschi – Moscow: Himiya, 1971. 471 p. [In Russian]
82. Nanobatteries in redox-based resistive switches require extension of memristor theory / I. Valov, E. Linn, S. Tappertzhofen et al. // Nat. Commun. 2013. V. 4. P. 1771.
83. Relation between currents and charges measured in samples during diagnostics of inhomogeneous insulating films / S. G. Dmitriev // Semiconductors. 2009. V. 43. Pp. 823-827.
84. Correlation between intrinsic electron traps and electrical conductivity in stabilised zirconia / R.I. Merino, V.M. Orera // Solid-State Ion. 1995. V. 76. Pp. 97-102.

85. Dynamics of interacting oxygen ions in yttria stabilized zirconia: bulk material and nanometer thin films / K.L. Ngai, J. Santamaria, C. Leon // Eur. Phys. J. B. 2013. V. 8687. Pp. 1-10.
86. Electronic processes in semiconductors with space charge regions / V.N. Ovsyuk. – Novosibirsk: Nauka, 1984. 252 p. [In Russian]
87. Ion Transport Phenomena in Insulating Films / E.H. Snow, A.S. Grove, B.E. Deal et al. // J. Appl. Phys. 2004. V. 36. Pp. 1664-1673.
88. Modeling the Universal Set/Reset Characteristics of Bipolar RRAM by Field- and Temperature-Driven Filament Growth / D. Ielmini // IEEE Trans. Electron Devices. 2011. V. 58. Pp. 4309-4317.
89. Resistive switching memories based on metal oxides: mechanisms, reliability and scaling / D. Ielmini // Semicond. Sci. Technol. 2016. V. 31. P. 063002.
90. Role of metal-oxide interfaces in the multiple resistance switching regimes of Pt/HfO_2/TiN devices / S. Brivio, J. Frascaroli, S. Spiga // Appl. Phys. Lett. 2015. V. 107. P. 023504.
91. Multi-scale quantum point contact model for filamentary conduction in resistive random access memories devices / X. Lian, X. Cartoixà, E. Miranda et al. // J. Appl. Phys. 2014. V. 115. P. 244507.
92. Current overshoot during set and reset operations of resistive switching memories / A. Chen // Proceedings of “IEEE International Reliability Physics Symposium” (Anaheim). 2012. Pp. MY.2.1-MY.2.4.
93. Oxygen migration during resistance switching and failure of hafnium oxide memristors / S. Kumar, Z. Wang, X. Huang et al. // Appl. Phys. Lett. 2017. V. 110. P. 103503.
94. Defect-engineered electroforming-free analog HfO_x memristor and its application to the neural network / G.S. Kim, H. Song, Y.K Lee et al. // ACS Appl. Mater. Interfaces. 2019. V. 11. Pp. 47063-47072.
95. Current injection in solids / M.A. Lampert, P. Mark. – New York and London: Academic Press, 1970. 351 p.

96. A detailed understanding of the electronic bipolar resistance switching behavior in Pt/TiO_2/Pt structure / K.M. Kim, B.J. Choi, M.H. Lee et al. // Nanotechnology. 2011. V. 22. P. 254010.
97. Chemist's Handbook / B.P. Nikolsky (Ed.). – Moscow: Himiya, 1966. 1072 p. [In Russian]
98. A fast, high-endurance and scalable non-volatile memory device made from asymmetric Ta_2O_{5-x}/TaO_{2-x} bilayer structures / M.J. Lee, C.B Lee, D. Lee et al. // Nat. Mater. 2011. V. 10. Pp. 625-630.
99. Sub-10 nm Ta channel responsible for superior performance of a HfO_2 memristor / H. Jiang, L. Han, P. Lin et al. // Sci. Rep. 2016. V. 6. P. 28525.
100. Multilayer metal-oxide memristive device with stabilized resistive switching / A. Mikhaylov, A. Belov, D. Korolev et al. // Adv. Mater. Technol. 2020. V.5. P. 1900607.
101. A light-controlled resistive switching memory / M. Ungureanu, R. Zazpe, F. Golmar et al. // Adv. Mater. 2012. V. 24. Pp. 2496-2500.
102. Light-activated resistance switching in SiO_x RRAM devices / A. Mehonic, T. Gerard, A.J. Kenyon // Appl. Phys. Lett. 2017. V. 111. P. 233502.
103. Wavelength dependent light tunable resistive switching graphene oxide nonvolatile memory devices / A.H. Jaafar, N.T. Kemp // Carbon. 2019. V. 153. Pp. 81-88.
104. Atomic scale plasmonic switch / A. Emboras, J. Niegemann, P. Ma et al. // Nano Lett. 2016. V. 16. Pp. 709-714.
105. Atomic scale photodetection enabled by a memristive junction / A. Emboras, A. Alabastri, F. Ducry et al. // ACS Nano. 2018. V. 12. Pp. 6706-6713.
106. Reversible optical switching memristors with tunable STDP synaptic plasticity: A route to hierarchical control in artificial intelligent systems / A.H. Jaafar, R.J. Gray, E. Verrelli et al. // Nanoscale. 2017. V. 9. Pp. 17091-17098.
107. Optoelectronic synapses based on hot-electron-induced chemical processes / P. Wang, M.E. Nasir, A.V. Krasavin et al. // Nano Lett. 2020. V. 20. Pp. 1536-

1541.

108. Photovoltaic and photoconductive theory applied to InSb / T.S. Moss // J. Electron. Control. 1955. V. 1 (2). Pp. 126-133.
109. Surface photovoltage phenomena: theory, experiment, and applications / L. Kronik, Y. Shapira // Surf. Sci. Rep. 1999. V. 37 (1). Pp. 1-206.
110. Electrical and photoelectric properties of Si-based metal-insulator-semiconductor structures with Au nanoparticles at the insulator-semiconductor interface / M. N. Koryazhkina, S. V. Tikhov, O. N. Gorshkov et al. // Semiconductors. 2016. V. 50. Pp. 1614-1618.
111. On the stochastic nature of resistive switching in metal oxide RRAM: Physical modeling, Monte Carlo simulation, and experimental characterization / S. Yu, X. Guan and H.-S.P. Wong // Proc. IEEE Int. Electr. Dev. Meet. 2011. Pp. 17.3.1-17.3.4.
112. Stochastic electronics: a neuro-inspired design paradigm for integrated circuits / T.J. Hamilton, S. Afshar, A. van Schaik et al. // Proc. IEEE. 2014. V. 102. Pp. 843-859.
113. Stochastic switching of TiO_2-based memristive devices with identical initial memory states / Q. Li, A. Khiat, I. Salaoru et al. // Nanoscale Res. Lett. 2014. V. 9. P. 293.
114. Stochasticity Modeling in Memristors / R. Naous, M. Al-Shedivat and K.N. Salama // IEEE Trans. Nanotechnol. 2016. V. 15. P. 15.
115. Stochasticity in materials structure, properties and processing - A review / R. Hull, P. Keblinski, D. Lewis et al. // Appl.Phys.Rev. 2018. V. 5. P. 011302.
116. In situ observation of filamentary conducting channels in an asymmetric Ta_2O_{5-x}/TaO_{2-x} bilayer structure / G.-S. Park, Y.B. Kim, S.Y. Park et al. // Nat. Commun. 2013. V. 4. P. 2382.
117. Stability, bistability and instability of amorphous ZrO_2 resistive memory devices / P. Parreira, G.W. Paterson, S. McVitie et al. // J. Phys. D. 2016. V. 49. P. 095111.

118. Impact of oxygen exchange reaction at the ohmic interface in Ta_2O_5-based ReRAM devices / W. Kim, S. Menzel, D.J. Wouters et al. // Nanoscale. 2016. V. 8. P. 17774.
119. Quantized conductance coincides with state instability and excess noise in tantalum oxide memristors / W. Yi, S.E. Savel'ev, G. Medeiros-Ribeiro et al. // Nat. Commun. 2016. V. 7. P. 11142.
120. Complex dynamics in multistable systems / U. Feudel // Int. J. Bifurcat. Chaos. 2008. V. 18. P. 1607.
121. Stochastic resonance in a tunnel diode in the presence of white or coloured noise / R.N. Mantegna and B. Spagnolo // Il Nuovo Cimento D. 1995. V. 17. P. 873.
122. Experimental study of a nonlinear system in the presence of noise: The stochastic resonance / E. Lanzara, R.N. Mantegna, B. Spagnolo et al. // Am. J. Phys. 1997. V. 65. P. 341.
123. Linear and nonlinear experimental regimes of stochastic resonance / R.N. Mantegna, B. Spagnolo and M. Trapanese // Phys. Rev. E. 2001. V. 63. P. 011101.
124. Moment equations for a spatially extended system of two competing species / D. Valenti, L. Schimansky-Geier, X. Sailer et al. // Eur. Phys. J. B. 2006. V. 50. P. 199.
125. Spatio-temporal patterns in population dynamics / A. La Barbera and B. Spagnolo // Physica A. 2002. V. 314. P. 120.
126. Pattern formation and spatial correlation induced by the noise in two competing species / D. Valenti, A. Fiasconaro and B. Spagnolo // Acta Phys. Pol. B. 2004. V. 35. P. 1481.
127. Stochastic resonance in a trapping overdamped monostable system / N.V. Agudov, A.V. Krichigin, D. Valenti et al. // Phys. Rev. E. 2010. V. 81. P. 051123.
128. Stochastic resonance in multistable systems: The role of intermediate states /

C. Nicolis // Phys. Rev. E. 2010. V. 82. P. 011139.

129. Stochastic resonance in multistable systems: The role of dimensionality / C. Nicolis // Phys. Rev. E. 2012. V. 86. P. 011133.
130. Stochastic resonance in multi-stable system driven by Lévy noise / D. Han, X. Su and P. Shi // Chin. J. Phys. 2018. V. 56. P. 1559.
131. Experimental investigation of resonant activation / R.N. Mantegna and B. Spagnolo // Phys. Rev. Lett. 2000. V. 84. Pp. 3025-3028.
132. Nonmonotonic behavior of spatiotemporal pattern formation in a noisy Lotka-Volterra system / A. Fiasconaro, D. Valenti and B. Spagnolo // Acta Phys. Pol. B. 2004. V. 35. P. 1491.
133. A simple noise model with memory for biological systems / O. Chichigina, D. Valenti and B. Spagnolo // Fluc. Noise Lett. 2005. V. 5. P. L243.
134. Environmental metal pollution considered as noise: effects on the spatial distribution of benthic foraminifera in two coastal marine areas of Sicily (Southern Italy) / D. Valenti, L. Tranchina, M. Brai et al. // Ecol. Mod. 2008. V. 213. P. 449.
135. Verhulst model with Lévy white noise excitation / A.A. Dubkov and B. Spagnolo // Eur. Phys. J. B. 2008. V. 65. P. 361.
136. Volatility effects on the escape time in financial market models / B. Spagnolo and D. Valenti // Int. J. Bifurcat. Chaos. 2008. V. 18. P. 2775.
137. Resonant activation in piece-wise linear asymmetric potentials / A. Fiasconaro and B. Spagnolo // Phys. Rev. E. 2011. V. 83. P. 041122.
138. Stability in a system subject to noise with regulated periodicity / O.A. Chichigina, A.A. Dubkov, D. Valenti et al. // Phys. Rev. E. 2011. V. 84. P. 021134.
139. Stochastic memory: memory enhancement due to noise / A. Stotland and M. Di Ventra // Phys. Rev. E. 2012. V. 85. P. 011116.
140. Design of a Lambda system for population transfer in superconducting nanocircuits / G. Falci, A. La Cognata, M. Berritta et al. // Phys. Rev. B. 2013.

V. 87. P. 214515.

141. On the beneficial role of noise in resistive switching / G.A. Patterson, P.I. Fierens and D.F. Grosz // Appl. Phys. Lett. 2013. V. 103. P. 074102.
142. Stabilization of quantum metastable states by dissipation / D. Valenti, L. Magazzù, P. Caldara et al. // Phys. Rev. B. 2015. V. 91. P. 235412.
143. Noise-induced effects in nonlinear relaxation of condensed matter systems / B. Spagnolo, D. Valenti, C. Guarcello et al. // Chaos Solitons Fractals. 2015. V. 81. P. 412.
144. A parsimonious model for generating arbitrage-free scenario trees / A. Consiglio, A. Carollo and S.A. Zenios // Quant. Financ. 2016. V. 16. P. 201.
145. Nonlinear relaxation phenomena in metastable condensed matter systems / B. Spagnolo, C. Guarcello, L. Magazzù et al. // Entropy. 2017. V. 19. P. 20.
146. Enhancing metastability by dissipation and driving in an asymmetric bistable quantum system / B. Spagnolo, A. Carollo and D. Valenti // Entropy. 2018. V. 20. P. 226.
147. Stabilization by dissipation and stochastic resonant activation in quantum metastable systems / B. Spagnolo, A. Carollo and D. Valenti // Eur. Phys. J-Spec. Top. 2018. V. 227. P. 379.
148. Stabilizing effect of driving and dissipation on quantum metastable states / D. Valenti, A. Carollo and B. Spagnolo // Phys. Rev. A. 2018. V. 97. P. 042109.
149. Uhlmann curvature in dissipative phase transitions / A. Carollo, B. Spagnolo and D. Valenti // Sci. Rep. 2018. V. 8. P. 9852.
150. Symmetric logarithmic derivative of fermionic gaussian states / A. Carollo, B. Spagnolo and D. Valenti // Entropy. 2018. V. 20. P. 485.
151. Conductive Atomic Force Microscopy: Applications in Nanomaterials / M. Lanza (Ed.). – Weinheim: Wiley-VCH, 2017. 384 p.
152. Recommended methods to study resistive switching devices / M. Lanza, H.-S.P. Wong, E. Pop et al. // Adv. Electron. Mater. 2018. V. 5. P. 1800143.

153. A review of three-dimensional resistive switching cross-bar array memories from the integration and materials property points of view // J.Y. Seok, S.J. Song, J.H. Yoon et al. // Adv. Funct. Mater. 2014. V. 24. P. 5316.
154. A review on resistive switching in high-κ dielectrics: a nanoscale point of view using Conductive Atomic Force Microscope / M. Lanza // Materials. 2014. V. 7. P. 2155.
155. Scaling effect on silicon nitride memristor with highly doped Si substrate / S. Kim, S. Jung, M.-H. Kim // Small. 2018. V. 14. P. 1704062.
156. A very reliable multilevel YSZ resistive switching memory / F. Pan, J. Jang, V. Subramanian // Proc. IEEE 70th Device Research Conference (University Park, PA, United States, June 18-20, 2012). Pp. 217-218.
157. Filament growth and resistive switching in hafnium oxide memristive devices / S. Dirkmann, J. Kaiser, C. Wenger et al. // ACS Appl. Mater. Interfaces. 2018. V. 10. P. 14857.
158. Five non-volatile memristor enigmas solved / L. Chua // Appl. Phys. A. 2018. V. 124. P. 563.
159. The bistable potential: an archetype for classical and quantum systems / B. Spagnolo, P. Caldara, A. La Cognata, et al. // Int. J. Mod. Phys. B. 2012. V. 26. P. 1241006.
160. Changes in the resistive state of Au/Zr/SiO_2/TiN/Ti memristive structures under the influence of alternating voltage with different amplitudes / M.N. Koryazhkina, A.S. Novikov, A.I. Belov et al. // Meeting of the section «Stochastic multistable systems» of the 24rd Scientific Conference on Radiophysics. 2020. Data available by link: http://www.stolab.unn.ru/index.php/news/87-news20200529. [In Russian]
161. Analysis of the statistics of device-to-device and cycle-to-cycle variability in TiN/Ti/Al:HfO_2/TiN RRAMs / E. Pérez, D. Maldonado, C. Acal et al. // Microelectron. Eng. 2019. V. 214. Pp.104-109.
162. Impact of ultra-thin Al_2O_{3-y} layers on TiO_{2-x} ReRAM switching characteristics /

M. Trapatseli, S. Cortese, A. Serb et al. // J. Appl. Phys. 2017. V. 121. P. 184505.

163. High precision tuning of state for memristive devices by adaptable variation-tolerant algorithm / F. Alibart, L. Gao, B.D. Hoskins et al. // Nanotechnology. 2012. V. 23. P. 075201.
164. High precision analogue memristor state tuning / R. Berdan, T. Prodromakis, C. Toumazou // Electron. Lett. 2012. V. 48. Pp. 1105-1107.
165. Nanoscale resistive switching devices for memory and computing applications / S.H. Lee, X. Zhu, W.D. Lu // Nano Res. 2020. V. 13. Pp. 1228-1243.
166. Dynamical attractors of memristors and their networks / Y.V. Pershin, V.A. Slipko // EPL. 2019. V. 125. P. 20002.
167. Bifurcation analysis of a TaO memristor model / Y.V. Pershin, V.A. Slipko // J. Phys. D. 2019. V. 52. P. 505304.
168. Compact model of nonlinear dynamics while the cycling of a memristor / R. Mikheev, G. Teplov, I. Matyushkin // 2019 IEEE Conf. Russ. Young Res. Electr. Electron. Eng. 2019. V. 2. Pp. 2057-2061.
169. Stochastic resonance in a tunnel diode / R.N. Mantegna and B. Spagnolo // Phys. Rev. Rap. Comm. E. 1994. V. 49. Pp. R1792-R1795.
170. Stochastic resonance and noise delayed extinction in a model of two competing species / D. Valenti, A. Fiasconaro and B. Spagnolo // Physica A. 2004. V. 331. Pp. 477-486.
171. Stochastic resonance / L. Gammaitoni, P. Hänggi, P. Jung et al. / Rev. Mod. Phys. 1998. V. 70. Pp. 223-287.
172. Noise enhanced stability in an unstable system / R.N. Mantegna and B. Spagnolo // Phys. Rev. Lett. 1996. V. 76. Pp. 563-566.
173. Noise-enhanced stability of periodically driven metastable states / N.V. Agudov and B. Spagnolo // Phys. Rev. E. 2001. V. 64. P. 035102(R).
174. Noise-enhanced stability in fluctuating metastable states / A.A. Dubkov, N.V. Agudov and B. Spagnolo // Phys. Rev. E. 2004. V. 69. P. 061103.

175. Signatures of noise-enhanced stability in metastable states / A. Fiasconaro, B. Spagnolo, and S. Boccaletti // Phys. Rev. E. 2005. V. 72. P. 061110.
176. Resonant activation over a fluctuating barrier / C.R. Doering, J.C. Gadoua // Phys. Rev. Lett. 1992. V. 69. Pp. 2318-2321.
177. Experimental investigation of memristance enhancement / V. Ntinas, A. Rubio, G.C. Sirakoulis et al. // 2019 IEEE/ACM Int. Symp. Nanoscale Archit. 2019. V. 1. P. 1.
178. Power-efficient noise-induced reduction of ReRAM cell's temporal variability effects / V. Ntinas, A. Rubio, G.C. Sirakoulis et al. // 2020 IEEE Trans. Circuits Syst. II: Express Briefs. 2020. P. 1-5.
179. Stochastic resonance subject to multiplicative and additive noise: the influence of potential asymmetries / Z. Qiao, Y. Lei, J. Lin et al. // Phys. Rev. E. 2016. V. 94. P. 052214.